UNIVERSITÀ DEGLI STUDI DI PADOVA

Sede Amministrativa: Università degli Studi di Padova

Sede Consorziata: Université de Grenoble

Dipartimento di Geoscienze

SCUOLA DI DOTTORATO DI RICERCA IN SCIENZE DELLA TERRA

CICLO XXIV

Physico-chemical processes in seismogenic faults: active and exhumed examples

Direttore della Scuola : Ch.mo Prof. Gilberto Artioli

Supervisore : Ch.mo Prof. Giulio Di Toro

Ch.mo Prof. Jean-Pierre Gratier

Dottorando : Silvia Mittempergher

Riassunto

I processi chimici e fisici attivi nel ciclo sismico controllano l'evoluzione delle proprietà meccaniche delle zone di faglia, sia nel breve (durante la propagazione di un terremoto) che nel lungo periodo (per esempio, il recupero delle proprietà elastiche delle rocce di faglia nel periodo intersismico). L'irregolare distribuzione dei terremoti nel tempo è infatti dovuta alla complessa interazione tra energia di deformazione elastica accumulata nell'incassante e l'evoluzione temporale delle proprietà meccaniche (coesione, attrito, ecc.) delle zone di faglia. Studiare le rocce di faglia naturali è un mezzo per riconoscere i processi attivi nelle varie fasi del ciclo sismico e per confrontarne le tessiture con rocce deformate in laboratorio in condizioni controllate. Il campionamento di rocce in faglie sismogenetiche può avvenire attraverso (i) perforazioni di faglie attive e (ii) faglie non più attive ed oggi esumate nelle catene montuose. La perforazione di faglie attive permette di correlare i processi fisici e chimici identificati nelle rocce di faglia con l'attività (sismicità o scivolamento asismico) registrata in tempo reale, ma è limitata ai primi chilometri di crosta. Le faglie esumate d'altro canto permettono di accedere a livelli crostali più profondi e compatibili con quelli di nucleazione di grandi terremoti, ma si hanno pochi vincoli sul loro stile deformativo.

In questa tesi, vengono studiati campioni da due faglie sismogenetiche: la Faglia di San Andreas (California, USA), faglia sismogenetica attiva, e la Faglia delle Gole Larghe (Alpi Meridionali, Italia), faglia sismogenetica esumata. Le faglie e le rocce di faglia sono state studiate integrando diversi metodi: geologia strutturale, deformazione sperimentale di rocce, analisi microstrutturale (microscopia ottica ed in catodoluminescenza, microscopio elettronico ad emissione di campo (FESEM), diffrazione da retrodiffusione elettronica (EBSD), analisi di immagine), mineralogia (diffrazione da raggi X (XRD)), geochimica (fluorescenza da raggi X (XRF), microanalisi da spettroscopia a dispersione di energia da raggi X (EDS), spettroscopia ad infrarosso (FTIR), microsonda elettronica (EPMA)), geochimica degli isotopi stabili.

La Faglia di San Andreas è stata perforata fino ad una profondità di 2.7 km presso Parkfield (California centrale) nell'ambito del progetto SAFOD (San Andreas Fault Observatory at Depth), con il recupero di tre carote da profondità prossime agli ipocentri di terremoti di bassa intensità (M<3) registrati in questo tratto della faglia. Nei campioni studiati, abbiamo identificato una sovrapposizione ciclica di strutture legate a presso-soluzione(*creep*), idrofratturazione e ancora presso-soluzione. Questo potrebbe confermare il modello secondo cui, in faglie mature e ricche in materiali argillosi come la Faglia di San Andreas, si possano formare delle sacche poco permeabili isolate in cui la pressione dei fluidi può aumentare a causa della continua compattazione del materiale di faglia, fino a superare la resistenza alla rottura della roccia.

La faglia delle Gole Larghe è una faglia esumata che era attiva 30 Ma fa a 9 -11 km di profondità. La presenza di pseudotachiliti, fusi di frizione prodotti durante lo scivolamento sismico, testimonia

l'attività sismica passata. La Faglia delle Gole Larghe permette quindi di avere un accesso diretto ai processi che avvengono alla profondità dei maggiori terremoti nella crosta continentale. Due argomenti sono stati affrontati: (i) l'evoluzione microstrutturale delle rocce cataclastiche associate alle pseudotachiliti all'aumentare della deformazione. Lo scopo dello studio è identificare i processi (intersismici) che possono portare alla nucleazione di instabilità frizionali nelle prime fasi di crescita di una faglia. Ai processi fragili come fratturazione e cataclasi si sovrappongono processi di pressо-soluzione e alterazione, favoriti dalla frammentazione della roccia e dall'ingresso di fluidi idrotermali. (ii) L'origine dei fluidi nelle faglie sismogenetiche e nel processo di fusione per attrito. Nel caso della Faglia delle Gole Larghe, la formazione di un sistema di faglie cataclastiche consente l'ingresso di un fluido acquoso, di probabile origine profonda, anche se non può essere esclusa una componente di fluidi meteorici o connati. La caratterizzazione della speciazione dell'acqua attraverso spettoscopia FTIR nelle pseudotachiliti ha permesso di identificare un'idratazione tardiva (post-deformativa) delle pseudotachiliti. La composizione isotopica delle psudotachiliti (ricalcolata escludendo l'effetto dell'idratazione) è simile a quello di pseudotachiliti artificiali prodotte in condizioni anidre. La principale fonte di fluidi nelle pseudotachiliti è quindi la deidratazione dei minerali idrati (biotite, clorite, epidoto) della roccia incassante indotta dal calore di frizione prodotto dallo scivolamento cosismico.

Abstract

The time recurrence of earthquakes is the result of the complex feedback between the tectonic loading on a fault and the time-dependent evolution of fault strength. The chemical and physical processes active during the seismic cycle, control the short term and long term mechanical properties of the fault zone. The study of natural fault rocks is a method for recognizing the processes occurring in the seismic cycle and for finding a correspondence with rocks experimentally deformed in controlled conditions. The study of seismic fault zone rocks are attained (i) by scientific drilling in active fault zones and (ii) by the study of ancient seismic faults now exhumed in mountain ranges. Drilling is limited to the first kilometers of crust, but the features found in fault rocks can be correlated with detailed in-situ measurements of the fault activity. Exhumed fault zones allow to the study of fault rocks from a large span of depth in the crust, but little can be inferred on their activity.

In this thesis, two case studies are examined: the modern seismogenic San Andreas Fault (California, USA) and the ancient seismogenic Gole Larghe Fault (Southern Alps, Italy). The fault rocks and fault zones are investigated by integrating methods from: structural geology, experimental rock deformation, microstructural analysis (optical microscopy, cathdolouminescence microscopy, field emission scanning electron microscopy (FE-SEM), electron back scatter diffraction (EBSD), image analysis), mineralogy (X-ray diffraction (XRD), geochemistry (X-ray fluorescence (XRF), energy dispersive spectrometry (EDS) X-ray microanalysis, Fourier transform infrared (FTIR) spectroscopy, electron probe micro-analysis (EPMA)) and stable isotope geochemistry.

The San Andreas Fault was drilled to 2.7 km depth at Parkfield (central California) within the SAFOD (San Andreas Fault Observatory at Depth) project, and samples were extracted from the depth of nucleation of repeating microearthquakes registered in that fault strand. The identification of a cyclic recurrence of pressure-solution creep, hydrofracture and pressure solution creep supports the idea that, in mature fault zones as the San Andreas Fault, isolated compartments of high fluid pressure might cause small to moderate in size earthquakes, associated to the dominant creep activity.

The Gole Larghe Fault Zone is an exhumed fault which was active 30 Ma ago at 9 – 11 km depth. The occurrence of pseudotachylytes, frictional melts produced during seismic slip, witnesses the seismic behavior of the fault, and allows to investigate the processes occurring at hypocentral depths of major intracrustal earthquakes. Two topics were investigated: (i) The fabric evolution of cataclastic rocks with increasing deformation. This microstructural study aims to identify the (interseismic?) processes potentially leading to the onset of unstable slip at the early stages of fault growth. Brittle processes as fracturing and cataclasis are overprinted by pressure solution processes and alteration enhanced by rock fragmentation and fluid ingression. (ii) The origin of fluids involved in seismic faulting and frictional melting. The formation of a cataclastic fault network might allow the ingression of external hydrous fluids, probable deep in origin, although mixing with meteoric or

connate fluids cannot be excluded. Isotope studies in natural pseudotachylytes were coupled with detailed mineralogical characterization, which allowed to identify a (post-deformation) late hydration of the pseudotachylytes. The similar isotopic composition of natural pseudotachylytes (re-calculated excluding the effects of late hydration) and dry experimentally-produced pseudotachylytes suggests that the main fluid source is the dehydration induced by coseismic frictional heating of OH-bearing minerals (biotite, chlorite, epidote) in the wall rocks.

Résumé

Les processus physiques et chimiques activés pendant le cycle sismique déterminent l'évolution des propriétés mécaniques des failles, à court terme (pendant la propagation de un séisme) comme à long terme (pour exemple, la récupération des propretés élastiques des roches de faille pendant le période interséismique). Les tremblements de terre se répètent à intervalles du temps irrégulier. Ca est une conséquence des complexes interactions entre l'énergie élastique accumulée dans le roches et l'évolution temporelle des propriétés mécaniques (cohésion, friction…) des zones de faille. L'étude des roches de faille naturelles est un moyen pour reconnaitre les processus actives pendant les diverses phases des cycle séismique et pour comparer les microstructures avec roches déformées en laboratoire en conditions connues . Il est possible accéder directement aux zones de nucléation des séismes au moyen (i) de forages à travers des failles actives, (ii) ou de l'étude de failles qui ne sont plus actives et qui ont été exhumées par des processus tectoniques. Le forage à travers des failles actives permit de corréler les processus physiques et chimiques identifiés dans les roches de faille avec l'activité (séismes ou frottement aséismique) sous monitorage continu, mais les forages sont limités à les premières kilomètres de croute. Les failles exhumées permettent de accéder à failles actives plus en profondeur dans la croûte, ou les sources des grandes tremblements de terre sont localisées, mais on a peu de contraintes sur les style de déformation.

En cette thèse, échantillons prévenants de deux failles séismiques sont étudiés: la Faille de San Andreas (California, USA), une faille séismique active, et la faille de Gole Larghe (Alpes Méridionales, Italie), une faille séismique exhumée. Les failles et roches de faille sont étudié par moyen de l'intégration de plusieurs techniques analytiques: géologie structurale, deformation expérimentale de roches, analyse microstructurale (microscope optique et en cathodoluminescence, microscope électronique à balayage à émission de champ (FESEM), imagerie en diffraction d'électrons rétrodiffusés (EBSD), analyse d'image), minéralogie (diffraction de rayons X) géochimie (spectrométrie de rayon X (EDS), spectrométrie à l'infrarouge (FTIR), microsonde électronique (EPMA)), géochimie des isotopes stables.

La Faille de San Andreas a été forée jusqu'à 3km de profondeur près de Parkfield dans le cadre du projet SAFOD (San Andreas Fault Observatory at Depth) et échantillonnée à profondeur des hypocentres des microséismes (M<3) enregistrés dans ce région. Les échantillons montrent une superposition de: pression-dissolution ,hydrofracturation et encore pression dissolution. La succession des évents est compatible avec la formation de sacs de fluides dans zones de basse perméabilité, ou la pression de fluides augmente à cause de le progressif compactage de le gouge de faille, jusqu'à la rupture.

La faille de Gole Larghe est une faille exhumée, qui a exceptionnellement préservé des structures de séismes qui ont eu lieu à 9 - 11 km de profondeur il y a 30 millions d'années. Les pseudotachylytes (roches fondues par le chaleur de friction pendant une frottement séismique) présentes le long la faille sont une évidence de ancienne activité séismique. Deux argumentes sont

traités: (i) l'évolution des microstructures des cataclasites associées à les pseudotachylytes. L'objectif est de identifier les processus (interséismiques) qui peuvent porter à la formation de instabilités frictionnelles pendant les premières phases de croissance de une faille. Les processus de pression – dissolution et altération sont superposé à les processus fragiles (fracturation et cataclasis), favorisant les interaction roche-fluides. (ii) L'origine des fluides dans les failles séismiques et dans la fusion pour friction. Dans la Faille de Gole Larghe, la formation de un système de failles à cataclasites permit la percolation de un fluide aqueux de profondeur (même si des components météoriques ou connates ne peuvent pas être exclues). Une hydratation tardive des pseudotachylytes est mesuré par spectroscopie infrarouge. La composition isotopique des pseudotachylytes (calculé sans la component de hydratation) est proche à celle des pseudotachylytes reproduites en expériences du laboratoire (sans fluides). La principale source de fluides dans le pseudotachylytes est donc la déshydratation des minéraux hydraté (biotit, clorit et epidote) des roches autour de la faille.

Table of contents

Chapter 1. Introduction

1.1 Fluid enhanced physico-chemical processes in the seismic cycle

Slip on seismogenic faults is attained by a repetition of earthquakes, which occur at not predictable intervals and locations (Gilbert, 1909), and interseismic creep (e.g. afterslip, Johanson eet al., 2006). The elastic rebound theory, formulated by Reid (1910) based on geodetic data from the San Francisco earthquake of 1906, formalizes the observations of Gilbert, by interpreting the earthquakes as the result of sudden relaxation of elastic strain, which was accumulated over a long period (centuries to millennia) by the steady motion of the regions on either side of the fault. If the cycle of loading - failure were regular, the time prediction of earthquakes would be possible, once the rate of tectonic loading and the fault strength were known (e.g., characteristic earthquakes: for a discussion about earthquake prediction and probabilistic forecastins, Jordan et al., 2011). Both stress loading of the fault and fault strength evolve in a complex way during time, and their interactions determines the complexity of the seismic cycle (Kanamori and Brodsky, 2004) (Figure 1). The complex behavior of faults depends on the interaction between:

(i) The rate of stress loading. Perturbations of the background tectonic loading might arise from static and dynamic stress changes due to slip on nearby faults (e.g., Stein, 1999; Gomberg et al., 2001; Johnson and Xiaoping, 2005), or by the mechanical effects of pore fluid migration (e.g. Miller et al., 2004).

(ii) The time dependent strength of the fault zones. Physical and chemical processes in the fault zone rocks control the short term (e.g., coseismic processes, velocity-dependent weakening and strengthening, Sone and Shimamoto, 2009; Di Toro et al., 2011) and long term fault strength (evolution of elastic properties of the fault zone with time, fault sealing, fault weakening processes: Blanpied et al., 1992a,b; Miller et al., 1996; Gratier et al., 2003; 2011; Jefferies et al., 2006; Smith et al., 2008; Collettini et al., 2009).

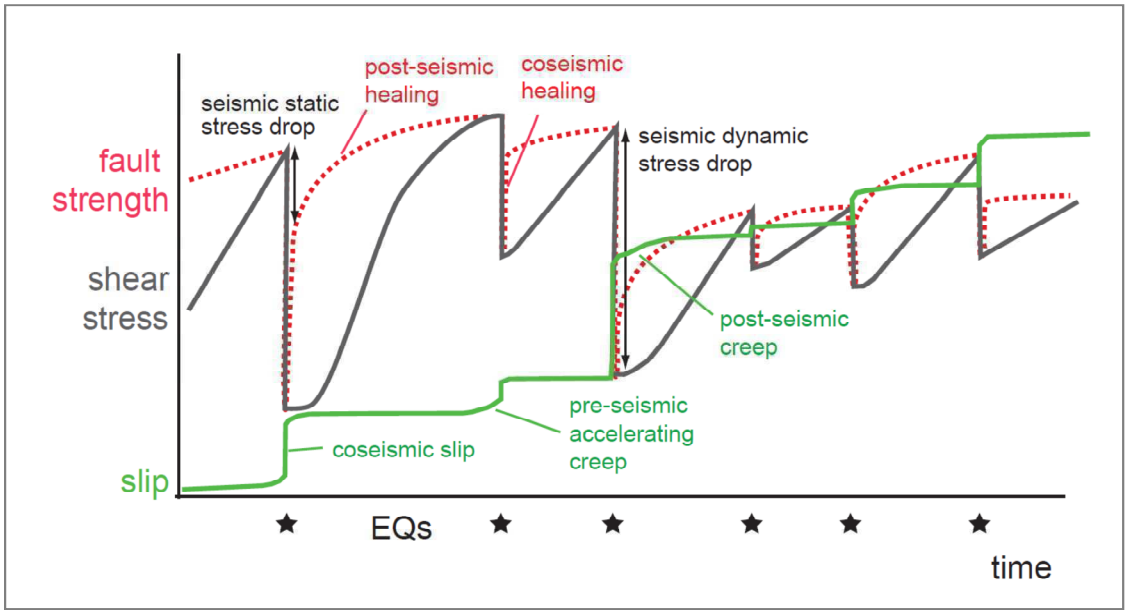

FIGURE 1.1. Fault failure occurs when the shear stress exceeds the fault strength. Both fault strength and loading stress evolve in time, and their feedback determines the irregular earthquake recurrence times. Pre-seismic accelerating creep might occur for some earthquakes. Post seismic creep might be as large as coseismic slip in some fault patches. This framework renders a physically-based earthquake forecasting model an extremely challenging task (from Di Toro et al., in press).

Understanding the processes controlling the evolution of the fault zone properties during the seismic cycle is a fundament for a physically-based probabilistic forecasting of earthquakes, and for determining the conditions which make a fault accommodate deformation by aseismic slip instead of seismically. Rocks which form in fault zones preserve the signatures of the processes affecting the fault rocks during the seismic cycle (e. g., Sibson, 1977; Smith et al., 2008). Earthquakes nucleate at depth in the crust: active earthquake sources can be accessed only by deep drilling of active fault zones and the depth of investigation is limited to the first 3km (e.g., Zoback et al., 2010; Boullier, 2011). The sources of the most intense earthquakes in the continental crust are located around 10 – 15 km depth (Scholz, 2002), and can be investigated only when faults are exhumed by tectonics (e.g. Sibson, 1977). In this thesis, physic-chemical processes occurring in natural fault zones have been investigated in two case studies: the active San Andreas Fault, in California, which was drilled to 3 km depth, and the exhumed Gole Larghe Fault zone, an exhumed seismogenic source exhumed from 10 km. Fluid-rock interactions have been found to be pervasive in both geological context. Fluids are crucial in controlling the physical properties of fault zones, as well as their mechanical behavior at the scale of the seismic cycle. The influx of fluids spans from mechanical effects on the nucleation,

propagation, arrest and recurrence of earthquakes, to the long term compositional and structural evolution of a fault zone.

1.1 Mechanical effects of fluids in fault zones

The effective stresses acting in a fluid saturated medium is obtained by subtracting the pore pressure to the stress, following the concept developed in soil mechanics by Terzaghi (1943). Applied to fault mechanics, the Terzaghi's principle is a mechanism for lowering the strength of faults in presence of fluid pressure above the hydrostatic, as was firstly stated for thrust faults by Hubbert and Rubey (1959). Since then, this mechanism has been considered an explanation of many paradoxes of fault and earthquake mechanics, as (i) the low heat flow along active mature faults, such as the SAF (Lachenbruch, 1980; Rice, 1992); (ii) the nucleation of earthquakes on unfavorably oriented faults (Sibson, 1990). Direct evidence of the effects of fluid pressure in fault stability comes from earthquakes induced by injection of fluids down boreholes (e.g., Zoback and Harjes, 1997), or by infilling of water reservoirs (e.g., Simpson et al., 1988). Geological evidence that fluid pressure higher than hydrostatic has been achieved periodically in the crust come from the widespread occurrence of veins in crustal rocks at different depths (Ramsay, 1980; Etheridge et al., 1984; Vannucchi, 2001). Shear zones in particular are recognized as preferential conduits for focused flow of overpressured fluids and mineralization (e.g., Sibson, 1987). Occurrence of multiple vein episodes in fault zones supports the idea that fluid pressure might vary during time in tectonic processes (e.g., Robert et al., 1995; Fagereng et al., 2010). How fluid pressure can be built-up and maintained in the different tectonic contexts is indeed a debated question. One of the hypothesis is that fluid overpressure might result from the sealing of some sectors of the fault zone (Byerlee, 1990). Fluids are also affecting coseismic processes, such as rupture stopping by rapid drops in fluid pressures in dilatational jogs (Sibson, 1985), or cause extreme coseismic fault weakening by thermal pressurization (e.g., Lachenbruch, 1980; Sibson, 1973; Brantut et al., 2008).

1.2 Chemical effects of fluids in fault zones

Fluids exert influence on the fault zones by a variety of chemical effects, such as fluid-assisted retrograde mineral reactions, pressure-solution, crack healing and sealing, cementation, subcritical crack growth. All these effects are interrelated, in that they depend upon possibly thermally activated (endothermic and exothermic) chemical reactions between the rock and pore fluids, as

well as the rate at which dissolved species are transported through the pore fluid (Hickman et al., 1995).

Retrograde metamorphism of fault rock minerals might result in long term weakening of the fault zone, when reaction products are weaker than the reactants. Some examples are the weakening of granite in fault zones due to alteration of feldspar to kaolinite (Evans, 1988), muscovite (Janecke and Evans, 1988) or, at shallower depth, to laumontite (Blenkinsop and Sibson, 1992). The abundance of clays in shallow mature fault gouge is interpreted as due to the preferential hydrolysis of feldspar to phyllosilicates in fault zones. An interesting case is the formation of the Mg-rich smectite clay saponite in fault rocks derived from the alteration of ultramafic protoliths, as found in SAFOD cores (Holdsworth et al., 2011; Moore and Rymer, 2012) and on other fault zones in Japan (Sone et al., 2012). The saponite is an extremely weak mineral (having coefficient of friction of 0.1), and their occurrence has been invoked as an explanation for creep at very low shear strength along the central section of the San Andreas Fault at shallow (< 5 km) depths (Lockner et al., 2011; Carpenter et al., 2011).

Pressure solution is a deformation mechanism occurring in rocks containing an intergranular fluid phase. Under a non-hydrostatic stress, localized dissolution occurs at grain boundaries which support the largest normal stress. Dissolution rate of minerals in an aqueous fluid is indeed higher where a crystal lattice is under high stress, due to the increase of chemical potential with pressure. The dissolved material can diffuse in the fluid, drawn by chemical potential gradient induced by stress differences, to sites of low solubility. Deposition of the dissolved material occurs then at free grain boundaries that are in contact with fluids. In natural fault zones, the minerals which precipitate at free grain boundaries are not necessarily the same which were dissolved, in response to local ambient (P - T) conditions and the chemical composition of the fluid (incongruent pressure solution). Fluid can also migrate to larges distances and deposit material in sites such as veins or strain shadows. Pressure solution processes, are an effective mechanism of accommodating aseismic creep in crustal fault zones (e.g., Gratier et al., 2011). At the same time, they determine the long term strength of fault rocks, since mass transfer processes control the compositional and textural evolution of fault rocks, such the development of foliated rocks (e.g., Jefferies et al., 2006) and furnish chemical species which contribute to fracture sealing (e.g., Gratier et al., 2003). Due to pressure-solution processes, the less soluble species are passively concentrated along planar surfaces which are roughly perpendicular to the maximum principal stress. Compared with other rock forming minerals, the phyllosilicates have lower solubility in most crustal environments, and

this makes foliation surfaces to be relatively enriched in aligned phyllosilicates; this fabric strongly influences the frictional properties of faults, as friction along foliation surfaces has been proved to be much lower than the same material in an isotropic arrangement (Collettini et al., 2009).

1.3 Fluids in the seismic cycle: open questions

The chemical and mechanical effects of fluids on faults are related with the various phases of the seismic cycle. Earthquake ruptures, causing pervasive fractures in the fault rocks (as measured by seismic wave tomography on faults before and after earthquakes (e.g., Brenguier et al., 2008), and as observed in damaged zones of exhumed faults (e..g., Mitchell and Faulkner, 2009), enhance fault permeability. Fluid ingression in the fault zone boosts pressure-solution processes, which are likely to be more efficient between two successive earthquakes and to accommodate some deformation by post-seismic creep. Fracturing and cataclasis reduce the size of the mass transfer between dissolution and precipitation sites, thus increasing the rate of pressure-solution. Sealing of fractures causes pressure-solution processes to be gradually less effective in accommodating creep, due to the increased distance of mass transfer. The fault zone recovers strength and the permeability decreases.

The cyclic evolution of permeability of fault zones has lead to the hypothesis that, after fluid infiltration after an earthquake, they would be trapped due to the subsequent reduction in permeability by (i) sealing of fractures and (ii) compaction of cataclasites and fault gouge. Further reduction of pore spaces by creep and compaction of the fault gouge would allow the fluid pressure to raise until a new earthquake rupture would nucleate, and the cycle starts again (Blanpied et al., 1992; Sleep and Blanpied, 1992; Byerlee, 1993; Gratier et al., 2003; Faulkner and Rutter, 2001). This mechanism has been adducted to explain earthquakes along major, misoriented faults like the San Andreas fault. If the cycle of fluid trapping & pore rise due to sealing and compaction of fault rocks is really applicable to natural faults, and to which extent, this has not yet demonstrated by field evidences. For instance, is this mechanism active in the entire fault, or only in some fault zone compartments? And could this mechanism be efficient at hypocentral depths of major crustal earthquakes (10-15 km)?.

Another effect of fluids in seismic fault networks is earthquake triggering by fluid redistribution and migration, as observed in seismic sequences of the Apennines (Miller et al., 2004; Chiarabba et al., 2009). Identifying the fluid source, and thus the extent of fluid circulation in fault zones, might

constrain at what depth and in which geological context such a mechanism can be active. From stable isotope studies, it has been observed that in deep-seated shear zones, fluids are of local origin and the fluid-rock ratio is low. But in shallower and brittle fault networks, the opening of the system due to rupture propagation might allow ingression of external fluids and high fluid-rock ratios (e.g., Kerrich et al., 1984). The large extent of fluid circulation in brittle fault networks has been proved by geochemical studies in exhumed faults (e.g., Pili et al., 2002), which demonstrated, for instance, the flux of mantle derived fluids in the San Andreas fault system (Kennedy et al., 1997; Pili et al., 2011) and the infiltration of meteoric water in other faults (e.g., O'Hara and Sharp, 2001). Fluid infiltration in seismogenic faults (so during the entire seismic cycle) would possibly be recorded by pseudotachylytes, quenched frictional melts which form coseismically; stable isotope studies in deep seated pseudotachylytes demonstrated that, in those conditions, fluids embedded in pseudotachylytes were of local origin (Moecher and Sharp, 2004). If fluid ingression might trigger earthquake nucleation in other geological contexts, is still not constrained by geochemical evidence.

This thesis aims to contribute to the understanding some of the issues discussed above by integrating microstructural, geochemical and field studies on two cases study:

(i) The San Andreas Fault, which was drilled to 2.7 km depth and gives the unique opportunity to correlate fault microstructures to detailed in-situ measurements of the fault activity. The identification of a cyclic recurrence of pressure-solution creep, hydrofracture and pressure solution creep supports the idea that, in mature fault zones isolated compartments of high fluid pressure might cause low intensity seismicity, associated to the dominant creep activity (Chapter 2).

(ii) The Gole Larghe Fault Zone, an exhumed fault which was active at 9 – 11 km depth. The occurrence of pseudotachylytes allows to investigate the processes occurring at hypocentral depth of major earthquakes (Scholz. 2002). Two topics were investigated: (i) The fabric evolution of cataclastic rocks associated to pseudotachylytes with increasing deformation. This microstructural study aims to identify the (interseismic?) processes leading to the onset of unstable slip. (Chapter 3) (ii) The origin of fluids involved in earthquakes nucleating at 9 – 11 km depth, where, potentially, meteoric fluids might be involved (Chapter 4).

Chapter 2. Physico-chemical processes in the SAFOD phase 3 cores

Abstract

The San Andreas Fault Observatory at Depth (SAFOD) in Parkfield, central California, has been drilled through a fault segment that is actively deforming through creep and microearthquakes. Creeping is accommodated in two fault strands, the Southwest and Central Deforming Zones, embedded within a damaged zone of deformed shale and siltstone. During drilling, no pressurized fluids have been encountered, even though the fault zone acts as a permeability barrier to fluid circulation between the North American and Pacific plates. Microstructural analysis of sheared shales associated with calcite and anhydrite-bearing veins found in SAFOD cores collected at 1.5m from the Southwest Deforming Zone, suggests that transient increases of pore fluid pressure have occurred during the fault activity, causing mode I fracturing of the rocks. Such build-ups in fluid pressure may be related to permeability reduction during fault creep and pressure-solution processes, resulting in localized failure of small fault zone patches and providing a potential mechanism for the initiation of some of the microearthquakes registered in the SAFOD site.

This work was prepared in collaboration with Giulio Di Toro, Jean Pierre Gratier, Jafar Hadizadeh, Steven A. F. Smith, Richard Spiess and published as Mittempergher et al., 2011.

2.1 Introduction

The NSF EarthScope San Andreas Fault Observatory at Depth (SAFOD) in Parkfield offers the opportunity to correlate physical and chemical processes identified in core samples with high-resolution seismological and geophysical data (Zoback et al., 2010). The SAFOD is located in the

transition zone between the creeping segment of the SAF (to the north), and the southern "locked" segment, which lastly ruptured in the 1857 Mw7.8 Fort Tejon earthquake (Fig. 1a). Near Parkfield, the SAF activity includes permanent creep at about 20 mm yr-1 (Titus et al., 2006), microearthquakes (e.g. Nadeau and Johnson., 1998) and moderate (~M6) earthquakes that have nucleated at fairly regular intervals between 1857 and 2004 (e.g. Bakun et al., 2005). The SAFOD main hole crosses the actively deforming SAF at about 2.7km of vertical depth, approximately 100m above the hypocentral area of a cluster of repeating M2 earthquakes, which was one of the targets for drilling (Nadeau et al., 2004). During 2007, about 40 m of core was extracted parallel to the main hole, including a section that crosses the two actively creeping strands of the fault detected by borehole casing deformation, named Southwest Deforming Zone (SDZ) and Central Deforming Zone (CDZ) (Zoback et al., 2010) (Fig. 1a - c).

Slip in the SAF occurs at much lower shear stress than expected based on laboratory friction of rock forming minerals (Brune et al., 1969), suggesting that it behaves as a weak fault in a strong crust (Rice, 1992); such a model is confirmed by down hole stress measurements and mechanical modeling (Hickman and Zoback, 2004; Chéry et al., 2004; Boness and Zoback, 2006). Pressurization of the fault core by pore fluids was one of the explanations suggested for the low strength of the SAF (Rice, 1992). Since no fluid pressure higher than hydrostatic has been detected during drilling (Zoback et al., 2010), the most convincing mechanisms remain the presence of intrinsically weak material within the actively creeping sections (e.g., (Moore and Rymer., 2007)) and the effect of stress driven pressure solution creep processes ((Gratier et al., 2009)). The study of the source mechanisms of repeating microearthquakes in Parkfield at depth of 2 - 5km reveals peak stress drops exceeding 50MPa (Imanishi and Ellsworth, 2006; Dreger et al., 2007), suggesting that relatively strong asperities exist within an otherwise weak fault zone.

2.2 Methods

We performed microstructural, mineralogical and geochemical analyses on samples collected at 1.5m from the south-eastern boundary of the SDZ. The sampled core shows contemporary occurrence of veins and sheared shales (Fig. 1d). Here we provide possible evidence of fracture opening in the presence of fluids and discuss mechanisms for permeability reduction and strength recovery after failure.

The mineral composition has been determined by X-ray Powder Diffraction (XRPD). The data were obtained by step scanning using an automated diffractometer system (Philips X'Change) with incident- and diffracted-beam soller slit (0.04 rad.). The instrument was equipped with a curved graphite diffracted-beam monochromator and a gas proportional detector. Divergence and antiscatter slits of 1/2° were used so that the irradiated area could be confined to the sample at angles >10 °2theta. A receiving slit of 0.2 mm was used. A long fine focus Cu X-ray tube was operated at 40 kV and 30 mA. Diffraction pattern was obtained using a step interval of 0.02 °2theta with a counting time of 15 s. The scan was performed over the range 3–70°2theta. The program High Score Plus (PANalytical) was used for phase identification and Rietveld refinement (Rietveld, 1967). The fine fraction was separated from the bulk powder and treated with ethylene glycol and heated to 200°C and 300°C for clay identification, following the methods described in Moore and Reynolds (1997).

Microchemical mapping was performed on polished thin sections with an Eagle III microfluorescence apparatus located at the Laboratoire de Géodynamique des Chaine Alpine (LGCA) of Grenoble (France). A grid of 256x200 spectra was acquired, with spacing of 55µm in x direction and 61µm in y direction. The fluorescence spectra acquisition was limited to the region of interest (ROI) of the following wavelength: FeK, TiK, MgK, AlK, CaK, NaK, SiK, KK and SK.

Microstructural investigations were performed on carbon-coated, polished thin sections with a field emission scanning electron microscope (FE-SEM) JSM6500F upgraded to version 7000 and equipped with an energy dispersive X-ray spectroscopy (EDS) analyzer with internal standards for quantitative chemical composition (Istituto Nazionale di Geofisica e Vulcanologia, Rome). Backscattered electron (BSE) images were collected at working distance of 10 mm and accelerating voltage of 10 kV; the BSE resolution in these conditions is 4 nm. The EDS electron beam spot size for analysis was 400 nm as estimated by means of Monte Carlo Method simulations.

The microtexture of calcite in veins was investigated by an optical microscope equipped with a Technosyn, 8200 MKII cathodoluminescence apparatus (Laboratoire de Géophysique Interne et Tectonophysique, Grenoble).

The EBSD patterns in calcite were acquired by a CamScan MX2500 SEM equipped with a tungsten filament (University of Padova) and indexed using Channel 5 software by HKL Technology. Indexing was accepted when at least six detected Kikuchi bands matched with those in the standard reflector file for calcite.

Microscopic and macroscopic fractures were discretized by tracing the digital image of the thin section. The discretized curves are composed of nodes, whose position is described by position

vectors in a local reference frame;the nodes are connected by sub-equal segments, whose length is approximately 100-400 micron. To analyze the orientation data, we measured and recorded the orientation of each individualsegment and plotted all of the data on a rose diagram (Figure 2b), following the procedure of Griffith et al. (2011).

2.3 The samples

The damage zone of the SAF is identified in the borehole as a zone of low seismic velocities (Fig. 1c), and is composed of sheared and fractured shales, siltstones and sandstones of the Great Valley Formation (Solum et al., 2006) (Fig. 1b). The studied core section includes sheared Fe-rich shales with embedded veined sandstone ribbons (Fig. 1d). The phase III cores have been drilled along a trajectory parallel to that of the main hole, and we consider the attitude of the main hole axis as a reference to infer an approximate orientation of the sample. Using the foliation in the shale as reference plane and assuming that its attitude is roughly parallel to the SAF plane (Fig. 1d, e), the veins are subvertical and make an angle of 40-100° clockwise with the foliation plane (Fig. 1e, f).

2.4 Observations

The sandstone in the studied core is medium grained (<500μm), composed of clasts of plagioclase, K-feldspar, quartz, mica and bioclasts and cemented by quartz. Pervasive macroscopic and microscopic veins in the sandstone are sealed by calcite and anhydrite; the veins crosscutting the boundary between sheared shale and sandstone are intruded by the shale (Fig. 1f; 2a). The veins oriented at an acute angle to the shale foliation are extensional, while those roughly perpendicular to the shale foliation show extension with a component of sinistral shear (Fig. 1f).

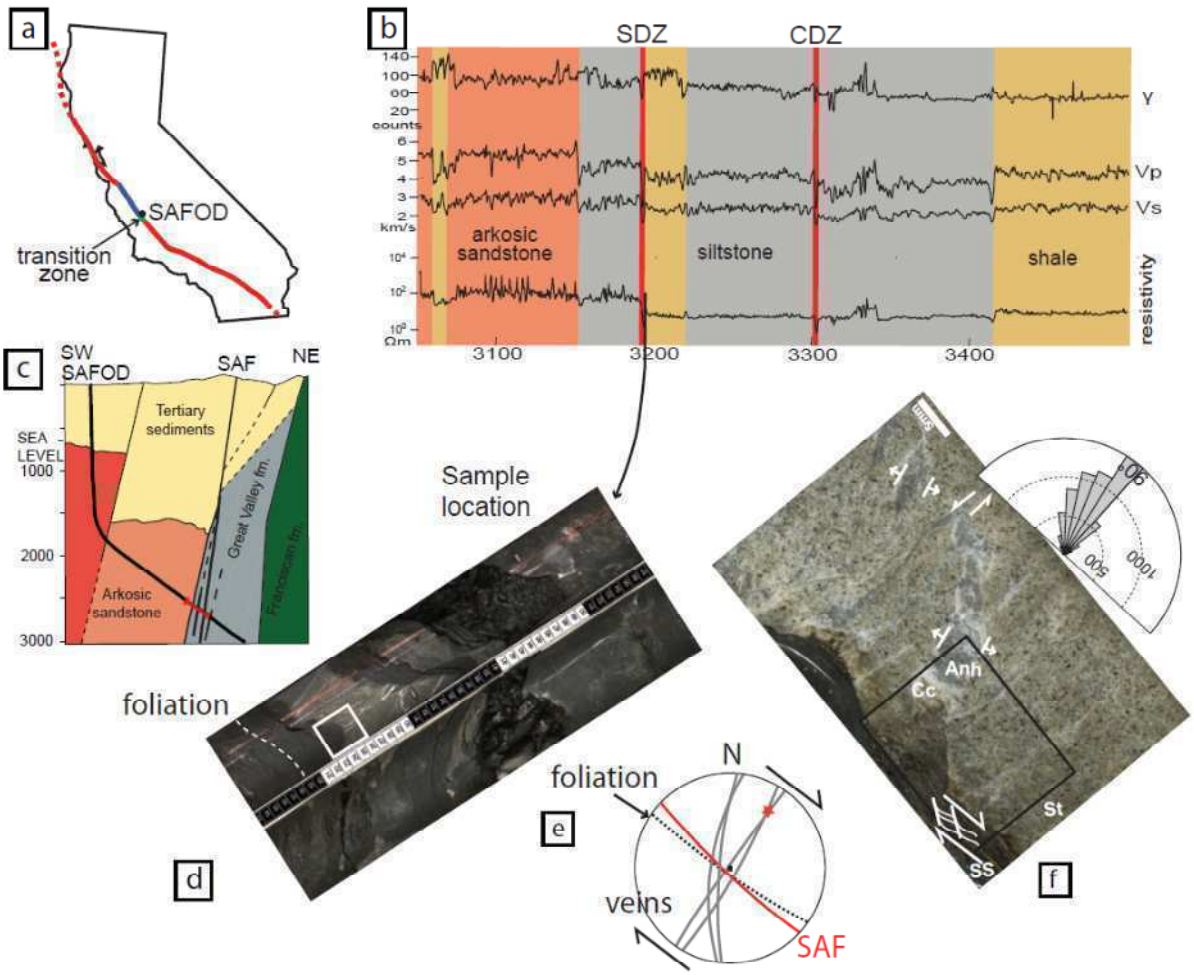

FIGURE 1. Sample location. (a) Sketch of the SAFOD location in California. The SAF is in red (locked segments), blue (creeping section) and green (transition zone). (b) Schematic geological section of the SAFOD site, parallel to the borehole trajectory (thick black line) (Zoback et al., 2010). In red, the segment enlarged in Fig. 1a. (c) The downhole geophysical logs of the SAFOD main hole, with the location of the sample (black arrow). Highlighted in red, the actively deforming fault strands. (d) The studied core section (image from http://www.earthscope.org/observatories/safod/). (e) Lower hemisphere stereoplot of great circles corresponding to the attitude of the SAF in Parkfield (red, datum from (Boness and Zoback, 2006)) and the inferred attitude of the foliation planes in the studied core (dotted line) and the vein planes (gray) (f) Polished thin section, reflected light photomosaic (Cc: calcite, Anh: anhydrite, SS: sheared shale, St: sandstone). Inset: rose diagram of the orientation of the anhydrite-calcite veins, referred to the foliation in the gouge; dashed lines contours the number of counted segments (see AM 1 for details of fracture counting). The black square is the area in Figure 2a.

The sheared shale is composed of illite and illite-smectite interlayers (altogether 48.9%), quartz (18.9%), albite (14.5%), K-feldspar (11.2%) and chlorite (4.9%), with minor calcite (1.1%) and pyrite

(0.5%) (Rietveld XRPD quantitative analysis). The illite-smectite interlayers contain about 20% smectite. The sheared shale is foliated along clay-rich dissolution seams, bended toward the intrusion in the veins (XRF chemical map, Fig. 2a). The material within the foliation planes have smaller grain size and is depleted in Ca, Na, K, Si and enriched in Fe and Mg relative to the less deformed shale. This evolution is seen when comparing the foliation with the initial texture preserved within a strain shadow around a pyrite clast (Fig. 2b). Locally the foliation shows an S-C' texture (Passchier and Trouw, 2005) (Fig. 2c, d). FE-SEM observations show that fibrous, micrometric illite-smectite lamellae have grown in strain shadows around clasts and within intragranular microcracks (Fig. 2d). In the apical part of the veins (Fig. 2a, e) intruded by randomly arranged clays and clasts from the shale layer, the pore spaces are filled by calcite (Fig. 2e). The calcite and anhydrite crystals sealing the veins are mostly euhedral, forming a blocky texture (Passchier and Trouw, 2005), and include domains of elongated crystals (Fig. 3a). Calcite shows thin and straight twins, a texture typical of deformation at temperatures below 200°C (Ferrill et al., 2004). Under the cathodoluminescence microscope, calcite has either dark or light orange luminescence. In the thick vein in Figure 2a, the calcite crystals close to the vein borders have a dark nucleus and a lighter rim and have a blocky texture. In contrast, the calcite crystals towards the vein centre have light rims alternating with dark rims and crystals are elongated with the long axis perpendicular to the vein walls (stretched-fibrous texture) (Fig. 3a). In the latter texture, the associated anhydrite crystals show similar stretched-fibrous crystals associated with microcracks oriented parallel to the long axis of the light and dark luminescence rims in calcite. EBSD analysis on calcite has been performed along the vein borders (blocky calcite, Fig. 3b), and towards the vein centre (elongated calcite, Fig. 3c). The pole figures in blocky and elongated calcite show preferential distribution maximum density of the 'c' axes lower than 2.5 times the mean unit density (MUD), indicating a weak crystallographic preferred orientation (CPO). The blocky calcite is characterized by a weak maximum of the 'c' axes in a direction perpendicular to the vein borders. In elongated calcite, the distribution of 'c' axes shows a minimum parallel to the vein borders, with the 'c' axes plotting within a broad girdle roughly perpendicular to the vein borders.

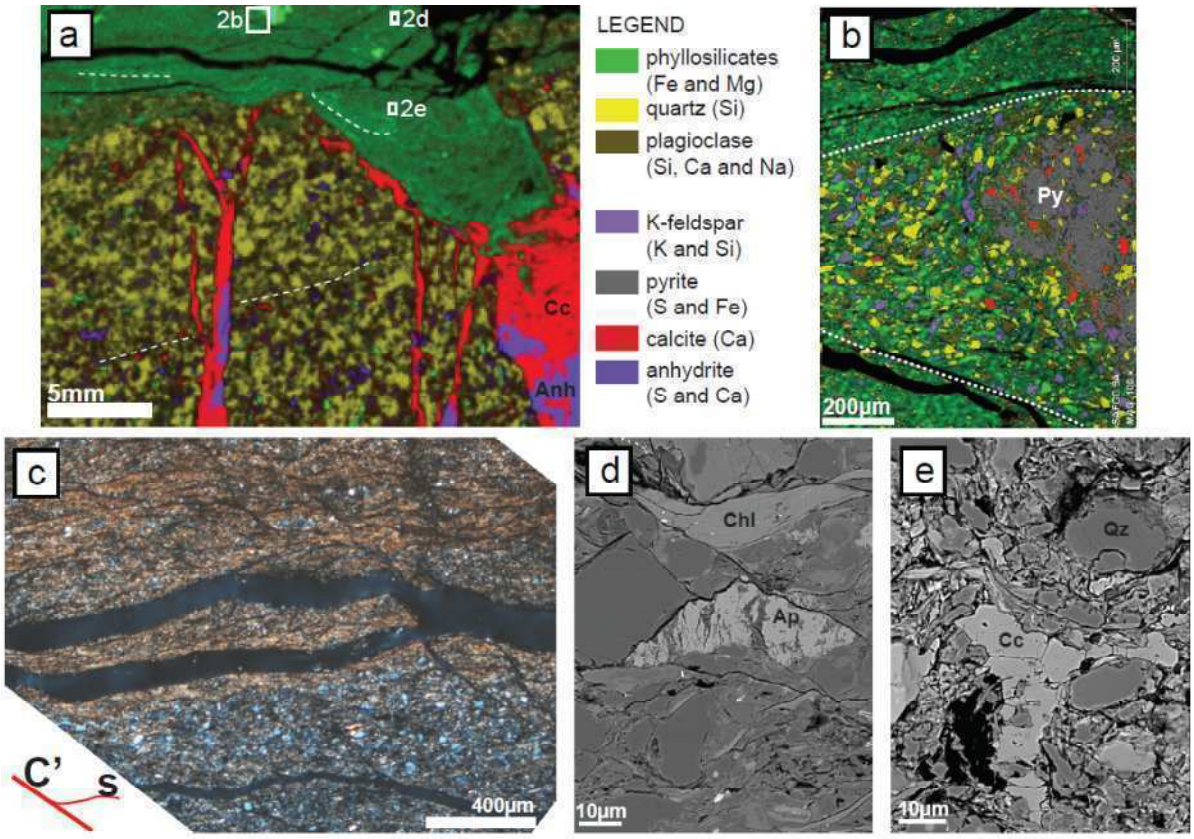

FIGURE 2. Geochemistry and microstructures. (a) Elemental chemical composition by superimposition of XRF chemical maps. Dashed lines: phyllosilicate-rich dissolution seams. (b) Detail of the elemental composition of a strain shadow around a pyrite clast (Py) within the sheared shale. Outside the strain shadow (dashed white line), there is sharp grainsize reduction, leaching of Ca and Si, and passive concentration of Fe and Mg-bearing phyllosilicates (superimposition of SEM-EDS chemical maps). (c) Foliated clay-rich shale with S-C' foliation (optical micrograph, crossed Nicols). (d) Fractures within an apatite (Ap) clast filled by fibrous Illite-Smectite (I-S) lamellae. The S foliation is defined by a chlorite crystal (FE-SEM BSE image). (e) Blocky calcite filling the pore spaces within the shale particles from the apical part of the vein intruding the sandstone (FE-SEM BSE image).

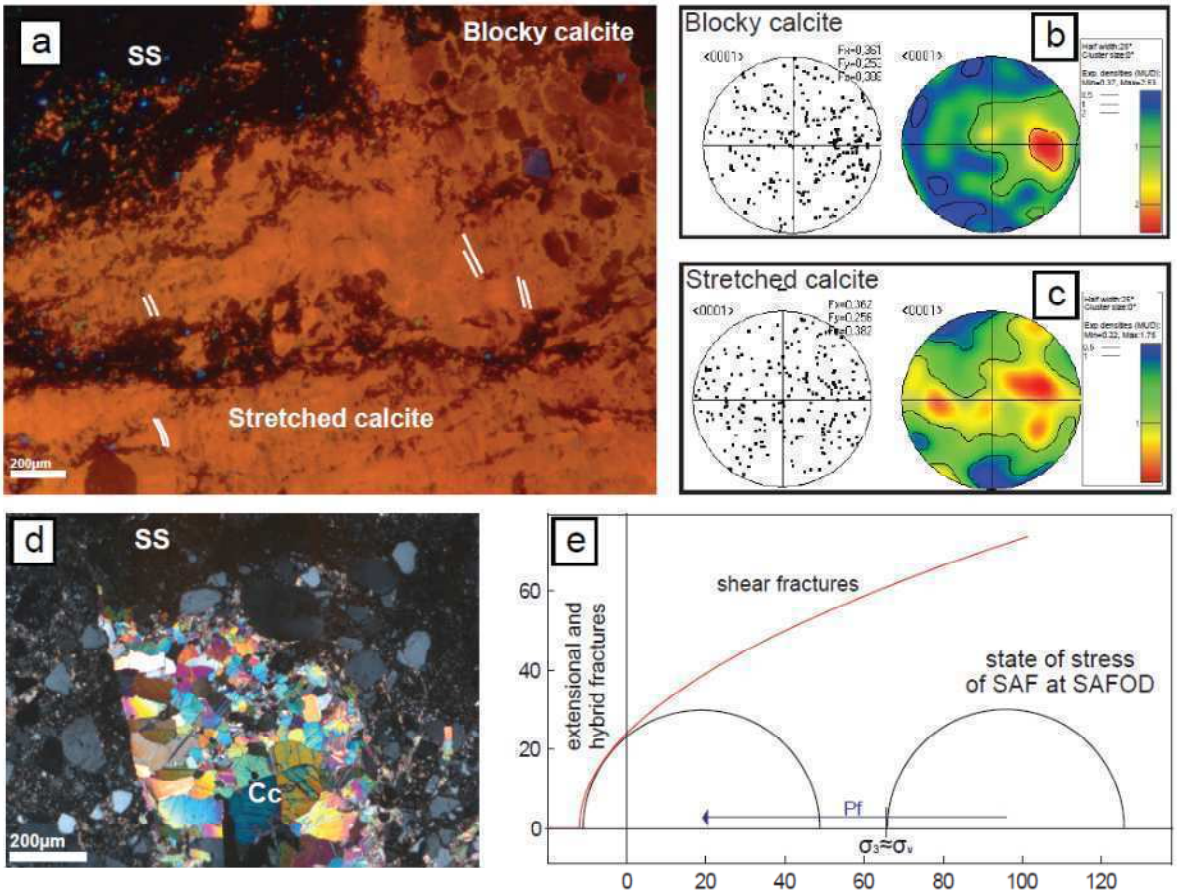

FIGURE 3. Microstructure of the calcite veins. (a) In blocky crystals close to the vein border, calcite is uniformly dark with a thin light rim; in the stretched calcite toward the vein centre, a fine scale banding of light and dark calcite is visible (CL micrograph). (b, c) EBSD data. C-axes orientation plotted in a lower hemisphere stereogram, as scattered data and contour plots; contours are expressed as multiples of mean unit density (MUD); the horizontal line in the pole figures coincides with the long axis of the CL micrograph. (d) Blocky calcite in the apical part of one of the veins, showing pervasive low temperature twinning. (e) Sketch of the Murrell-Griffith criterion of failure and the state of stress in the vicinity of the SAF (from (Hickman and Zoback, 2004)). The conditions for extensional or hybrid fracturing are met when the least principal stress σ3 is negative, after a negative shift due to pore pressure higher than the lithostatic value.

2.5 Discussion and conclusions

The creeping deformation within the SAF is localized within the SDZ and the CDZ. The samples we studied are from the deformed sediments at about 1.5m from the SDZ margin, and thus the deformation structures we described cannot be rigorously related to the active deformation. The location of the microearthquakes associated to the SAF is even less constrained, since they register

static stress drops (up to 120 MPa) compatible with fracturing in relatively strong rocks (Imanishi and Ellsworth, 2006). Therefore, we suggest that the microearthquakes might be localized within the damaged zone, or at the boundaries between creeping zones and damage zone. Here we discuss how the deformation processes active within the siliciclastic sediments in the damage zone can cause local fluid overpressure and brittle failure.

The development of a foliation in the sheared shale is associated with dissolution of quartz and feldspar clasts and growth of clay lamellae in microcracks. These processes are typical of stress driven pressure solution (Gratier et al., 2009), and might cause permeability reduction due to passive concentration of clay minerals such as illite and illite-smectite, clast size reduction and pore space closure at the micrometric scale. The loss of Ca and Na and the passive enrichment in Fe and Mg along dissolution planes due to fault-perpendicular compression is a phenomenon documented at all scales in the SAF damage zone (Schleicher et al., 2009; Gratier et al., 2009). Since dissolution planes are roughly perpendicular to the main compressive stress, they contribute to the development of fault-parallel permeability barriers that may separate compartments with distinct fluid composition, as revealed by abrupt changes in real time mud gas analysis observed during drilling into the SAF (Wiersberg and Erzinger, 2008).

Veining and dilational jogs (consistent with dextral sense of shear of the SAF) in other core sections are sealed by calcite and anhydrite, suggesting that mineral precipitation was related to the SAF activity (SAFOD 2010 core Atlas). The blocky texture of calcite and the intimate intergrowth of calcite and anhydrite in the veins indicate that vein opening was faster than calcite and anhydrite growth (e.g. Passchier and Trouw, 2005), and mineral precipitation occurred into a free fluid in an open vein. This is supported by the weak CPO of blocky calcite with the 'c' axis perpendicular to the vein margins: after nucleation along the vein margins, calcite crystals, which are trigonal and thus anisotropic, grow faster in direction of the 'c' axis. This process would result in a weak CPO due to growth competition (Nollet et al., 2005). The intrusion of sheared shale into the veins is another indication that vein opening was sudden; disruption of foliation and calcite pore fillings within the intrusions suggest that the shale particles were mixed with fluids. The vein texture and their medium to high angle orientation to the foliation in the shale indicate that veins formed either as mode I fractures due to intrusion of pressurized shale material, or as hybrid shear – extensional (Ramsey and Chester, 2004) fractures. Following the Murrell-Griffith criterion of failure (Fig. 3e), to form either extensional (mode I) or hybrid shear – extensional (modeI/modeII) fractures, it is necessary that the effective least principal stress is tensional: $\sigma'3 = (\sigma3 - Pf) < 0$. At about 2.7 km of depth, in the stress

regime of the SAF, which is transitional between strike slip and reverse with σh ≈ σv as in the SAF, these conditions are satisfied when the fluid pressure is higher than lithostatic (Fig. 3e).

After sealing, the veins underwent further deformation, as suggested by twinning and stretching in calcite crystals. In elongated calcite, (1) the fine-scale alternation of light and dark luminescence rims and, (2) the 'c' axis preferentially oriented perpendicular to the vein margin (similar orientation as in the blocky grains), suggest incremental grain growth ("crack-seal",(Ramsay, 1980)), inheriting the orientation of the former blocky crystals (Fig. 3a, b, c). The change in calcite luminescence, which is influenced by traces of Fe and Mn, indicates a modification of fluid composition after the main fracturing episode.

Following these observations, we propose that one of the possible mechanisms of rupture initiation in relatively "strong" rocks embedded within the damage zone of the SAF could be a transient increase of fluid pressure in isolated compartments where the circulation of fluids is limited by fault-parallel horizons consisting of insoluble minerals. Anomalies in the focal mechanisms of two M4 earthquakes in Parkfield area support a non double couple component, suggesting that some seismic ruptures might be initiated in presence of high fluid pressure and then propagate with a dominant shear component (Johnson and McEvilly, 1995). Some of the "asperities" responsible for microearthquakes in the Parkfield segment of the SAF might thus be represented by compartments where the fluids might accumulate due to permeability reduction during compaction and pressure solution processes in clay-rich sedimentary inclusions or fault gouges (e.g., (Sleep and Blanpied, 1992)).

Chapter 3. The fabric evolution with slip in natural cataclasites from seismogenic depths

Abstract

The complexity of the seismic cycle results from the interaction and evolution of stress (tectonic, gravitational, pore pressure, etc.) and fault zone and wall rocks cohesive and frictional strength with time. At seismogenic nucleation depths (7-15 km in the typical continental crust), fault strength and frictional behavior (velocity weakening vs. velocity strengthening) are determined by the fault zone fabric (clast shape and distribution, permeability, etc.), fault mineralogy (weak vs. strong minerals), and the kinetics of fluid rock interactions (weakening vs. healing).

In this study, we investigate the evolution of cataclasites fabric and mineralogy with finite strain (from 0 to about 100) from samples stem from the Gole Larghe Fault Zone (Southern Alps, Italy). The fault zone is exposed in glacier-polished outcrops, is hosted in tonalites and was active 30 Ma at earthquake nucleation depths (9-11 km, 250-280°C). The fault zone is composed of about two hundred sub-parallel main cataclastic horizons connected by a network of minor faults and fractures. Ancient seismicity of the fault zone is witnessed by the occurrence of pseudotachylytes associated to the cataclasites. Nineteen samples were stem from faults/fractures with increasing slip (from 0 to 4.7 m) determined on displaced dykes. Samples were studied by means of microstructural (field emission scanning electron microscope, optical cathodoluminescence), mineralogical (X-Ray powder diffraction), geochemical (Energy Dispersive X-Ray Spectroscopy) and image analysis (clast size distribution and shape parameters) investigations to quantify the evolution of fabric with slip and discriminate the different physico-chemical processes active during the seismic cycle.

With increasing finite strain, the average grain size decrease, the fractal dimension increases (from 1.6 to 2.4 in two dimensions) and the faults develop multiple domains of foliated cataclasites and ultracataclasites. If ultracataclasite is present, thinning of the fault zone suggests localization and possible strain weakening behavior. Fluid-rock interactions are widespread in the faults and

damaged tonalite, enhancing pressure-solution processes overprinting the cataclastic texture. Fluid rock interactions allow part of the deformation to be accommodated by pressure-solution driven aseismic creep.

3.1 Introduction

Brittle fault zones are decorated by a layer of granular material formed by wearing of the fault walls during sliding, which, in the case of typical crustal geothermal gradients, is incohesive (fault gouge) at shallow depths (down to 3-7 km), or cohesive due to induration by hydrothermal minerals (cataclasites) at larger depths (up to 10-15 km) (Sibson, 1977; Scholz, 2002). The fragmentation processes operating during shear on the granular material determines the grain size distributions (Sammis et al., 1987; Blenkinsop, 1991; Storti et al., 2003; Billi, 2005) and grain shapes (Storti et al., 2007; Heilbronner and Keulen, 2006). With increasing shear strain, the particle size distribution evolves to (i) fractal dimensions *D* larger than 3 (in three dimensions), (ii) smaller grain sizes (Blenkinsop, 1991), and, (iii) more rounded shapes (Storti et al., 2007; Heilbronner and Keulen, 2007). The macroscopic frictional behavior of granular materials is controlled by interactions between particles (e.g., Biegel et al., 1989; Hazzard and Mair, 2003), and is thus strongly dependent on the mechanical properties (e.g., indentation hardness), size and shape of the particles. Friction experiments on simulated gouge (Mair et al., 2002) and 3D modeling (Abe and Mair, 2009) demonstrated that a gouge composed of angular fragments has an higher friction than one composed of spherical fragments. Experimental studies on simulated fault gouge demonstrated that there is an evolution in the macroscopic frictional behavior with increasing displacement, as a consequence of the evolution of particle size distribution (e.g., Biegel et al., 1989) and the onset of localization of the deformation (Beeler et al., 1996; Logan et al., 1992). This behavior is of crucial importance in fault mechanics, since the evolution of fault material with increasing strain can be a factor controlling slip instability in natural fault zones. In natural faults, the fabric of granular material controls also the porosity and permeability of the fault zone, influencing its hydraulic transport properties (Faulkner and Rutter, 2001). On the other hand, the interaction with percolating fluids is a major factor in controlling the fabric of natural crustal faults and fault healing (Blenkinsop, 1991; Blenkinsop and Sibson, 1992; Gratier et al., 2002).

Here, we attempted to evaluate the effects of increasing shear strain on the fabric of small displacement faults in an ancient seismogenic fault hosted in tonalites and active at 9-11 km depth,

typical earthquake nucleation depth in the continental crust. The samples were collected in the Gole Larghe fault and analyzed by means of quantitative microstructural measurements, Scanning Electron Microscope (SEM) Back Scatter Electron imaging and SEM Energy Dispersive X-Ray Spectroscopy (EDS) equipped SEM for chemical mapping. An increase in the fractal dimension of the clast size distribution with slip, coherent with experimental results, is measured. Possible strain localization (and weakening) is found in extremely comminuted cataclasites. Pressure-solution processes, activated by fluid infiltration upon faulting, overprint the cataclastic texture, allowing further strain to be accommodated by aseismic creep.

3.2 Geological setting

The Gole Larghe Fault is a dextral transpressive fault zone which cuts across the northern Adamello batholith, in the Southern Italian Alps (Figure 1a). The fault zone structure was extensively described in Di Toro and Pennacchioni (2004; 2005) and Pennacchioni et al. (2006). From regional (pseudotachylyte Ar-Ar dating, host rock dating and fission track studies, mineral assemblages in the Adamello metamorphic aureola), microstructural (evidence of incipient crystal plasticity in quartz in cataclasites) and mineralogical (mineral assemblages in cataclasites) constraints it is inferred that the fault was active at 9-11 km depth, after cooling of the host Avio tonalite, at an ambient temperature of 250-300°C (Di Toro and Pennacchioni, 2004; Pennacchioni et al., 2006). The Gole Larghe Fault is composed of hundreds of cataclasite- and pseudotachylyte-bearing fault strands which exploit pre-existing joints. The Gole Larghe Fault dips on average 65° towards N195° and the lineation has pitch of 35° to the West. Joints are pervasive within the Avio tonalite outside the fault zone, and organized in two main sub-vertical sets striking about E-W and N-S. In both sets, joints are spaced apart of 0.5-3 m (Di Toro and Pennacchioni, 2005). North-South (less commonly the E-W set) striking joints are locally activated as amphibolitic facies mylonites (Pennacchioni, 2005). Instead, in the fault zone, the East-West striking joints are usually exploited as sub-greenschist facies cataclasites and pseudotachylytes (Di Toro and Pennacchioni, 2005) and zeolite facies faults (Pennacchioni et al., 2006; Dempsey et al., 2011). From previous microstructural and field investigations (Di Toro and Pennacchioni, 2004; 2005), it is known that pseudotachylytes, which are quenched frictional melts associated with seismic sliding (Sibson, 1975), are mostly associated with green in color cataclasites. The ‘re-activation’ of joints and the formation of a network of cataclasite-bearing faults in between the major sub-parallel joints usually predates pseudotachylyte formation

(Di Toro and Pennacchioni, 2005) (Figure 1b) though there is evidence of fault segments hosting pseudotachylyte without the presence of cataclasites (Pittarello et al, 2008).

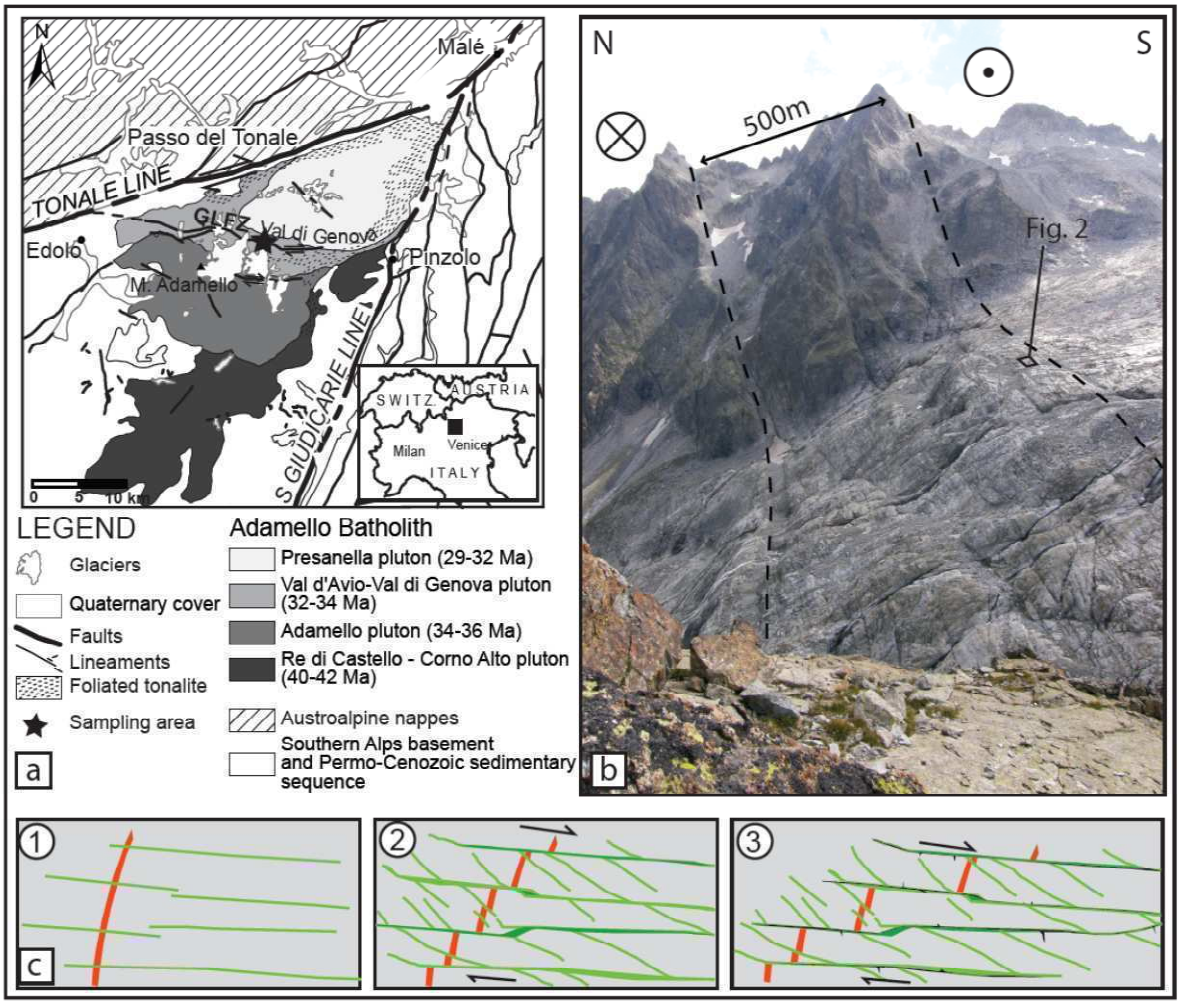

FIGURE 1: Geological setting of the Gole Larghe Fault Zone. (a) Simplified geological map of the Adamello area with location of the sampled outcrop (shown in detail in Fig. 2). (b) View of the fault zone from the west; the fault is composed of a set of about two hundred sub-parallel main faults, which exploits pre-existing joints. Joints cutting the tonalite are clearly visible outside the fault zone boundaries (to the left and to the right of the dashed lines). (c) Sketch of the possible evolution from joints (1) to pseudotachylyte-bearing faults (3), through the formation of green cataclasites (2). Pseudotachylytes, associated to seismic ruptures, record usually the last deformation event recorded by most of the individual Gole Larghe main faults.

3.3 Methods

3.3.1 Field survey and sampling

A flat glacier-polished outcrop in the southern side of the fault zone (Figure 1b) was chosen for detailed field mapping and sample collection. The outcrop was mapped over an area of 20 m^2 by a mosaic of photographs taken in a rigid 60x40 cm rectangular reference frame, which was successively used for rectifying the pictures. The fault structures were digitized in an ArcMap project.

Nineteen samples were extracted from the outcrop using a driller with diamond drill bits (20 or 40 mm in diameter). Drilling locations were chosen in order to have a complete set of displacements from zero (at the outcrop scale) to 4.3 m, and fault strikes spanning over 55°. The samples were stem preferentially where the separation of the markers (aplitic dykes) was measured. The slip vector (lineation of the cataclasite fault surfaces) was not parallel to the outcrop surface, so it was necessary to convert by trivial trigonometry (i.e., relationships between the attitude of the outcrop surface, attitude of the structural marker, attitude of the fault surface and of the slickenlines, see Di Toro PhD 2003 thesis), the separations measured on the outcrop to displacements (Table 1). It was not possible to measure the attitude of the lineation all faults, since most of the fault surfaces were not exposed in the flat surface; however, the lineation measured over the whole fault zone, including major and minor faults, is rather constant (35^{o} to the west), so a mean lineation with pitch 35° to the west was used for calculations (Di Toro and Pennacchioni, 2005).

3.3.2 Thin section study

Polished thin sections were cut perpendicular to the fault surface and parallel to the average lineation, after sample consolidation with epoxy. The thin sections were examined under the optical microscope for textural description. Scans of the thin sections acquired under the optical microscope (plane polarized and crossed polarized light) were used to manually map the orientation of microcracks and dissolution seams. Microcracks and dissolution seams were traced using a GIS program, then the orientation data were plotted using the function rose.m in MatLab ®. The microfractures related to the fault activity were distinguished from those induced by sample

preparation based on their fillings: only fractures bearing either fluid inclusion trails or a mineral assemblages compatible with that cementing the cataclasites at 9-11 km depth were traced.

Cathodoluminescence images of selected zones were obtained using an optical microscope equipped with an OPEA Cathodyne system (spectral range 170 to 2000 nm) installed at the ISTerre, University of Grenoble. Cathodoluminescence microscopy allows to identify subsequent phases of growth in minerals, due to the possible occurrence of chemical impurities which influence the electron luminescence of the minerals (Marshall, 1988).

Microstructural investigations on carbon coated thin sections were performed in two SEM apparatuses: a CamScan MX2500 SEM equipped with a tungsten filament or a LaB_6 source (Dipartimento di Geoscienze, University of Padova) and a field emission scanning electron microscope (FE-SEM) JSM6500F upgraded to version 7000 (INGV, Rome). Both devices are equipped with an energy dispersive X-ray spectroscopy (EDS) analyzer; spot analyses were collected for mineral phase determination and chemical maps were collected on selected areas (see § 6).

3.3.3 Image analysis

Scanning Electron Microscope-BSE images are suitable for image analysis studies, because, once the mineralogy is known, it is possible to associate a gray intensity to a mineral phase and map its distribution over the image. The cataclasite rocks studied here have quite constant mineral composition, so this method can be easily applied. We used image analysis techniques for measuring the clast size distribution (CSD) of the clasts of plagioclase and quartz, to analyze the shapes of clasts and to measure the modal composition of the fault rock assemblage.

Clast size analysis

The SEM-BSE images were acquired at magnifications of 100x, 300x and 400x. Scanning Electron Microscope images were segmented to gray levels corresponding to the values of quartz and plagioclase using the threshold function of the Image analysis toolbox of MatLab® and of the software ImageJ (downloaded for free from http://rsbweb.nih.gov/ij/). The binary images were stacked over the original SEM images and manually corrected for defects such as holes due to the sample preparation, changes in brightness due to electronic gun “instabilities” and charging effects along grain boundaries. The areas of the particles with area greater than 25 pixel were then computed using the built-in function in ImageJ, excluding the particles along the edges of the image. The threshold of 25 pixel was chosen because smaller particles cannot be resolved on the SEM

images, so it was not possible to check if the particle was truly a clast or, for instance, a hole or dust on the polished surface.

The area *A* of the particles was scaled to the pixel size in microns and the equivalent circular diameter d_{eq} was calculated as:

$$d_{eq} = 2\sqrt{A/\pi} \qquad \text{(Eq. 1)}.$$

The cumulative distribution curve of the equivalent diameters was then calculated and plotted in a log-log graph. To combine data for the same sample but collected at different magnifications, the cumulative number was normalized with the area of the analyzed image, corrected for the boundary particles (i.e., the particles truncated by the edge of the image were not considered). Images at 100x were chosen for computing the slope of the cumulative curve in the log-log plot because they cover a range of grain sizes which overlaps between fine grained built and coarse grained built studied fault rocks. The slope of the curve was calculated in a clast size range chosen to avoid particle sub-sampling towards the grain size limits, either due to sub-sampling of small particles due to the low resolution of the image, or due to sub-sampling of the large particles due to the small area investigated.

Particle shape analysis

The binary images corrected for measuring the CSD were used also for the analysis of the particle shapes. For particle shapes, a lower threshold of 200 pixel was chosen, because, for smaller particles the effects of the shape of the pixels is not resolvable from the effects of the overall shape of the particle (e.g., Bjork et al., 2009).

The binary images were analyzed using the program ImageJ (Fiji version) and the plug-in Particle8 designed by Landini (2006). The advantage of this program is that it computes both the area and the convex hull of a particle using the same method (Freeman's algorithm), so that they are directly comparable. Many of the shape parameters used to describe the roughness of the particle outlines are based on the comparison between the actual perimeter (or area) of a particle and the length (or area) of its convex hull. If the perimeter of a particle is computed for instance by pixel counting and the perimeter of the convex hull is computed as a vector polygon connecting the particle edges, in some cases the length of the convex hull might be smaller than the perimeter length. This leads to unrealistic convexities, or the ratio between the perimeter and convex hull, in excess of 1.

After testing the effectiveness of the shape parameters calculated by the software, we choose the parameters (aspect ratio, orientation of the long axis, solidity, etc.) which were the more robust and better described the cataclasite fabric.

Modal mineralogical composition by point counting

In most samples, given the limited thickness (often < 2 mm) of the cataclasites and the presence of several microstructural domains (foliated cataclasites, ultracataclasites, etc,), it was not possible to obtain enough powder to determine the modal content of individual domains by means of X-ray powder diffraction (e.g., Rietveld method). At the same time, given the very similar tone of gray of epidote and chlorite, the esteem of mineral modal composition by phase mapping of SEM BSE images was not possible. For this reason, we estimated the modal composition by point counting in the images at magnitude 400x used for measuring the particle sizes. At 400x, it was possible to distinguish chlorite and epidote by eye, due to the different mineral habitus. At least 600 random points were counted for each image, and the counting was stopped when there were no more fluctuations in the distribution plot of the mineral phases.

3.4 The mapped outcrop

The mapped outcrop is located close to the southern boundary of the Gole Larghe Fault zone (Fig. 1b). In this area, the fault zone is composed of two sub-parallel main faults, spaced 2 m apart and a network of minor fractures/faults in between. The main faults dip on average 65° to N190°, roughly parallel to the E-W striking main joint sets measured in the area outside the fault zone (Di Toro and Pennacchioni, 2005) (Fig. 1b and Fig. 2b). The outcrop was chosen because (i) it is flat, so its straightforward to map the surface,(ii) there are several dikes, almost perpendicular to and cut by the main and minor faults/fractures. As a whole, the mapped outcrop has a finite strain $\gamma = 5.48$ (cumulative displacement δ= 15224mm, outcrop thickness, 2w = 2777.3 mm) , distributed over two main faults, which accumulate most of the deformation (4796mm + 1759mm = 6555mm or 43% of the cumulative displacement in the selected area) and at least 85 minor fractures which cut across the dyke marker. All the faults in the map bear cataclasites, whereas pseudotachylytes, at the outcrop scale, are found continuously on the main faults and, discontinuously in some segments of the minor faults.

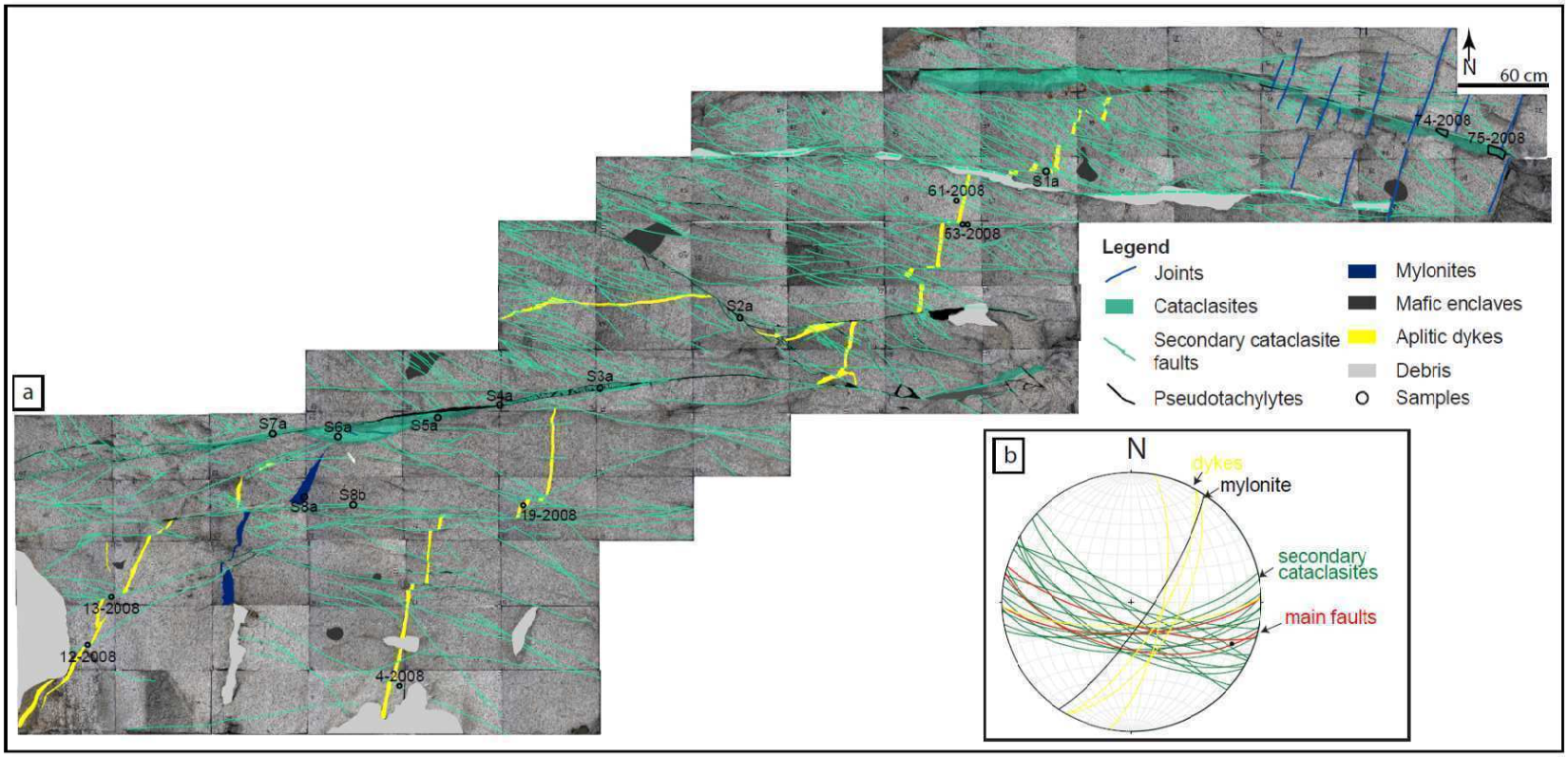
a
N
60 cm
74-2008
75-2008
S1a
61-2008
63-2008
S2a
S3a
S4a
S5a
S6a
S7a
S8a
S8b
19-2008
13-2008
12-2008
4-2008
Legend
Joints
Cataclasites
Secondary cataclasite faults
Pseudotachylytes
Mylonites
Mafic enclaves
Aplitic dykes
Debris
Samples
b
N
dykes
mylonite
secondary cataclasites
main faults

FIGURE 2: Surface map and structural data of the selected glacier-polished outcrop (for location, see Figure 1b). (a) Surface maps covering 20 m^2 and made by photomosaic of 82 orthorectified photos using a 40x60 cm frame as reference (see methods section) . (b) The orientation of representative structural elements measured over the selected outcrop. Lower hemisphere, equal angle stereoplot.

3.5 Fault rocks

We focused on the (1) main fault and (2) on the minor faults and fractures within the two main faults. The dense network of minor faults and fractures (Fig. 2) is absent outside the fault zone, suggesting that it results from brittle faulting and that most minor faults are Mode II and III cracks (i.e., these minor faults and fractures are not due to cooling or other late-magmatic processes, see Di Toro and Pennacchioni, 2005). The first macroscopic effect of the increasing deformation on cataclasites is the increase in thickness and the development of an internal layered structure. The cataclasites evolve from very thin (few millimeters thick), chlorite- and epidote-bearing mono layered fractures cutting across a weakly deformed and poorly altered tonalite, to multi layered cataclasites bearing one or, sometimes, two or three pseudotachylyte-bearing layers surrounded by a damaged and often intensely altered tonalite,.

The surface map and thin section scans were used to estimate the local thickness of the faults, estimated as area of the cataclasites divided by the length of the fault segment. The finite strain γ accumulated by the cataclasite horizon was estimated as

$\gamma = \delta/2w$ (Eq. 2)

where γ is the finite shear strain, δ is the displacement and w is the half width of the shear zone. The displacements, thickness and shear strains of the studied samples are listed in Table 1. Fault rocks are mostly cataclasites, i.e., fragmented host rock cemented by hydrothermal minerals including chlorite and epidote, which give a macroscopic green color to the rock (for definition of the fault rocks we refer to Sibson, 1977). Layers of finer grained material, macroscopically white in color, are identified as ultracataclasites. Pseudotachylytes are macroscopically dark brown – black in color and overprint the cataclasites (Di Toro and Pennacchioni, 2004; 2005).

The thickness of the minor faults with δ < 500mm are plotted against the displacement in Figure 3. Ultracataclasite-bearing faults plot in the lower part of the diagram, suggesting that, if ultracataclasites are present, more deformation is accommodated without an increase in fault thickness.

Sample	Fault rocks	Dip (°)	Dip direction (°)	Separation (mm)	Displacement (mm)	Thickness (mm)
M37	extensional joint	88	205	0	0.0	1.0
61-2008	cataclasite	60	211	1	1.0	0.4
19-2008	cataclasite ultracataclasite	87	27	22	33.9	0.4
4-2008	cataclasite	85	26	24	38.0	1.4
12-2008	cataclasite	70	170	47	77.1	1.4
53a-2008	cataclasite	58	195	98	120.2	2.1
53b-2008	cataclasite	58	195	98	120.2	2.1
S1a	cataclasite	75	220	99	130.1	4.7
	cataclasite	80	190	91	131.8	1.6
13-2008	cataclasite	58	177	115	152.6	0.9
S8b	cataclasite ultracataclasite	65	191	315	357.1	1.6
SM9-2008	cataclasite ultracataclasite	70	176	320	410.1	1.1
S3a	cataclasite pseudotachylyte	60	182	1352	1648.2	
S7a	cataclasite pseudotachylyte	70	183	1352	1648.2	
S6a	cataclasite pseudotachylyte	76	196	1352	1648.2	
S5a	cataclasite pseudotachylyte	74	167	1352	1648.2	
S4a	cataclasitepseudotachylyte	70	178	1352	1758.5	
SM-03-10	cataclasite	85	192	1310	2562.7	13.0
74-2008	cataclasite pseudotachylyte	60	193	4300	4796.1	68.1

TABLE 1. List of the samples.

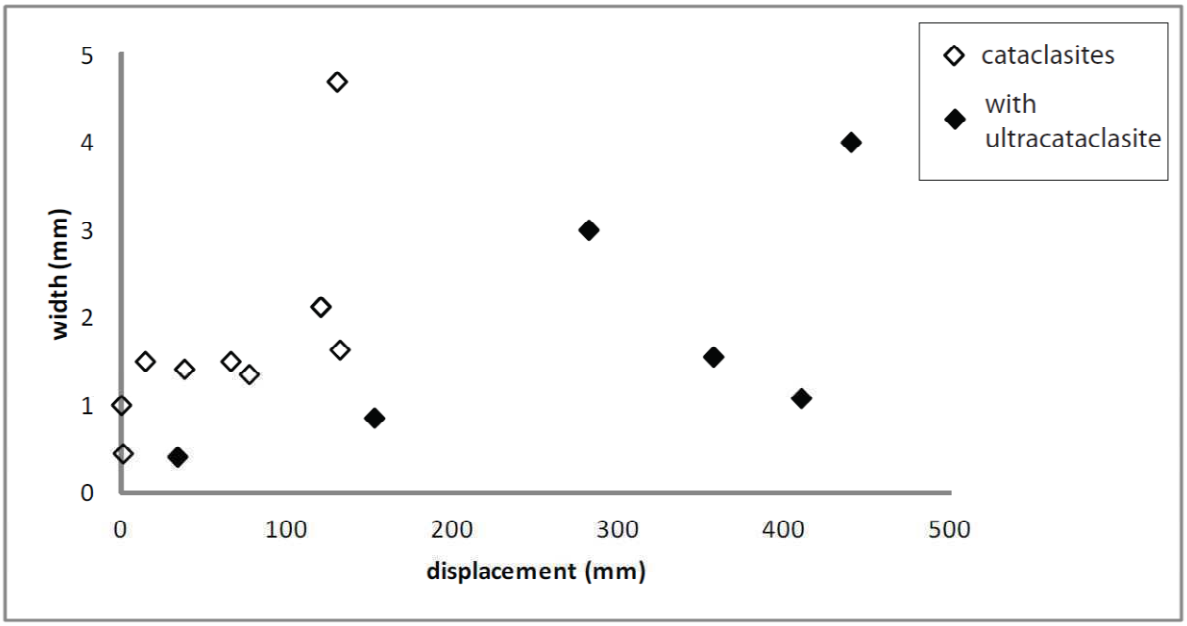

FIGURE 3: Thickness vs displacement of the sampled faults with displacement lower than 500mm. Cataclasites bearing an ultracataclasite layer are, for a given displacement, relatively thinner than cataclasites without an ultracataclastic layer. This evidence suggests strain localization in ultracataclastic layers.

3.6 Microstructures

3.6.1 Cataclasites-bearing minor faults

Cataclasites are composed of clasts of plagioclase, quartz and K-feldspar, in a matrix of K-feldspar, epidote and chlorite in variable proportion (see § 7). The microstructure of the cataclasites changes significantly with shear strain and include cataclasites, foliated and non folitated ultracataclasites are rare pseudotachylytes. Here we describe the textures of three representative samples which experienced increasing shear strain (Figure 4).

In cataclasites which experienced low finite strain (γ= 1, sample 61-2008 in Figure 4a), the clasts are mostly angular and elongated, with cuspate-lobed margins, due to grain dissolution and growth of the matrix minerals along their borders (see section 7). The tonalite bounding the minor faults is cut by fractures departing from the fault. Apparently, the shape of the clasts in the cataclasite layer (Fig. 5a) is controlled by the geometry of the microfractures in the tonalite walls, which limit lozenge or rectangular shaped, cuspate-lobed, elongated clasts (Figure 5a).

With increasing shear strain cataclasites become thicker and multiple domains are developed. In sample 53a-2008 with γ = 57 (Figure 4b), along the fault walls, a cataclastic texture similar to that found in sample 61-2008 is preserved. But towards the fault core, a fine grained (grain size < *10μm*) layer of foliated S-C' cataclasite is found. The S foliation is defined by elongated ribbons of plagioclase and quartz clasts, with wavy boundaries and jagged in the direction perpendicular to the S surfaces, alternated with 10-20 micron thick layers of matrix minerals (epidote, chlorite and K-feldspar, for details see § 7). The C' shears are discontinuous and strike at low angle to the fault walls, and include dragged micron-sized fragments of cataclasite minerals, mostly chlorite (Figure 5b). The sample 19-2008 (Figure 4c), which experienced higher shear strain (γ = 82), bears a 0.4 mm thick cataclasite - ultracataclasite layer. The ultracataclasite is foliated and non-foliated. The foliated ultracataclasite is present along most of the fault core and is similar to the S-C' foliated cataclasite found in sample 53a-2008 with γ = 57 (Figure 4b). The non-foliated ultracataclasite is made of rounded grains, with average size of 5μm and occurs in discontinuous domains along the fault and continuously in fractures departing at high angle from the fault (Fig 4c; 5c). We interpret the non-foliated microstructures as probably pristine cataclastic features preserved from alteration and chemical reactions under a gradient of stress; instead, alteration and intense fluid-rock interaction occurred in the foliated cataclasites (see § 7).

FIGURE 4: Microstructures of cataclasites with increasing finite strain. (a) SEM-BSE image of a fault with 0.4 mm of displacement and γ = 1 (sample 61-2008). It is composed of lozenge shaped clasts, preferentially aligned with the long axis parallel to the fault margins, in a matrix made of epidote, chlorite, K-feldspar. Similar lozenge shaped grains are found in the wall rocks bounding the faults (Fig. 5a). (b) SEM-BSE image of a fault with 120 mm of displacement, with γ= 57 (sample 53a-2008). Compared with (a), the fault is much thicker and foliated. The foliation is defined by iso-oriented and boudinaged clasts of plagioclase and quartz and by banded matrix minerals (epidote, chlorite, K-feldspar). The grain size decreases from the fault margins towards the center (where the sample was split). (c) SEM-BSE image of a fault with 34 mm of displacement with γ = 82 (sample 19-2008). Ultracataclasite is dicontinuosly present along the fault wall and fills cracks in the wall rocks. Elsewhere, the fault rock is a foliated, fine grained cataclasite.

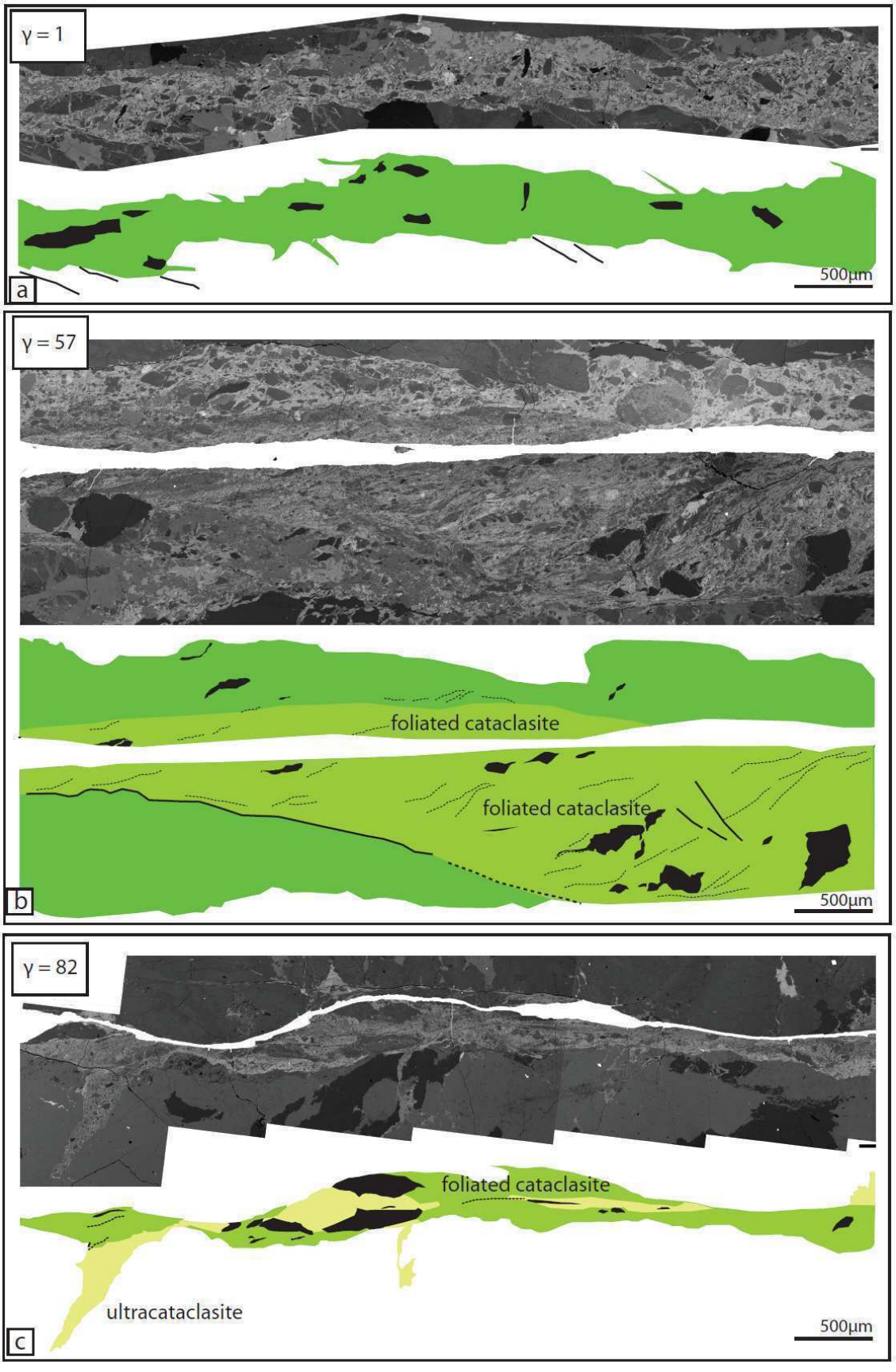
γ = 1
500µm
a
γ = 57
foliated cataclasite
foliated cataclasite
500µm
b
γ = 82
foliated cataclasite
ultracataclasite
500µm
c

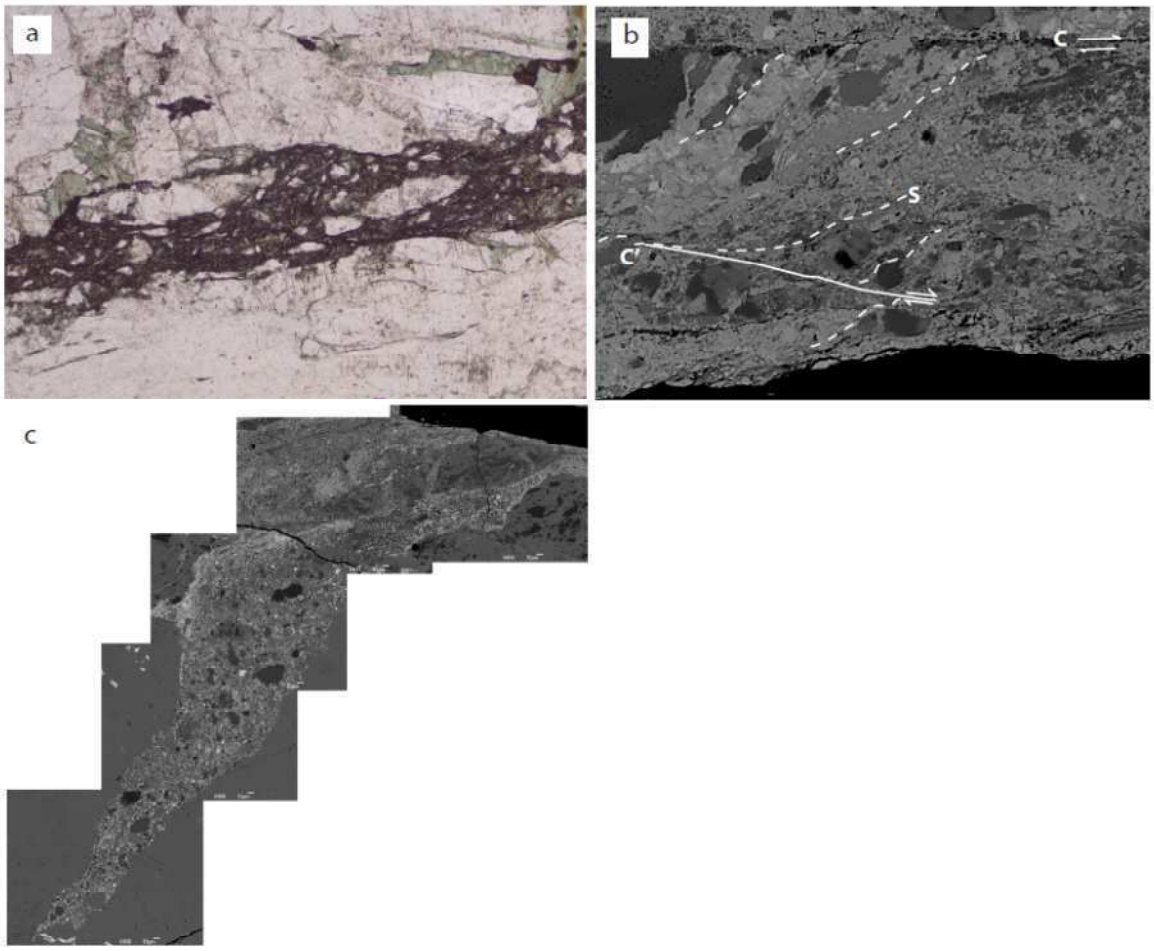

FIGURE 5. Details of the samples shown in Figure 4 (all SEM-BSE images). (a) Sample 61-2008, with γ = 1, detail of tensional fractures in host tonalite with formation of elongated clasts due to the growth of chlorite and K-feldspar in the fractures. With deformation and fluid-rock interaction these clasts are progressively included in the fault. (b) Sample 53a-2008, with γ= 57, detail of the foliation, with dragged micron sized clast fragments in C and C' type shears. (c) Sample 19-2008, with γ = 82. Ultracataclasite filling a fracture departing at high angle from the fault.

3.6.2 The damaged tonalite around minor faults

The tonalite around small displacement faults is characterized by pervasive microfracturing. Microfractures are either sealed by chlorite and K-feldspar (see § 7), or, inside quartz grains, healed by fluid inclusion trails. The microfractures are mostly clustered in two sets, one striking at low angle to the fault surface and one at 30 – 70° to the fault (Figure 6). With increasing slip, most microfractures tend to be oriented at about 30° clockwise from the fault, consistently with possible

orientation of the principal horizontal stress responsible for the dextral sense of shear of these minor faults.

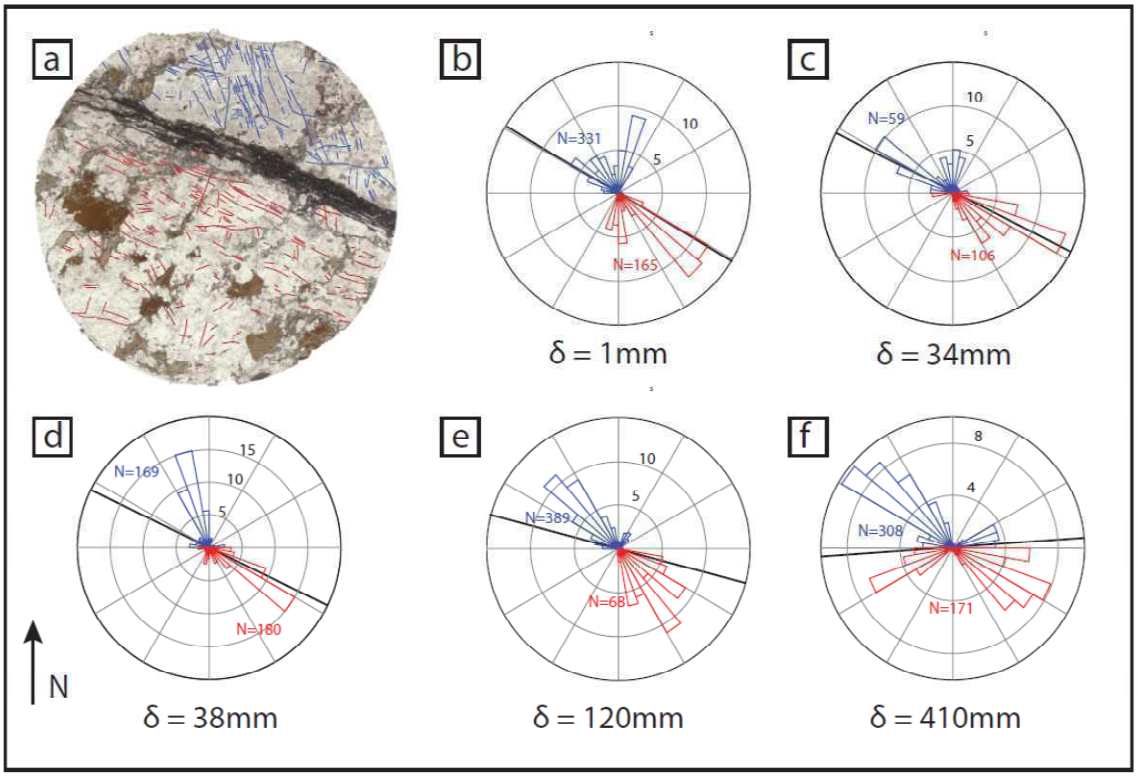

FIGURE 6: Microfractures filled by chlorite+K-feldspar or healed by fluid inclusion trails bounding the minor faults. (a) Thin section scan of a fault (sample 04-2008) with displacement of 38mm, with microfractures traced in red (southern side) and blue (northern side). The strike of the microfractures for this particular fault is represented in the rose diagram in d). The fracture frequency is normalized on the total number of fractures on each side and the number of measured fractures is reported in the rose diagrams (since the areas covered by the thin sections are different, the fracture intensity is not represented in these diagrams). (b) to (f), rose diagrams for microfracture orientation in tonalites bordering minor faults with increasing slip.

3.6.3 Cataclasite-bearing main faults

The main faults, which accommodated more than 1000 mm of displacement, are much thicker (several centimeters thick) than minor faults/fractures and composed of several cataclasite, foliated and non-folitated ultracataclasite and pseudotachylyte layers (Figure 7). In sample 75-2008, which accommodated 4796 mm of displacement, we recognize two layers of ultracataclasite (uc, one light brown and the second black in color under the optical microscope), a pseudotachylyte layer (pt, brown in color), crosscutting a cataclasite layer (cc) (Figure 7a, b). The thick layer of cataclasite

borders the fault walls (cc) (Figure 7a, b). The pseudotachylyte veins are the last deformation event, because they overprint the ultracataclasite and include elongated clasts of ultracataclasite. K-feldspar + chlorite veins (in pink in Figure 7b). Based on the crosscutting relationships, the succession of deformation events is: cataclasite, ultracataclasite, veining and pseudotachylyte.

Cataclasites are composed of clasts of plagioclase and quartz in a matrix of epidote, chlorite and K-feldspar (Figure 7d). Clasts are sub-angular, and sometimes show a pervasive internal fracturing as it is highlighted by cathodolumunescence imaging (Figure 8).

In ultracataclasites, quartz and plagioclase clasts have more regular boundaries and are overall rounded in shape. There are two domains of ultracataclasite, one cemented by chlorite, K-feldspar and chlorite (Figure 7c, light green in the sketch in Figure 7b), one cemented by dominant K-feldspar (Figure 7e, light yellow in Figure 7b).

Pseudotachylytes have a very different texture: clasts are well rounded, few large clasts of quartz and plagioclase are preserved, while the average size is much smaller than the one found in the cataclasite and ultracataclasite layers. The matrix is composed by acicular biotite and of a not resolvable matrix, probably of plagioclase and K-feldspar plagues (not visible in Figure 7f; fir details, see Di Toro and Pennacchioni 2004).

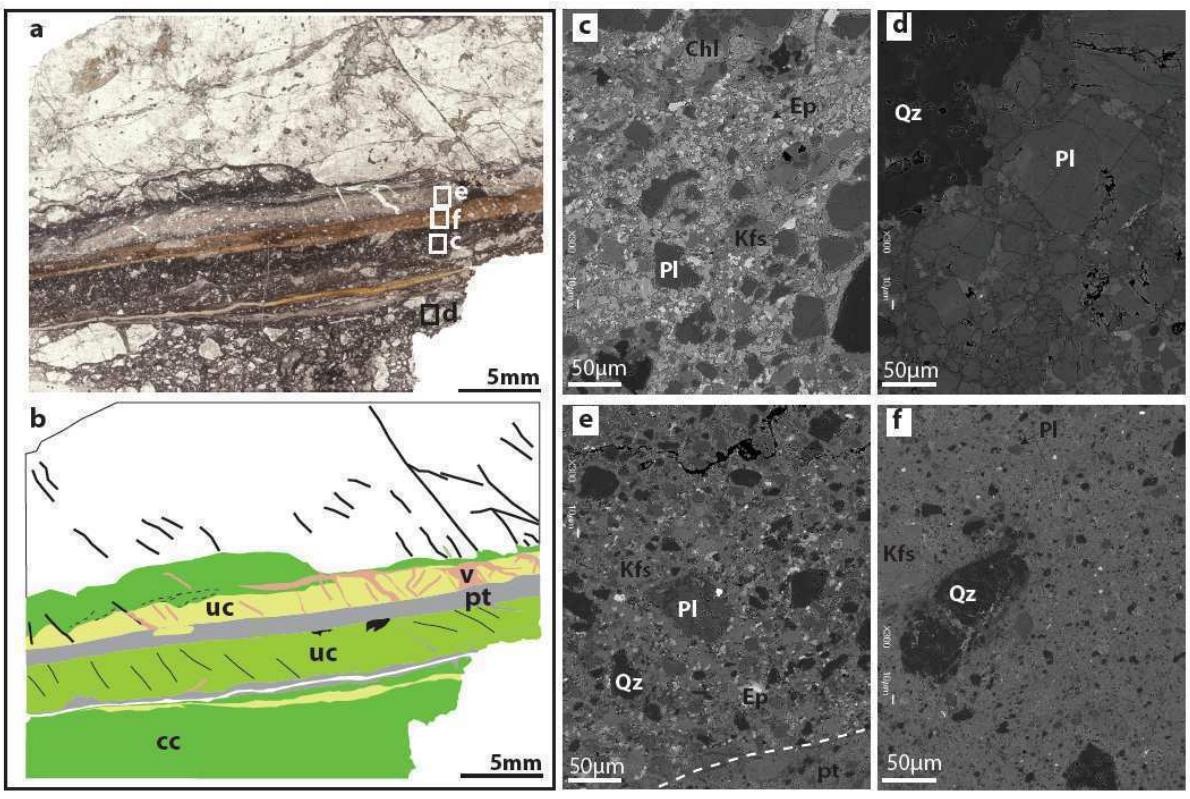

FIGURE 7: The main faults, which accommodated displacements of several meters, have several microstructural domains. (a) Thin section scan and (b) sketch highlighting the structure of a fault (sample 75-2008) with 4796mm of displacement (cc: cataclasite, uc: ultracataclasite, v: veins of K-feldspar and chlorite, pt: pseudotachylyte). (c) Ultracataclasite, composed of large, pervasively fractured, clasts of the host tonalite (SEM BSE image). (d) Cataclasite, composed of clasts of plagioclase and quartz (plagioclase>quartz) in a matrix of epidote, chlorite and K-feldspar (SEM BSE image). (e) Ultracataclasite composed of angular clasts of plagioclase and quartz in a matrix of dominant K-feldspar (SEM BSE image). (f) Pseudotachylyte, with rounded quartz and plagioclase clasts (quartz>plagioclase) in a cryptocrystalline matrix (SEM BSE image).

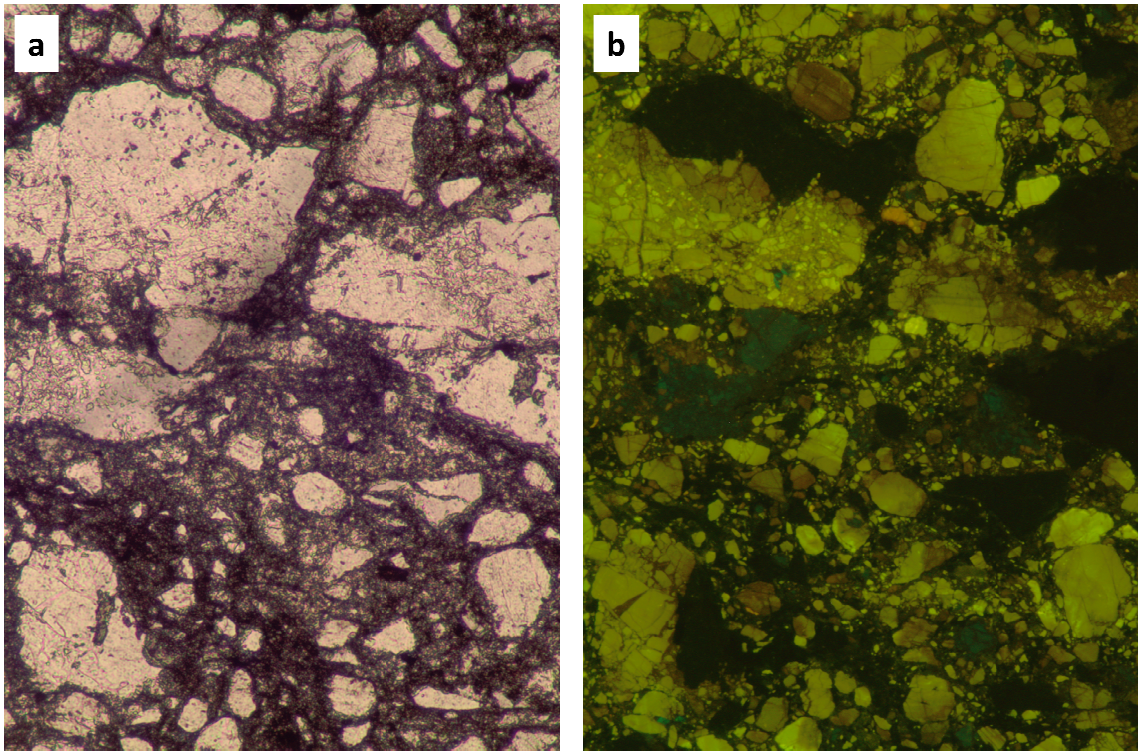

FIGURE 8. Strongly fractured clasts in the cataclasites close to the wall rocks of sample 75, with displacement = 4796 mm? (optical microscope, cathodoluminescence image of the same area). Yellow, plagioclase, blue K-feldspar. The damaged plagioclase has a reddish luminescence.

Protocataclasites enclosed between two fault strands or in restraining bends, own a S-C' foliation Figure 9a). The S foliated material is composed of pervasively fractured plagioclase and quartz, alternated with deformed biotite grains (Figure 9b-c), which are dragged in C' shears (Passchier and Trouw, 2005). At higher magnification, plagioclase and quartz in S domains appear to be fragmented down to sub-micron grain size (Figure 9d, e). Micrometric quartz aggregates have

polygonal, inequigranular (sizes spanning from 1µm to 20µm) grains; fluid inclusions are trapped in grain boundaries (Figure 9d). Plagioclase aggregates are instead composed of inequigranular fragments, with stylolitic grain boundaries (Figure 9e).

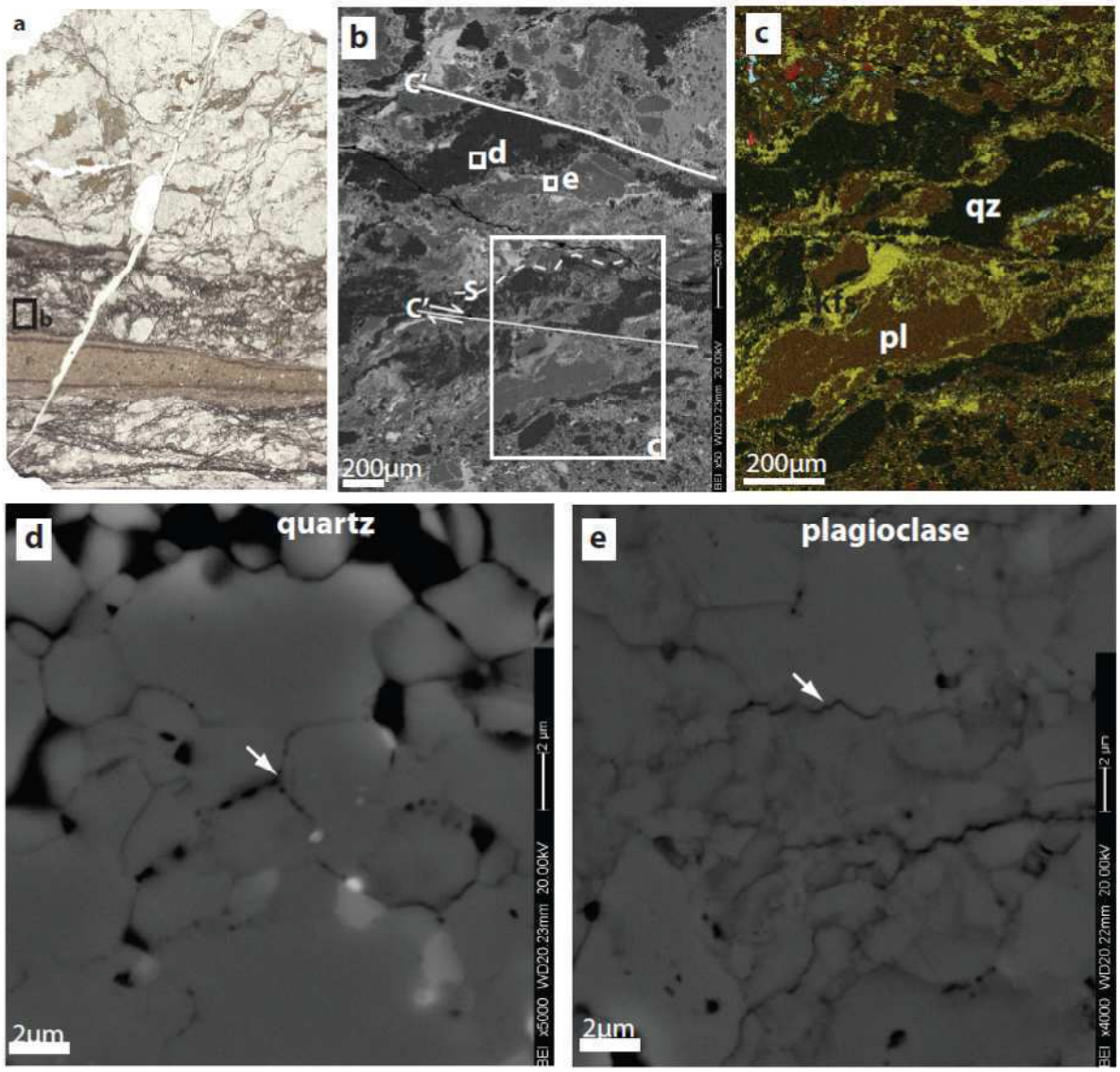

FIGURE 9: Foliated protocataclasite in a main fault (sample S4A-2008) with a cumulative displacement of 1500mm, from a contractional jog. (a) Thin section scan showing the structure of the fault zone, composed by a thick pseudotachylyte layer cutting across a foliated protocataclasite. (b) SEM_EBS image of a S-C' foliated domain, with the location of the images (d) and (e). (c) Combination of SEM EDS maps of Ca (red), K (yellow) and Ti (light blue), so that plagioclase is orange, quartz black, K-feldspar yellow, epidote red and titanite light blue. Quartz, K-feldspar and plagioclase particles are dragged in the C' shear band. (d) Particular of a quartz plague, which is composed of micrometric fragments. Straight grain boundaries and traces of fluid inclusions along the grain boundaries (arrow) suggest quartz recrystallization in presence of fluids. (e) Particular of a

plagioclase plague, composed of micrometric fragments. Indentation of grains suggests that pressure solution processes were active after fragmentation.

3.7. Geochemistry and mineralogy

The Avio tonalite at the base of Lobbia Glacier is 1-5 mm in grain size, composed of 48% An_{45} plagioclase, 29% quartz, 17% biotite and 6% K-feldspar, with accessory titanite, apatite and allanite (Di Toro and Pennacchioni, 2004). The cataclasites reported here are instead composed of K-feldspar (18.1 – 42.41%), epidote (3.41 - 43.3%) , chlorite (5.65 – 27%), plagioclase (3.42 – 30.18%), quartz (0.9 – 21.75%) and titanite (0 – 2.26) (modal compositions estimated by point counting, see section 3.3.3). The relative abundances of the minerals change significantly among the different samples and even among different microstructural domains (cataclasites vs. non-foliated ultracataclasites) within the same sample (Figure 10a).

The modal content of the cement minerals (K-feldspar, epidote and chlorite) was compared with the relative abundances of quartz and plagioclase, which are considered as formed only by crushing of tonalite. Cataclasites show different ratios between plagioclase and quartz (Figure 10b), suggesting that a loss of either mineral occurred in the cataclasites. The relative abundance of quartz with respect to plagioclase is roughly correlated with the composition of the matrix: in chlorite-rich domains, quartz clasts are less abundant than plagioclase clasts, whereas in K-feldspar rich domains quartz clasts are more abundant than plagioclase clasts (compared with the relative abundances in tonalite). This suggests that precipitation of chlorite in the matrix of cataclasites occurred from silica-poor fluids which resulted in quartz dissolution (compare Figure 10b with Figure 10c).

The major X-ray fluorescence elemental bulk compositions of four cataclasites from large displacement faults was compared to the composition of the host tonalite in an isocon diagram (Grant, 1986, 2005) (Figure 11, modified from Pennacchioni et al., 2006). Using the composition of the undeformed tonalite as a reference (straight line in Figure 11), the cataclasites show (i) a strong enrichment in K_2O, loss on ignition and Fe_2O_3, (ii) a slight (within the standard deviation) enrichment in TiO_2, MgO and MnO, (iii) a loss of Na_2O, CaO, SiO_2 (iv) same concentration of Al_2O_3, P_2O_5, FeO. These changes in elemental contents are well justified by the growth of K-feldspar and epidote at the expenses of plagioclase and quartz, as shown by modal mineral compositions.

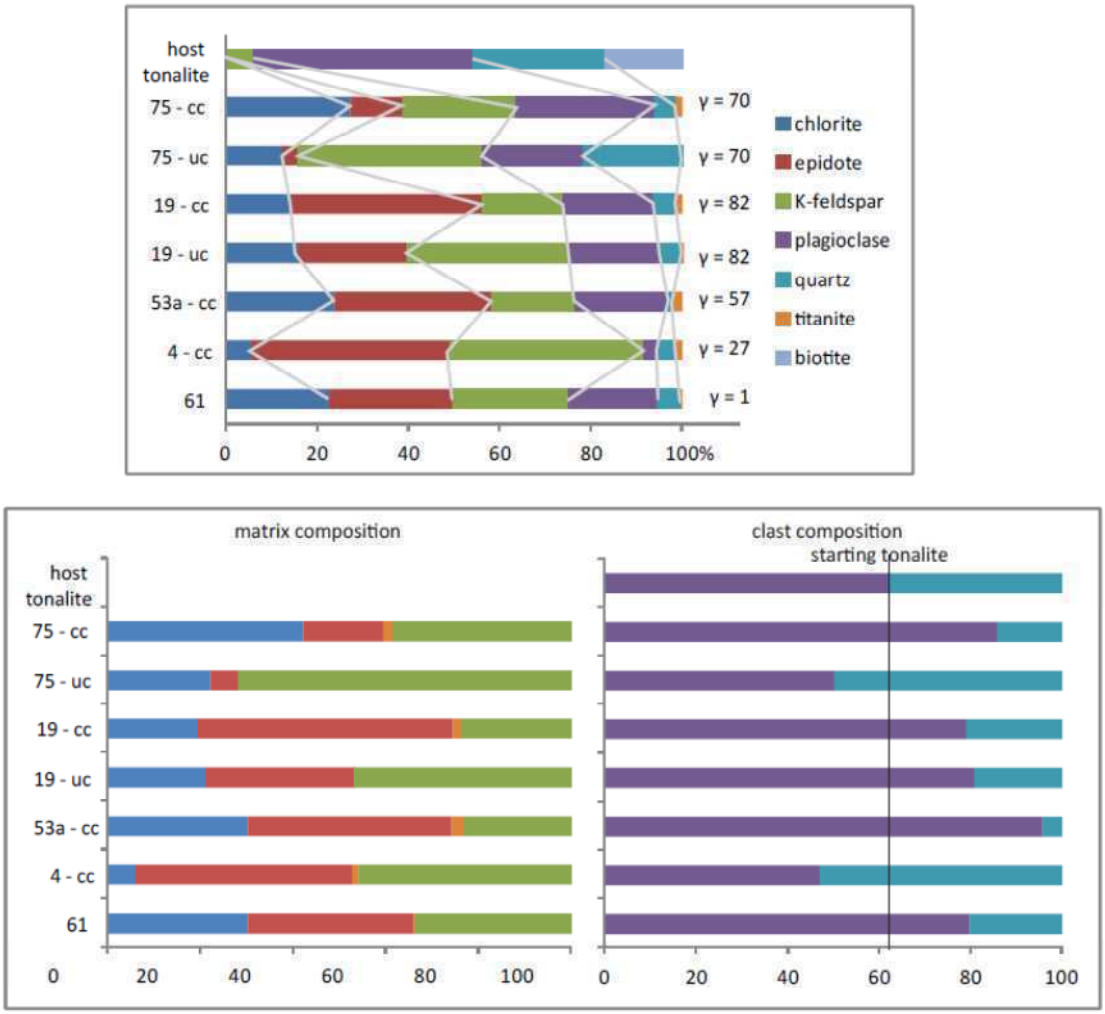

FIGURE 10. Mineral modal content of cataclasites from point counting (see section 3.3 for description of the method) and host tonalite (Di Toro and Pennacchioni, 2004). Cumulated slip in cataclasites increases from bottom to top. (a) Bulk modal content of the cataclasites (b) Modal content of the matrix (left) and of the clasts (right) of the cataclasites.

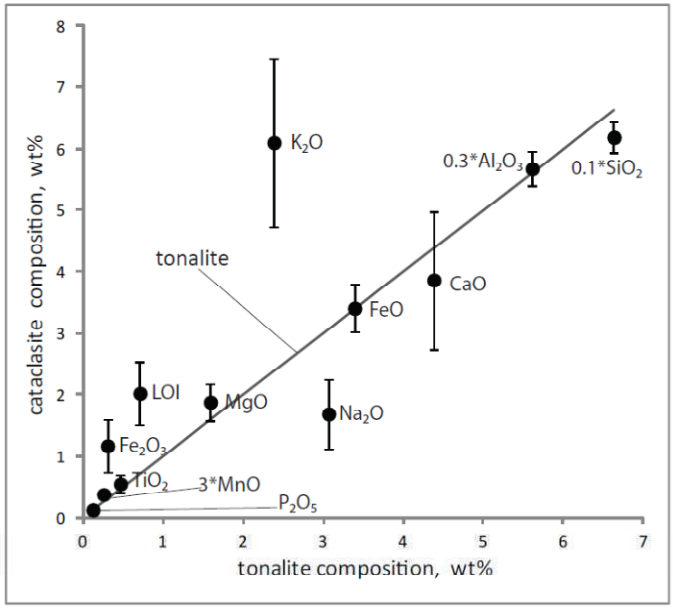

FIGURE 11: Plot of the major elements composition of cataclasite (averaged over four samples, error bars are standard deviations) compared with the composition of tonalite (straight line). Data from X-Ray Fluorescence analyses (Di Toro and Pennacchioni, 2005 and Pennacchioni et al., 2006).

Here we describe the spatial distribution of the minerals in cataclasites, in order to highlight how fluid rock interactions under a driving stress influence the fabric.

In faults with low shear strain, the cement minerals are randomly arranged. Epidote is idiomorphic or poikilitic, often zoned with Fe-rich cores (lighter in SEM BSE images) (Figure 12a, b); chlorite lamellae are randomly distributed and K-feldspar is in plagues. Microfractures in tonalite are sealed by chlorite and K-feldspar (Figure 12a-b).

The foliation in cataclasites with higher finite strain (e.g., γ = 57), is defined by aligned, elongated quartz and plagioclase clasts, K-feldspar plagues and epidote seams. The clasts of plagioclase are fractured along surfaces perpendicular to the S surfaces, and chlorite and, on less extent, K-feldspar fill the fractures (micro-boudins, the strain along the grain in Figure 9d is ε = 1.4), as well as in strain shadows at the tips of plagioclase clasts (Figure 12c-d). These observations suggest that chlorite and K-feldspar grow preferentially in zones of stress shadowing, such as fractures perpendicular to the foliation and around “hard” objects. The undulate boundaries of plagioclase, K-feldspar and quartz clasts along the foliation suggest instead that there is a preferential dissolution of these minerals under the driving stress (the orientation of the foliation and of the tensile cracks is consistent with the dextral sense of shear of these faults, Figure 12c-d).

In ultracataclasite domains, accommodating higher finite strain, the foliation is very weak and the main cement mineral is K-feldspar with blocky texture (Figure 12e, arrow). The plagioclase clasts have albite rich rims (Figure 12f).

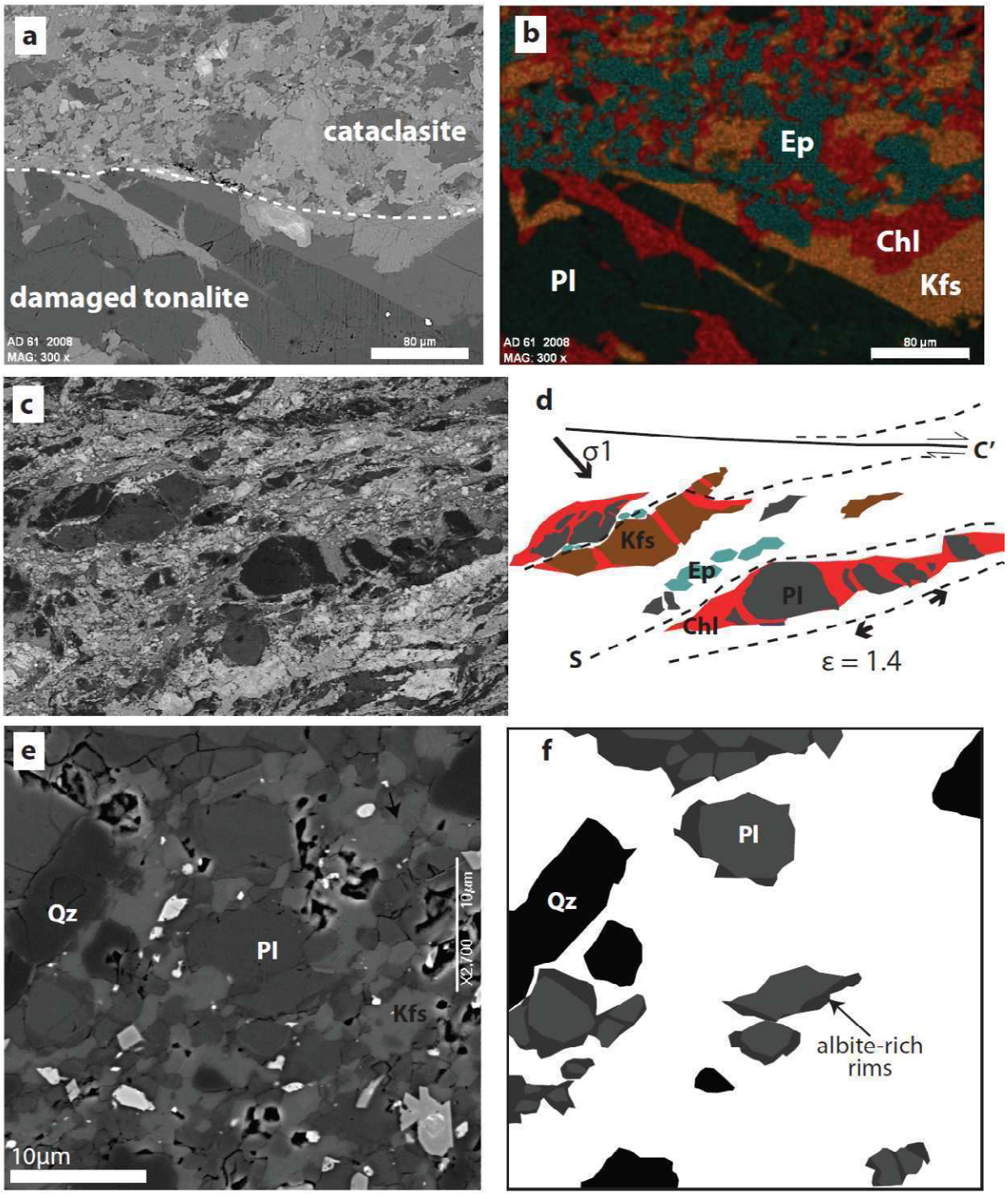

FIGURE 12: Evidence of fluid rock interactions in cataclasites. (a) SEM-BSE image of cataclasite with γ= 1. (b) Same area imaged in Fig. a: combination of SEM – EDS chemical maps (K: yellow, Mg: red, Ca: blue), showing the randomly arranged matrix of epidote, chlorite and K-feldspar cementing the cataclasite. Fractures in the damaged tonalite are sealed by chlorite and K-feldspar. (c) SEM-BSE image of foliated cataclasite. (d) Sketch of image (c) showing the preferential growth of chlorite in pressure shadows (tensile cracks) between plagioclase and K-feldspar boudins. Epidote and titanite crystals are preferentially aligned along the foliation. In this SEM-BSE image the contrast is quite high, so the plagioclase appears black colored. (e) SEM-BSE image of a ultracataclasite cemented by K-feldspar. The foliation is very weak and plagioclase breakdown is suggested by the darker (Na-rich) haloes at the border of the grains. (f) Sketch of image (e) highlighting the occurrence of Na-rich rims in plagioclase.

In the damaged tonalite close to faults, biotite is partially (retrograde) metamorphosed to an assemblage of chlorite + K-feldspar + titanite (Figure 13). Titanite grains are aligned along biotite kink bands and grain boundaries (Figure 13a), defining anastomosed surfaces. Titanite seams in biotite mapped over the whole sample set have a quite constant orientation (Figure 13b), and trace the orientation of the shortening direction (Boullier et al., 2004). The microcracks around altered biotite are sealed by chlorite and K-feldspar, which grow preferentially in 'protected' sites.

Summarizing, the modes of fluid rock interactions in cataclasites which have been recognized in the analyzed samples are: (i) bulk change of chemical and mineralogical composition, with dissolution of either quartz or plagioclase depending on the mineralogy of the matrix; (ii) stress driven dissolution of quartz and plagioclase along the foliation surfaces; (iii) precipitation of chlorite and K-feldspar in protected domains (strain shadows and tensile fractures perpendicular to the foliation surfaces); (iv) retrograde metamorphism of biotite, with distribution of the reaction products controlled by stress orientation..

FIGURE 13 (next page): Evidence of fluid-rock interactions in damaged tonalite. (a) Biotite grains in the host tonalite break down to chlorite + titanite + K-feldspar. Titanite grains inside biotite are aligned. Their alignment forms an angle of about 30° anti-clockwise with respect to the fault. (b) Titanite seams in biotite measured over nine samples collected in the outcrop have a quite constant orientation (with a peak at 30° anti-clockwise with respect to the fault). Tensile cracks filled by chlorite and departing from the biotite grains are oriented at about 90° from the titanite seams. The orientation of the tensile cracks and of the titanite seams is consistent with the inferred far field main principal stress of the area for dextral shearing of the studied main and minor faults. (c) and (d) SEM-BSE images of a biotite grain partially altered. In the sketch, red is chlorite, yellow K-feldspar and light blue titanite.

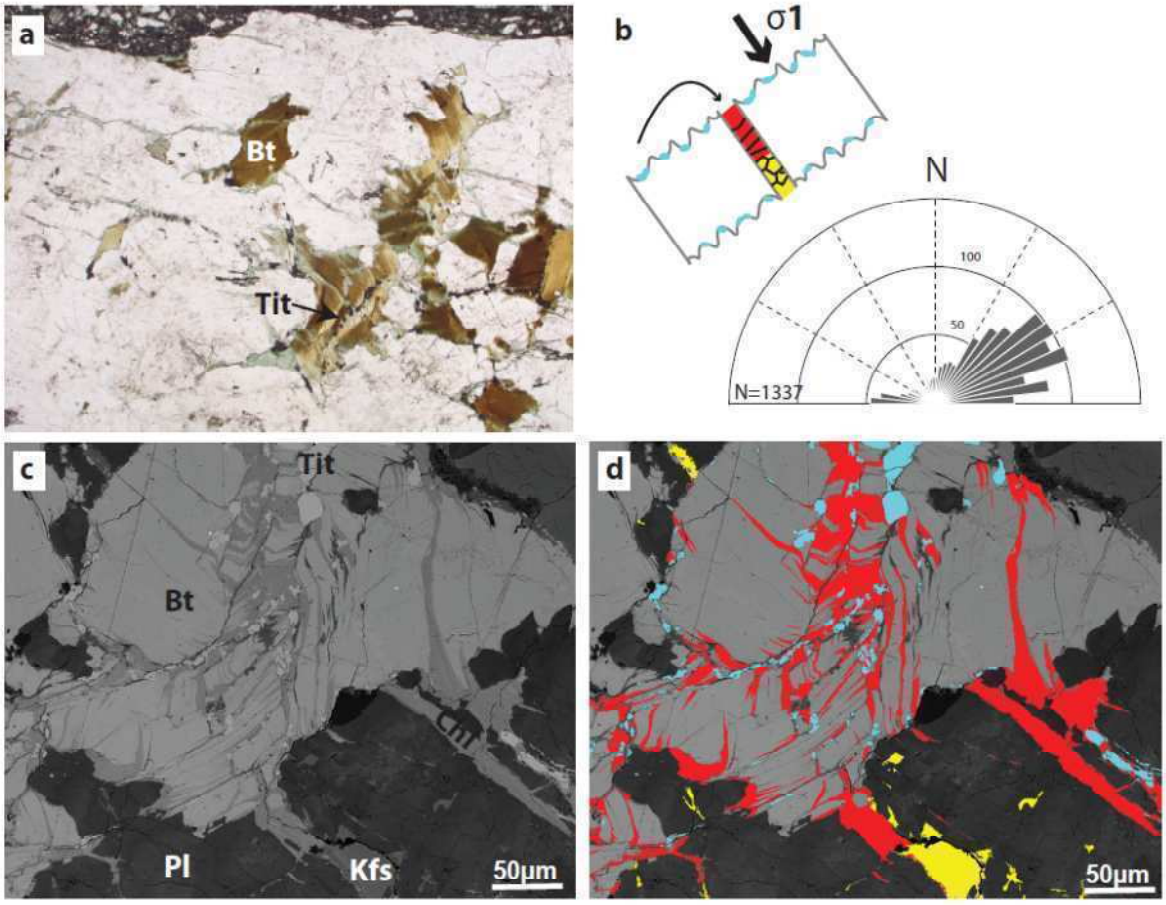

3.8 Image analysis results

3.8.1 Clast size distribution

The CSD measured in images at 400x magnification shows that in low strain cataclasites, the clast fraction with equivalent circular diameter < 6µm is under-represented (Figure 14a), i.e., in the log-log plot, the cumulative distribution curve is less steep for small d_{eq} than for the larger clast fraction. Scanning Electron Microscope images collected at greater magnifications (1000x, resolution 0.1 µm) confirm that micron-size particles are few compared to larger grains (Figure 14b). A lower limit of 6µm is thus imposed for calculating the slope *D* in the log-log diagrams, in order to have a comparable set of data among samples with different grain sizes. The utilization of power laws distributions as we do here is restricted to the purposes of internal comparisons of the dataset collected in this study or in other studies performed on similar grain size ranges (see discussion in Di Toro and Pennacchioni, 2005). In fact, a rigorous application of power law distributions should cover

several orders of magnitude in grain size (Turcotte, 1997). The exponent *D* (called 'fractal dimension' if the distribution covers several orders of magnitude in size, e.g., Turcotte 1997) was calculated as the slope of best fit of the cumulative distributions in *log(number) – log(d_{eq})* space. The upper limit of the distribution was chosen to cover the linear part of the distribution curve in a log-log plot, i.e., when the linear fit was attained with $R^2 > 0.9900$ (Figure 14a). Also the under-represented coarse grain fraction is excluded in the determination of *D*. The values of *D* and the relative "fractal" range are listed in Table 2. The slope *D* was calculated for quartz and plagioclase, where the number of clasts was sufficient to have a good linear fit (N>100). Mosaics of SEM BSE images were used to measure the entire cataclasite layer and the different microstructural domains described in section 6.

In most samples, the 2-dimensional *D* of plagioclase is higher than the *D* of quartz. With increasing finite strain, the slope of the CSD of quartz in whole cataclasite layers increases from D_{qz} = 1.41 to D_{qz} = 2.05, while plagioclase has an almost constant, ranging between D_{pl} = 1.75 and D_{pl} = 1.82 (*D* in this study is from 2-dimensional distributions). If the distributions of the different microstructural domains (cataclasites, foliated cataclasites, etc.) are plotted separately versus finite strain, higher *D* are measured in ultracataclastic domains (D_{qz} = 2.17 and D_{pl} = 2.78). Cataclasite domains have instead $0.87 < D_{qz} < 1.15$ and $1.45 < D_{pl} < 1.53$.

TABLE 2. Results of grain-size analysis.

Sample	γ	Magnification	Mineral	Domain	Number	Mean	Mode	D	R^2	range
61-2008	1	100x	plagioclase	whole	2757	10.81	3.64	1.75	0.9903	6 - 58.96
	1	100x	quartz	whole	311	11.75	3.71	1.41	0.9901	6 - 33.64
	1	400x	plagioclase	whole	591	15.00	2.19	1.44	0.9931	7.84-35.87
	1	400x	quartz	whole	96	21.06	10.82	0.97	0.9916	7.09 -33.57
4 _ 2008	27	100x	plagioclase	whole	241	46.07	13.00	1.20	0.9915	17.99 - 66.02
	27	100x	quartz	whole	351	9.11	3.64	1.54	0.9916	6 - 23.71
	27	100x	quartz	whole	689	8.80	3.64	1.24	0.9936	6 - 44.25
S1A	28	100x	plagioclase	whole	593	12.39	3.78	1.35	0.9905	6 - 22.15
	28	100x	quartz	whole	428	17.71	3.92	0.93	0.9916	6 - 23.24
53a-2008	57	100x	plagioclase	cataclasite	770	11.59	4.31	1.45	0.999	6 - 45.84
	57	100x	quartz	cataclasite	149	12.12	5.78	1.09	0.9935	6 - 18.44
	57	100x	plagioclase	cataclasite	1650	10.74	3.78	1.52	0.9984	6 - 38.89
	57	100x	quartz	cataclasite	360	13.46	3.64	1.15	0.9902	6 - 26.99
	57	100x	plagioclase	whole	3783	10.31	4.24	1.81	0.9965	6 - 69.04
	57	100x	quartz	whole	370	9.95	4.12	1.60	0.9978	6 - 28.61
	57	400x	plagioclase	whole	657	7.84	3.09	1.53	0.9957	6 - 31.48
19	82	100x	plagioclase	whole 1	265	7.04	3.71	1.67	0.9959	6 - 10.79
	82	100x	plagioclase	whole 2	645	13.07	5.97	1.82	0.9983	6 - 17.63
	82	100x	plagioclase	whole 3	793	8.65	3.92	1.55	0.9991	6 - 27.06
	82	100x	quartz	whole 123	217	6.80	3.78	1.49	0.9894	6 - 11.21
	82	400x	plagioclase	ultracataclasite	1347	2.80	1.57	1.98	0.9953	2.12 - 8.
	82	400x	quartz	ultracataclasite	165	4.73	1.35	2.55	0.9933	6 - 9.49
75-2008	70	100x	plagioclase	ultracataclasite	1260	6.58	3.85	2.78	0.9981	6 - 19.95
	70	100x	quartz	ultracataclasite	853	8.81	3.78	1.79	0.9954	6 - 31.52
	70	300x	plagioclase	ultracataclasite	2650	3.99	1.88	2.10	0.9952	6 - 10.91
	70	300x	quartz	ultracataclasite	898	5.95	1.81	2.03	0.99	6 - 27.66
	70	300x	plagioclase	cataclasite	1755	5.68	1.88	1.53	0.9937	6 --31
	70	300x	quartz	cataclasite	123	8.70	1.78	0.87	0.9949	2.69 - 9.29
	70	300x	plagioclase	pseudotchylyte	1106	3.20	1.81	2.20	0.9978	1.84 - 6.75
	70	300x	quartz	pseudotachylite	977	4.10	2.07	2.17	0.9945	6 - 13.16
	70	300x	plagioclase	ultracataclasite	1083	3.67	1.81	2.59	0.9924	6 - 9.87
	70	300x	quartz	ultracataclasite	1118	4.56	1.88	1.82	0.9947	3.29 - 10.38

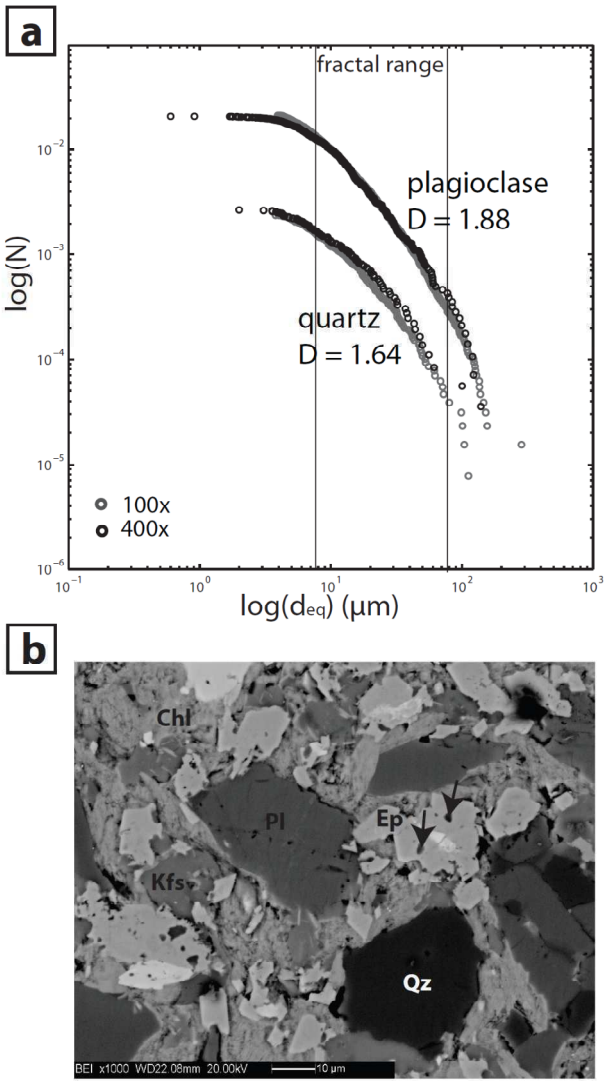

FIGURE 14. Clast size distribution and microstructure in low strain fault. (a) 2-dimensional CSD of sample 61-2008 (γ=1), from a combination of image analysis collected at 100x and 400x. The cumulative number of clasts is normalized by the area of the image. Data of quartz at 400x are quite scattered due to the very low number of clasts present in the analyzed image. (b) Scanning Electron Microscope BSE image of the cataclasite of sample 61-2008 at 100x magnification.

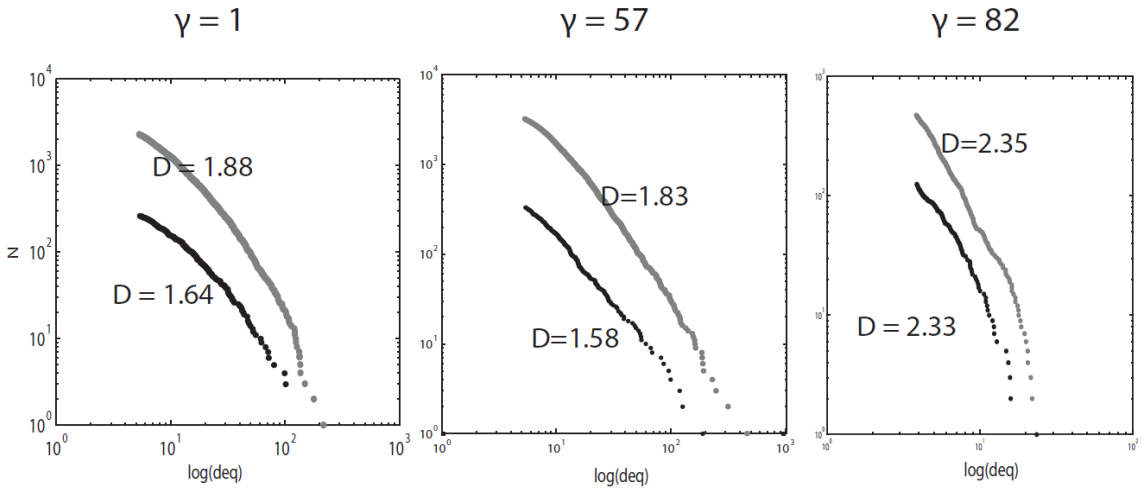

FIGURE 15. Clast size distributions of cataclasites for increasing finite strains from analysis of images collected at 100x. (a) CSD of sample 61-2008 (γ=1). (b) CSD of sample 53a-2008 (γ=57). (c) CSD of sample 19-2008 (γ=82). Black dots = quartz; gray dots = plagioclase.

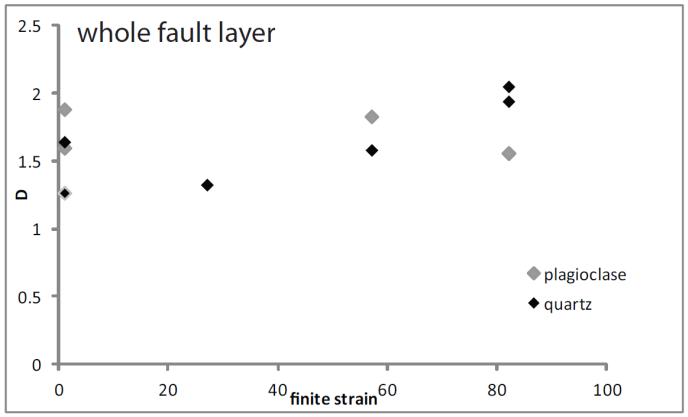

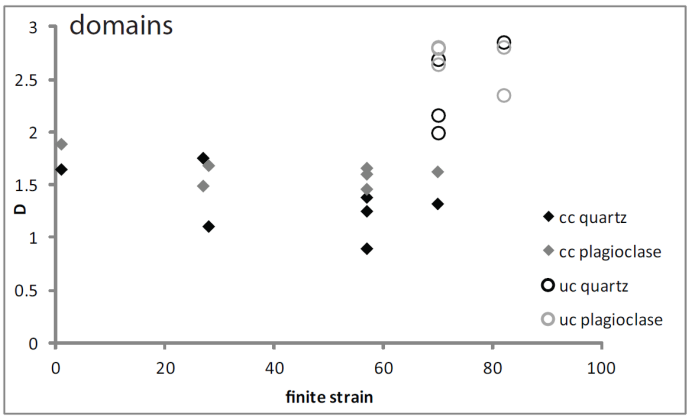

FIGURE 16. The evolution of *D* with finite strain, data collected in images at 100x magnification. (a) The evolution of *D* for data collected over the entire fault (including different domains). (b) The evolution of *D* for data collected in cataclasite (foliated) domains and ultracataclasite domains.

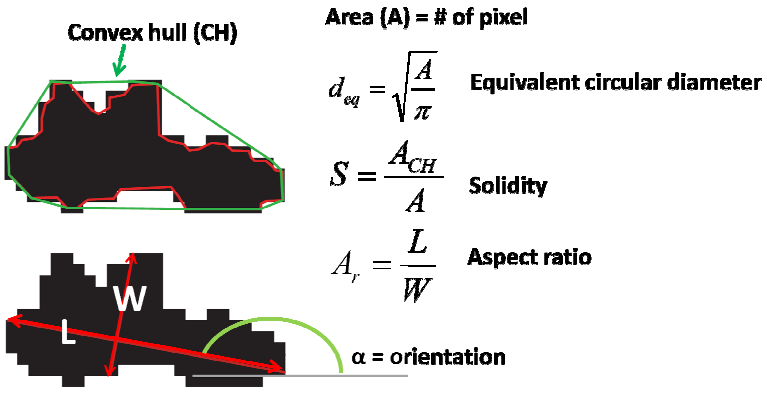

FIGURE 17. Sketch of the parameters measured by image analysis: particle area, equivalent circular diameter, solidity, aspect ratio and orientation are defined in the figure.

3.8.2 Clast shape analysis

The parameters used for describing the shape evolution of plagioclase and quartz grains are defined in Figure 17. The shape parameters (aspect ratio, solidity, etc,) reported in Figure 18 were chosen among the several determined because they were the more useful in highlighting differences in the cataclasite fabric and more sensitive to the change in finite strain.

The plagioclase and quartz clasts in cataclasites have the long axis orientated preferentially at 15 – 35° and 160° to the fault walls (Figure 18a-b), whereas in the ultracataclasites clasts are more randomly oriented (Figure 18c). The preferred orientation measured in the cataclasites (i) corresponds to clast alignment parallel to the S foliation and (ii) is more intense for clasts having larger diameter and aspect ratio, independently of their composition (Figure 17 d-i).

The aspect ratio of particles is computed as the ratio between the longest particle chord (L) and the longest chord perpendicular to L (W). The aspect ratios of clasts in cataclasites are distributed over larger values than in the ultracataclasite domain (Figure 19).

The aspect ratio of particles is computed as the ratio between the longest particle chord (L) and the longest chord perpendicular to L (W). The aspect ratios of clasts in cataclasites are distributed over larger values than in the ultracataclasite domain (Figure 19).

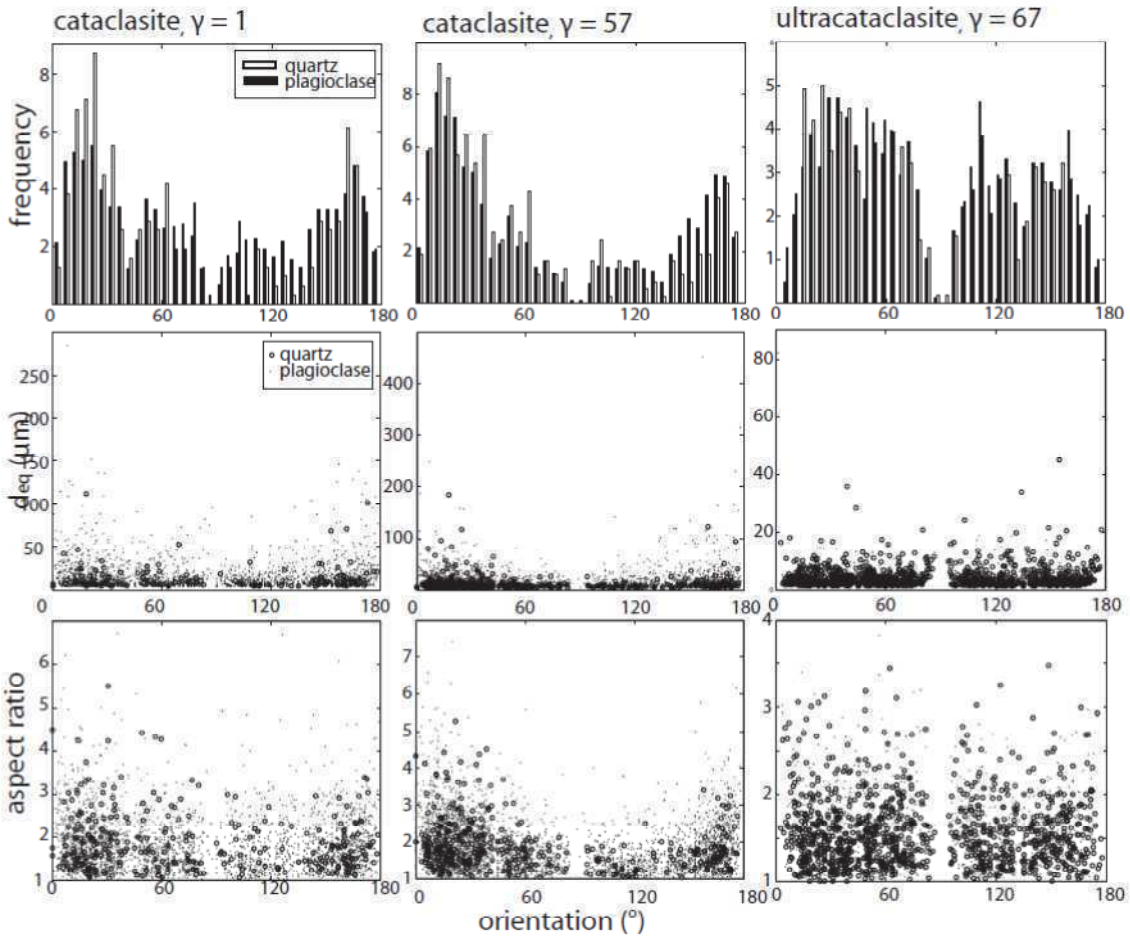

FIGURE 18: Orientation data of quartz and feldspar clasts in samples 61-2008 (γ = 1), 53a-2008 (γ = 57) and 19-2008 (γ = 82). (a) Frequency histograms of the orientation of quartz and plagioclase grains. (b) Mean diameter versus orientation of the long axis. (c) Clast aspect ratio vs. orientation of the long axis.

The solidity is a measure of the smoothness of the particle outlines. A convex object has solidity = 1, lower values indicate the occurrence of embayments or irregular shapes. The histograms of solidity of three representative samples are represented in Figure 19, for quartz and plagioclase. In sample 61-2008, with γ = 1, the maximum solidity of plagioclase and quartz are coincident, in the sample 53a-2008 with γ = 57 the peak of plagioclase clasts is centered on values higher than for quartz. In the ultracataclasite sample 19-2008 with the higher shear strain (γ = 82), the quartz has a peak on higher values of solidity. These observations are in agreement with microstructural observations and the modal content of plagioclase and quartz in these fault rocks, and possibly

related to the preferential chemical alteration (dissolution) of quartz in foliated cataclasite, and of plagioclase in ultracataclasites.

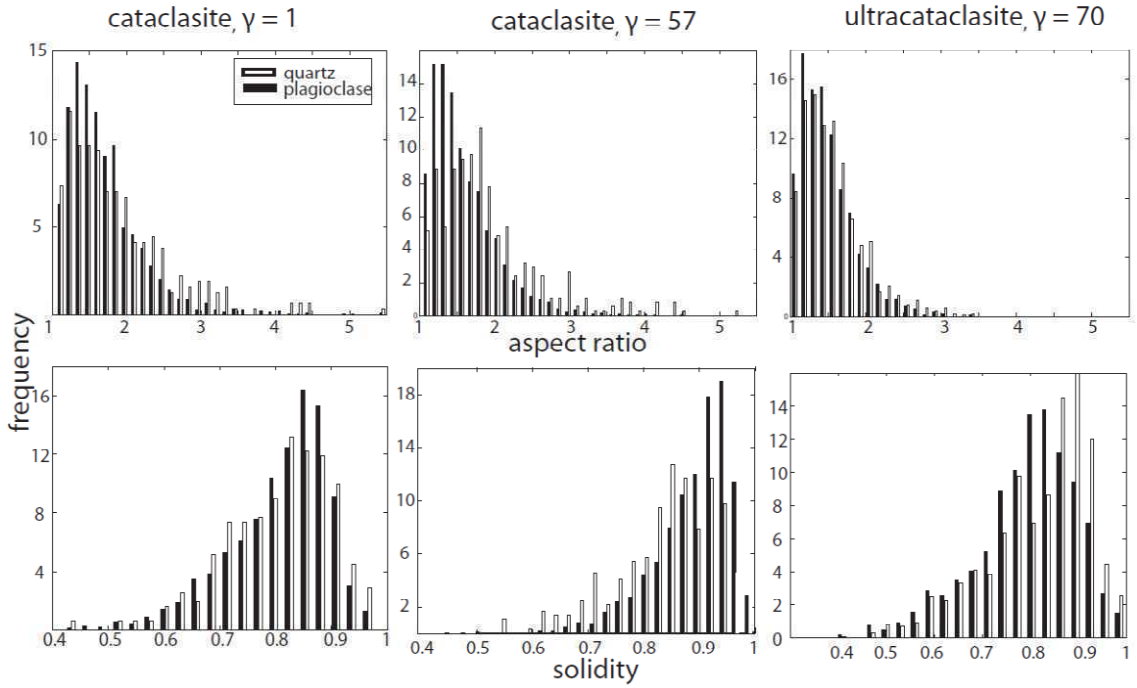

FIGURE 19. Histograms reporting the aspect ratio (top) and solidity (bottom) of quartz and plagioclase clasts measured in samples 61-2008, 53a-2008 and 19-2008 (same samples as in figure 18).

3.9 Discussion

3.9.1 Physico-chemical processes operating in the studied faults

The minor fault samples for microstructural analysis were mostly stem along Riedel-type shear fractures cutting large tonalite lithons comprised between the main faults. Therefore the minor faults are linked to the sliding along the main faults, and accommodate the deformation inside the lithons between two adjacent main faults (Di Toro and Pennacchioni, 2005; Bistacchi et al., 2011). The samples from faults with displacements >1m were collected along main faults, which exploit pre-existing joints and can be followed for tens of meters (Di Toro and Pennacchioni, 2005). Riedel fractures are oriented in a way such that they cannot easily accommodate a large displacement (e.g., Mandl, 1988), which is instead accumulated on the main bounding faults in the selected

outcrop. The different origin and geometry of Riedel shear fractures and main faults influence their fault rock fabric.

The minor faults cutting blocks of tonalite between the main faults preserve the early stages of formation and deformation of the fault material upon fracture propagation. The microfractures in tonalite adjacent to the minor faults (Figure 6), are organized in two sets: (i) at low (0 to 20°) angle to the fault surface, preferentially developed on the southern side, and (ii) at high (30° - 90°) angle to the fault, preferentially developed on the northern side of the shear fracture. One sample (53a-2008), shows just one set of microfractures at 30° to the fault surface on both sides, parallel to the inferred orientation of the main horizontal stress, as reproduced in shear fractures produced in laboratory triaxial texts (e.g., Amitrano and Schmittbuhl, 2002). The more asymmetric pattern in the other samples might arise from local stress rotations due to the propagation of mode II fractures (Vermilye and Scholz, 1998; 1999) or due local waviness of the fault surface, as measured and modeled by Griffith et al. (2010). The microfractures in tonalite are sealed by hydrothermal mineral similar to those cementing cataclasites, and biotite is partially altered to chlorite + K-feldspar + titanite (Figure 13). The biotite dissolution seams lined by titanite are preferentially perpendicular to the inferred main far field principal stress acting on the fault zone (i.e., the Gole Larghe Fault Zone is dextral., Di Toro and Pennacchioni, 2005). This pattern is consistent by pressure driven chemical reactions, favored by fluid infiltration in the host rock through pervasive microfracturing. The sealing of microcracks was thus associated with pressure solution processes and the development of a weak foliation in the damaged tonalite close to faults.

The shear fracture which did not experience a macroscopic shear strain (sample 61-2008) preserves the early stage of the fault filling. Many clasts have the long axis preferentially oriented sub-parallel to the fault boundaries (Fig. 18) and most tensile fractures in the host tonalite are oriented at xxx clockwise to the fault boundaries (Fig. 6x??). As observed in triaxial experiments conducted at confining stress up to 80 MPa on similar rocks (granite, Amitrano and Schmittbuhl, 2002), the tensile microcracks produced during fracture propagation release material from the intact wall rocks (like what is observed in Figure 5a), which is incorporated in the fault with increasing slip. This process is likely to produce preferentially lozenge shaped, fragments with high aspect ratio, as observed in sample 61-2008 (Figure 5a, Figure 19). Moreover, in the studied faults the grabbing of clasts from the fault walls is enhanced by growth of hydrothermal minerals (mostly chlorite and K-feldspar, Figure 12b) in the fractures.

The power law exponent of the CSD, *D*, is an expression of the proportion of small particles over large particles, within a given grain size range. Large *D* correspond to a high proportion of small particles. We assume that the initial size distribution in cataclasites is the one measured in sample 61-2008, which do not show a macroscopic finite strain. The power exponent *D* over the size range 6 – 83.86 μm is 1.75 for plagioclase and 1.42 for quartz. Although the displacement along the fracture is not visible on the outcrop, small particles of plagioclase were produced. These values are quite high for an extensional fracture, which should have $D \approx 1$ (e.g., Blenkinsop, 1991), and the fracture probably experienced some shear.

The accommodation of further strain on minor faults results in (i) thickening of the fault zone due to the production of new material from wearing of the fault walls (e.g., Scholz, 2002), (ii) an evolution in clast size distribution and (ii) the development of multiple textural domains. An overall increase in thickness with displacement is measured for minor faults with displacement < 500mm. The fault thickness was measured in thin section and was averaged over less than 20mm of fault length along strike, so it cannot account for variations in thickness on a larger scale. In the studied area, fault thickness is indeed expected to vary along the fault length due to variations in fault roughness (Bistacchi et al., 2011). The effects of finite shear strain on the *D* of the whole cataclasite (including all the domains and both quartz and plagioclase clasts) results in an increase of the 2-dimensional *D* from values below 1.8 in low strain faults, to values higher than 2. This evolution is associated with the development of multiple domains in cataclasites, including ultracataclasite domains which have $D>2.5$. An increase of the *D* of fault gouge with increasing displacement has been found in other natural fault gouges formed at shallower crustal levels (e.g., Sammis et al., 1987; Blenkinsop, 1991; An and Sammis, 1994; Storti et al., 2003; Billi, 2005; Keulen et al., 2007) and reproduced in shear experiments on simulated gouge (Marone and Scholz, 1989; Biegel et al., 1989;). In several samples, the slope of plagioclase distribution in the log-log *N* vs. d_{eq} plots (Figure 14, 15) is steeper than that of quartz, suggesting that there are proportionally more small particles of plagioclase than of quartz. This can be interpreted as (i) due to the preferential dissolution of small particles of quartz in many of the examined cataclasites (see next point of the discussion), or (ii) due to the lower resistance to fracturing of plagioclase than quartz. Plagioclase has a pervasive cleavage, and such weak planes might facilitate fragmentation.

The samples of cataclasites which show a strongly comminuted layer of ultracataclasite are usually thinner then cataclasites which do not bear ultracataclasites (Figure 3); this observation suggests that strain localization is very efficient in ultracataclasite-bearing faults. It is noteworthy

that ultracataclasite fill fractures oriented at high angle with respect to the faults (Figure 5c). These intrusive features could be interpreted as injection of fluidized material into the wall rocks (e.g., Lin 1996). The intrusive habit of the fractures bordering the minor faults and the extreme localization measured in minor faults hosting ultracataclasites suggest that these fault rocks might be associated to slip instabilities and coseismic slip. The ultracataclasites do not bear evidences of having passed through a melt phase, such as chilled margins, growth of high temperature microlites, spherulites; these features are instead well developed in the associated pseudotachylytes (Di Toro and Pennacchioni, 2004; Chapter 4 of this thesis). The similarity of the CSD of ultracataclasites and pseudotachylytes (Table 2), and their similar structures (injection veins and extreme localization) suggests that the ultracataclasite could be altered pseudotachylytes (so that underwent comminution, melting, solidification and alteration) or coseismic ultracataclasites (that underwent comminution, fluidization and, possibly, alteration, but not melting).

Chlorite- and epidote-rich domains in cataclasites are strongly foliated (Figure 4b, Figure 10) and are less abundant in quartz with respect to plagioclase, at least if compared to the parent tonalite (Figure 10b). The S-C' foliation is defined by the microboudinage of plagioclase clasts; chlorite and K-feldspar fill fractures perpendicular to the foliation and strain shadows. The long axis of plagioclase and quartz clasts is aligned sub-parallel to the S - C' foliation (Figure 18). Dissolution of plagioclase and quartz, and precipitation of chlorite and K-feldspar in fractures are controlled by the driving stress, and contributed to accommodate part of the shear strain. In K-feldspar-rich cataclasites, the plagioclase is lost preferentially. The effect of the matrix composition, which we assume reflects a different composition of the fluid (more under-saturated in SiO_2 in the case of chlorite-rich matrix) is recorded by the clast outline geometry: in samples with high chlorite content, the peak solidity of quartz is lower than that of plagioclase, where instead the K-feldspar dominate, the plagioclase has a lower peak solidity.

The main faults, accommodating displacements of more than 1m, have a complex internal layering, with cataclasites with coarser grain size along the wall rocks, passing to ultracataclasites towards the fault cores, and bear pseudotachylytes, which mostly crosscut the cataclasites (Di Toro and Pennacchioni, 2005). The damage in the material within the main faults is more intense than along the minor faults/fractures, as highlighted in Figure 8 and 9, and might be related to the intense stress perturbation associated to the propagation of seismic ruptures along the main faults (e.g., Reches and Dewers, 2005; Pittarello et al., 2008). The wall rock grains are crushed down to sub-micron size fragments and, in the case of quartz, they preserve a foam-like recrystallized

microstructure possibly due to the heat pulse typical of seismic slip (Bestmann et al., 2012; Figure 9d). The sutures inside the highly comminuted plagioclase along main faults (Figure 9e) suggest pressure-solution driven clast indentation, probably enhanced by the extreme fine grain size. An S-C' foliation is developed in this domain (Figure 9b, c).

3.9.2 Implications for the seismic cycle

Experimental work demonstrated that the fabric *latu sensu* of gouge determines its strength, sliding stability and friction coefficient (e.g., Beeler et al., 1996; Biegel et al., 1989; Mair et al., 2002). As observed in natural and experimental gouges, both grain shapes (Storti et al., 2003; Heilbronner and Keulen, 2006; Stunitz et al., 2010) and CSD (e.g., Sammis et al., 1987; Blenkinsop, 1991; An and Sammis, 1994; Storti et al., 2003; Billi, 2005; Keulen et al., 2007) of gouge evolves with displacement, to values of $D>2$ (in two dimensions) and more rounded particles (e.g., Storti et al., 2003). Understanding the evolution of gouge fabric (including its mineralogy) with displacement is thus of great importance for understanding the behavior of faults, i.e., if they will slide aseismically or if they will undergo slip instabilities. The most "evolved" material, i.e., having the highest D, found in the studied samples is localized within the ultracataclasite layers, which are associated with a possible strain weakening behavior (they accommodated more displacement without a large increase in thickness) (Beeler et al., 1996). The cataclasite samples which instead are thicker are composed of coarser, less evolved fault material, foliated, suggesting a strain strengthening behavior.

However, the application of models of grain size evolution developed for granular material (e.g., Sammis et al., 1987; Sammis and King, 2007; Mair and Abe, 2011) on faults which were active at seismogenic depth is not straightforward, because of the intense fluid-rock interactions occurring in natural faults. We measured a trend in grain size evolution with slip and finite strain which is coherent with that measured in other natural faults and in shear experiments, but we documented also the onset of chemical reactions which is coeval to cataclasite formation.

Rock fragmentation and the percolation of reactive fluids cause some of the cataclasites to develop a foliated texture, which is more intense where the matrix mineral assemblage is dominated by chlorite. The effects of chlorite (and phyllosilicates in general) in enhancing pressure-solution processes has been observed in experiments and natural faults (e.g., Renard et al., 1999).

The onset of pressure-solution deformation occurs probably until the cementation of the cataclasites is complete, and they recover their strength.

3.10 Conclusions

One of the aims of this study was the quantitative comparison of the microstructures found in natural faults with increasing displacement with those produced under controlled conditions in the laboratory and described in the literature. In fact, extrapolation to natural conditions of experimental observations (i.e., mechanical data) fails if the artificial fault rock products are dissimilar to natural ones: microstructural differences might result from other physico-chemical processes operating in nature with respect to those triggered in the laboratory. The evolution of the fabric of natural fault rocks with increasing deformation was investigated by means of microstructural and geochemical studies on a set of samples from the seismogenic Gole Larghe fault. The samples experienced displacements from δ = 1 - 4797mm; faults with δ<500mm have been more thoroughly examined and compared with large displacement faults.

The clast size distribution of quartz and plagioclase clasts evolves with increasing shear strain from $D < 1.5$ to $D > 2$, in agreement with previous studies on natural and experimental fault gouges. The aspect ratio of the clasts is higher for low strain faults and decreases with increased shearing. If highly sheared material (ultracataclasite) is present in the slipping zone the deformation is accommodated more efficiently without an increase in thickness (which would correspond to a strain weakening behavior).

Besides mechanical fracturing and comminution processes, the interaction with fluids strongly influences the fabric of natural cataclasites. The most relevant effect is the formation of a foliation and the transfer of dissolved chemical mass in solution, which is an efficient mechanism for accommodating bulk deformation. Chemical aggression on the plagioclase and quartz clasts is evidenced by the low values of some shape descriptors such as solidity and convexity, indicating lobed clast outlines.

According to the natural example investigated here, experiments performed on granular materials that do not include fluid-rock interaction might produce too simple mechanical models of the actual behavior of fault materials at seismogenic depths.

Chapter 4. Origin of hydrous fluids in faults at seismogenic depth: constraints from the hydrogen isotope geochemistry

Abstract

The role of hydrous fluids on the material properties of rocks in crustal faults is critical in controlling the dynamics of the seismic cycle. The presence of a free fluid phase at hypocentral depth has been measured by geophysical methods in many seismically active areas, so that the fluid pressure might potentially equal the lithostatic load. By contrast, abundant veining is not commonly associated with pseudotachylyte bearing fault systems, fault rocks produced by quenching of friction melts.

In this study, we performed microstructural, mineralogical and geochemical characterization, and hydrogen isotope analysis, on fault rocks from the Gole Larghe Fault (Southren Italian Alps), anexhumed seismogenic fault zone in tonalite, which was active at 9 – 11 km depth. Fault products span from early stage, high temperature (T = 550°C) mylonites, to cataclasites and pseudotachylytes (T = 250 – 300°C). Pseudotachylytes were formed by frictional melting of host tonalite and cataclasite, and are compared with frictional melts produced in dry, high velocity (up to 1.2 ms^{-1}) friction experiments simulating seismic slip on samples of tonalite and cataclasites collected in the same fault zone.

The bulk tonalite bears 0.96% of H_2O, the mylonites 1.4 – 1.7 % , the cataclasites 1.3 – 3.2 % and the pseudotachylytes 2.3 – 4.4% of water. The water content in cataclasites is explained by growth of hydrothermal minerals, while the strong enrichment in water in pseudotachylytes is due to (i) growth of biotite during cooling of the frictional melts and (ii) the occurrence of weakly bonded water in de-vitrified domains. The tonalite has hydrogen isotope composition (expressed as D/H ratio normalized on the SMOW) δD = -74 ± 1‰, close to the value in mylonites, having δD =-78 ± 1‰. Cataclasites have δD = -65 ± 4‰ and natural pseudotachylytes have δD of -93±9‰. Experimental pseudotachylytes have δD of -7 5 ± 2‰ (from tonalite) and of -83 ± 1‰ (from cataclasite).

At the scale of the fault zone evolution, the formation of cataclasite bearing faults corresponds to an opening of fluid circulation, with the ingression of fluids with higher δD than the magmatic fluids. Natural pseudotachylytes show a trend (lower δD) opposite than cataclasites, possibly due to the inclusion of adsorbed low D, present day high altitude rain water. This hypothesis is supported by step heating FTIR spectroscopy data. If the present day component of water is subtracted, the δD of the pseudotachylyte is in the range -75 to --80, similar to what obtained in dry friction experiments. We conclude that the main source of hydrous fluids in seismic melts is dehydration of the hydrous minerals in the wall rocks.

(this study was done in collaboration with Luigi Dallai, Giulio Di Toro, Giorgio Pennacchioni)

4.1 Introduction

Fluids are thought to be crucial in controlling the physics of earthquakes and faulting (e.g., Miller et al., 2004; Chiarabba et al., 2009;), but fluid origin and circulation paths at the base of the seismogenic crust are poorly known (for reviews, Abercrombie et al., 2006; Handy et al., 2007). Exhumed seismogenic faults offer the opportunity to investigate the mechanical and chemico-physical processes during the nucleation and propagation of seismic ruptures at the base of the seismogenic crust (7-15 km, Scholz, 2002), and the role of fluids in the seismic cycle. In silicate-bearing rocks, fast (about 1 ms^{-1}) sliding during earthquake propagation may result in melting of the fault rocks due to frictional heating (Jeffreys, 1942; McKenzie and Brune, 1972; Sibson, 1975). The friction melts quench in seconds to minutes (depending on melt thickness and temperature of melt and host rock) forming a dark-colored, glassy rock called pseudotachylyte (after Shand, 1916). Pseudotachylytes often preserve flow structures (e.g., Lin, 1994), microlites and spherulites (Di Toro and Pennacchioni, 2004), vesicles, amygdale (Magloughlin, 1992) and rare glass (for a review, Di Toro et al., 2009; Lin, 2007). Pseudotachylytes are considered evidence of past seismic activity in an exhumed fault (Sibson, 1975; Cowan, 1999) and, if not altered, they potentially retain information on fluid-rock interaction during an earthquake (O'Hara and Sharp, 2001; Moecher and Sharp, 2004). Frictional melting is a process which is commonly assumed to occur under "dry" conditions (Sibson and Toy, 2006, for a review). In fact, (i) coseismic frictional heating would result in thermal expansion of pore fluids which would pressurize the fault impeding the achievement of melting temperatures (Sibson, 1973; Rice, 2006) and (ii) water vaporization adsorbs heat and buffers the

increase in temperature in the slipping zone. On the other hand, the presence of water might lower the melting point of slipping zone minerals and should promote melting Allen (1979). Field evidence exist that pseudotachylytes are spatially and kinematically associated with cataclastic zones and breccias cemented by hydrothermal minerals (e.g., Magloughlin, 1992; Fabbri et al., 2000; Di Toro and Pennacchioni, 2005; Griffith et al., 2008). In particular, some pseudotachylytes hosted in the Sierra Nevada granodiorites (California) were produced in the same rupture event that produced the hydrothermal-mineral rich cataclasites (Kirkpatrick and Shipton, 2009; Griffith et al., 2010). Other pseudotachylytes, such as those from accretionary complexes in Alaska and Japan formed under fluid-present conditions (e.g., Rowe et al., 2005; Ujiie et al., 2007; Meneghini et al., 2010). Lastly, presence of vesicles in some pseudotachylytes requires that a fluid phase was generated during melting and pseudotachylyte formation (Maddock, 1987; Boullier et al., 2001).

Oxygen and hydrogen isotope compositions of silicatic minerals are useful tracers for water-rock interactions in geological processes (Taylor, 1977). The oxygen isotopic ratio in pseudotachylytes is buffered by the oxygen of the silicate minerals undergoing melting and is sensitive to the ingression of an external fluid for high fluid/rock ratios (O'Hara and Sharp, 2001). In contrast, the hydrogen isotopic ratio is more sensitive to the exchange of small amounts of water (Moecher and Sharp, 2004). The occurrence of meteoric water within a fault zones should be readily detected on the basis of the isotope composition of hydrogen. The only available hydrogen isotope data on pseudotachylytes and host gneiss are from the Homestake shear zone (Moecher and Sharp, 2004). The Homestake Shear Zone pseudotachylytes likely formed at 5-7 km depth as constrained by the thickness of overlying sedimentary sequences and are not associated with cataclasites (Allen, 2005). Pseudotachylytes contain white mica as product of devitrification of former glass and their hydrogen isotope compositions indicate that the main source of hydrogen in the melt was the dehydration of hydrous mineral in the host rock, with minor effects of hydrogen fractionation due to crystallization of white mica.

In this work we investigated the origin of hydrous fluids in mylonites, cataclasites and pseudotachylytes from three outcrops of seismogenic fault zones cutting the northern Adamello massif (Southern Italian Alps): the Gole Larghe Fault Zone (Di Toro and Pennacchioni, 2004; 2005) and the Passo Cercen fault (PCF, Mittempergher et al., 2009). After characterizing the mineralogy and the speciation of water in the fault rocks and the tonalitic host rock, hydrogen isotope measurements were performed on bulk rocks and mineral separates. For constraining the mechanisms of isotope fractionation during seismic slip, the products of frictional melting produced

in high velocity friction experiments starting from rock sampled in the same outcrops were analyzed as well.

4.2 Geological setting

The E-W-trending Gole Larghe fault zone cuts across the northern Adamello batholith in the Southern Italian Alps (Fig. 1a). The host rock is tonalite of the Val d'Avio pluton, whose crystallization and cooling ages range from 32 to 34 Ma (Del Moro et al., 1983). Successive deformation phases are recorded along the GLFZ, localized along pre-existing joints (Pennacchioni et al., 2006): amphibolite facies mylonites (T = 550°C), low greenschist facies cataclasites associated with pseudotachylytes (T = 250 – 300°C) and late zeolite bearing faults (T = 150°C). Mylonitic and brittle faulting occurred at 9-11 km depth, before the exhumation of the Adamello batholith (Di Toro and Pennacchioni, 2004). This is constrained by stepwise heating ^{39}Ar - ^{40}Ar (Villa et al., 2000) dating on pseudotachylytes matrix at an average age of about 30 Ma (Pennacchioni et al., 2006), i.e., prior to the exhumation of the area began. The GLFZ was sampled in two locations, as shown in Figure 1.

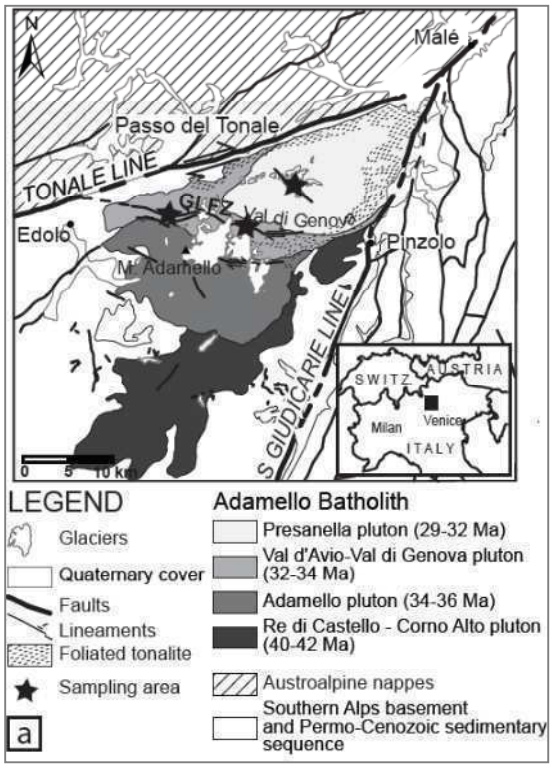

FIGURE 1. Geological setting. (a) Sketch of the Adamello batholith and the Gole Larghe Fault Zone; the sampling localities are indicated by the black stars.

4.3 Methods

The type of analyses performed are summarized in Table 1. Composite samples including different lithologies (tonalite, cataclasite and pseudotachylyte) have been cut to produce subsamples of the individual rock types. Polished thin sections obtained from the samples were analyzed with a scanning electron microscope (SEM, Camscan-Mx2500, resolution in back scattering of 100 nm, Dipartimento di Geoscienze, University of Padova, Italy) and with a Field Emission SEM (FE-SEM, JEOL 7000, resolution in back scattering of 4 nm, Istituto Nazionale di Geofisica e Vulcanologia, Rome, Italy). Both electron microscopes were equipped for energy dispersive spectrometric (EDS) X-ray microanalysis microanalysis. The EDS activation volume was 1 - 2 μm in radius for the SEM and 400 nm in radius for the FE-SEM (Del Gaudio et al., 2009).

X-Ray diffraction (XRD) was performed on representative host and fault rock powdered samples. Powder XRD data were obtained by step scanning using an automated diffractometer system (Philips X'Change) with incident- and diffracted-beam Soller slit (0,04 rad.). Diffraction profiles were obtained using a step interval of 0.02° 2θ with a counting time of 15 s. Scanning was performed over the range 3-70° 2θ. All the samples were ground to a particle size of <10 micron to minimize the possible microabsorption effect and to improve accuracy in measuring the intensities. Powders were loaded in Al sample holders with an area of $2 \times 1.15 cm^2$. The program High Score Plus (Panalytical) was used for the phase identification and the Rietveld refinement.

Fourier Transform infrared (FTIR) spectra were acquired in transmission mode in an HYPERION3000 microscope, equipped with a detector MCT (Mercury Cadmium Telluride) and an FPA (Focal Plane Array) detector, composed of a matrix of 64x64 detector cells, which allowed to cover an area on the sample surface of 170x170 μm. Samples were doubly polished rock slices 50 to 60 μm thick. FTIR were acquired also using an heatable chamber under vacuum (10^{-5} bar), for the following heating steps: 50°C, 100°C, 150°C, 200°C, 300°C. Background correction for the air and the windows of the heating chamber were calibrated before each acquisition.

Electron Microprobe data were obtained with the Cameca SX50 apparatus of the Geosciences Department of Padova University.

Bulk sample	*Rock type*	*Outcrop*	*Analyses*	*Sub-samples*	*Type of sample*	*Analyses*
Natural samples						
20b-00	pt in tonalite and cataclasite	Lobbia	XRF	20b-00-md 20b-00-sd		XRF XRF
07 162	mylonite	Lobbia		07-162-umyl	bulk myl	
99-D7	mylonite	Lobbia		99-D7-umyl	bulk myl	
50-00	cataclasite	Lobbia	XRF			
23-00	cataclasite	Lobbia	XRF			
2-99	pt in tonalite and cataclasite	Lobbia		2-99-bt 2-99-pt	biotite separate pt separate	TC/EA, CHN TC/EA, CHN
21-00	tonalite	Lobbia			biotite separate	TC/EA
3-02	pt in tonalite	Lobbia		3-02-bt 3-02-pt 3-02-pt-c	biotite separate bulk pt bulk pt	TC/EA TC/EA, CHN TC/EA
10-04	pt in tonalite	Lobbia	XRPD, FE-SEM	10-04-pt	bulk pt	TC/EA, CHN
46-99	pt in tonalite and cataclasite	Lobbia	XRF, XRPD, FE-SEM	46-99-cc 46-99-ptm-a 46-99-pt-a 46-99-pt-b 46-99-pt-c 46-99-pt-d	bulk cc bulk pt bulk pt bulk pt bulk pt bulk pt	TC/EA, CHN TC/EA, CHN TC/EA TC/EA TC/EA TC/EA
24-00	pt in tonalite and cataclasite	Lobbia	XRF, FE-SEM	24-00-cc 24-00-pt	bulk cc bulk pt	TC/EA, CHN TC/EA, CHN
32-00	pt in tonalite and cataclasite	Lobbia	XRF, XRPD, FE-SEM	32-00-cc 32-00-pt 32-00-pts	bulk cc bulk pt bulk pt	TC/EA, CHN TC/EA TC/EA, CHN
11-01	pt in tonalite and cataclasite	Lobbia		11-01-cc 11-01-pts	bulk cc bulk pt	TC/EA, CHN TC/EA, CHN
19-01	pt in tonalite and cataclasite	Lobbia		19-01-pt-c 19-01-pt-f	bulk pt bulk pt	TC/EA TC/EA,CHN

17-01	pt in tonalite and cataclasite	Lobbia		17-01-pt	bulk pt	TC/EA, CHN
13-01	pt in tonalite and cataclasite	Lobbia	XRPD, FE-SEM	13-01-pt-a	bulk pt	TC/EA
				13-01-pt-b	bulk pt	TC/EA, CHN
2-01	pt in tonalite and cataclasite	Lobbia		2-01-pt	bulk pt	TC/EA, CHN
21-01	pt in tonalite and cataclasite	Lobbia		21-01-pt-a	bulk pt	TC/EA, CHN
				21-01-pt-b	bulk pt	TC/EA
G 5	tonalite	Avio		G5-bt	biotite separate	TC/EA, CHN
L 65	pt in tonalite e cataclasite	Avio		L-65-pt	bulk pt	TC/EA, CHN
HVFRE samples						
370-06	artificial pt in tonalite		SEM	370-06-pt	bulk pt	TC/EA, CHN
372-06	artificial pt in tonalite		SEM	372-06-pt	bulk pt	TC/EA, CHN
376-06	artificial pt in tonalite		SEM, EMPA	376-06-pt	bulk pt	TC/EA, CHN
371-06	artificial pt in cataclasite		SEM	371-06-pt	bulk pt	TC/EA, CHN
				371-06-cc	bulk cc	TC/EA, CHN
378-06	artificial pt in cataclasite		SEM	378-06-pt	bulk pt	TC/EA, CHN
				378-06-cc	bulk cc	TC/EA, CHN
379-06	artificial pt in cataclasite and tonalite		SEM	379-06-pt	bulk pt	TC/EA, CHN
				379-06-cc	bulk cc	TC/EA, CHN

TABLE 1. List of the studied samples and subsamples. pt: pseudotachylyte, cc: cataclasite, bt: biotite, md: microlitic domain, sd: spherulitic domain, XRF: X-ray fluorescence, XRPD: X-ray powder diffraction, SEM: Scanning Electron Microscope, FE-SEM: Field Emission SEM, EMPA: Electron Micro-Probe Analysis, TC/EA: High Temperature Conversion Elemental Analyzer, CHN: Carbon, Hydrogen Nitrogen analyzer.

Hydrogen isotope ratios were measured on: (i) biotite mineral separates from the host tonalite, (ii) bulk cataclasite, (iii) bulk natural and (iv) bulk artificial pseudotachylyte powders. The samples were analyzed using a High Temperature Conversion Elemental Analyzer (TC/EA) in line with a Thermo-Finnigan Delta XP IRMS, at the IGG-CNR in Pisa, following the method described in Sharp et al. (2001). A standard NBS30 biotite was analyzed every 10 analyses, to correct the apparatus drift; the measured values were corrected for an NBS30 biotite value of δD = -67.5 (USGS, http://www.rcamnl.wr.usgs.gov/isoig/res/guide.html) and reproducibility of the measurements was within ±5‰. Results of these analyses are presented in the standard delta notation as parts per thousand (‰), relative to the SMOW (Standard Mean Ocean Water). The samples analyzed for hydrogen isotope were also measured for their quantitative CHN contents by means of a Fisons CE-EA 1108.

4.4 Petrography and microstructure

4.4.1 Host tonalite

In the Gole Larghe Fault, the host rock is the Val d'Avio tonalite. It is a medium grained rock composed of 48 wt.% plagioclase, 29% quartz, 17% biotite and 6% K-feldspar, with accessory titanite, allanite and apatite (Di Toro and Pennacchioni, 2004) (Fig. 2a). Plagioclase is idiomorphic and shows oscillatory and normal zoning, with anorthite-rich cores. Biotite is idiomorphic and locally defines a foliation, probably magmatic in origin. Quartz and K-feldspar occur as interstitial phases. Close to faults, tonalite is commonly altered with growth of chlorite at the expense of biotite and saussuritization of plagioclase. In both outcrops, the analyzed tonalite samples were collected in unaltered rock volumes between fault horizons.

4.4.2 Mylonites, cataclasites and pseudotachylytes of the GLFZ

The mylonitic deformation in this area is localized along pre-existing joints (for an thorough description, Pennacchioni, 2005). Various grades of deformation affect the tonalite close to shear zones, from a S-C' fabric to an intense mylonitic foliation. The two samples of mylonite analyzed in this study are from foliated domains, where: quartz is dynamically recrystallized, plagioclase form

rounded porphyroclasts, K-feldspar is preserved in pressure shadows and biotite is present as mica fish (relict grains from the tonalite) or as recrystallized aggregates.

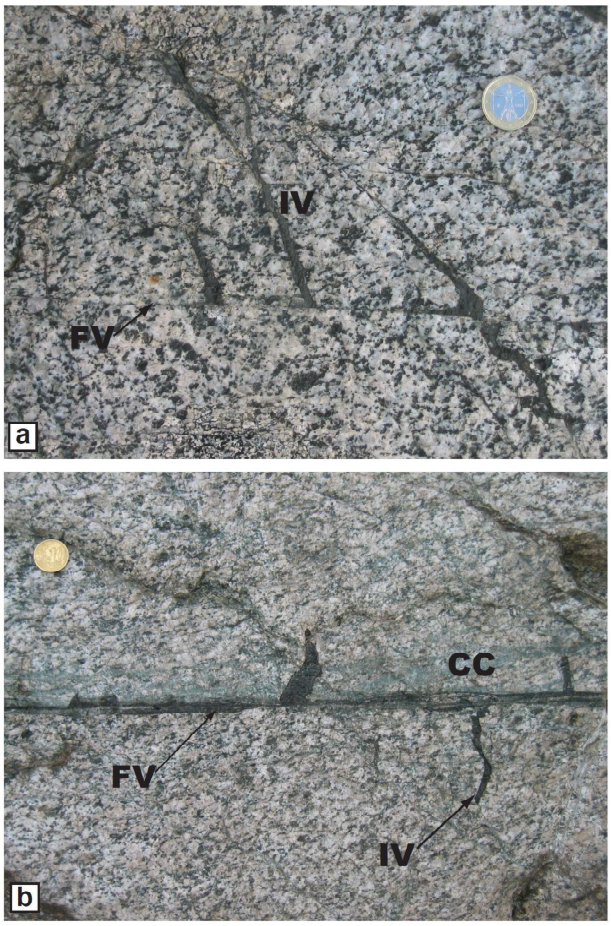

FIGURE 2. Field photographs of fault rocks of the GLFZ. (a) A pseudotachylyte-bearing fault in tonalite, composed of a fault vein (FV) and injection veins (IV); most of the pseudotachylyte volume (black in color) is concentrated in the injection veins. (b) A pseudotachylyte hosted in cataclasite (CC, green in color); pseudotachylyte fault and injection veins clearly intrude and postdate the cataclasite.

Cataclasites and pseudotachylytes of the GLFZ were described by Di Toro and Pennacchioni (2004; 2005) and Pennacchioni et al. (2006). The cataclasites are green and contain lithic clasts of (often altered) tonalite and reworked cataclasite, cemented by micrometric epidote+K-feldspar+chlorite (Fig. 2b, 3a).

The pseudotachylytes are sharply-bounded veins, occurring both as fault veins and injection veins (Fig. 2), whose thickness varies from about 0.5mm up to 10-20 cm in pull-apart structures. Most of the pseudotachylyte volume is concentrated in injection veins (after Sibson, 1975) branching at high angle from the slipping zone (Fig. 2). Pseudotachylytes are mostly associated with

precursor cataclasites, except in a few fault branches where they occur within intact tonalite (Fig. 2a) (Pittarello et al., 2008). Pseudotachylytes are composed of angular clasts embedded in a

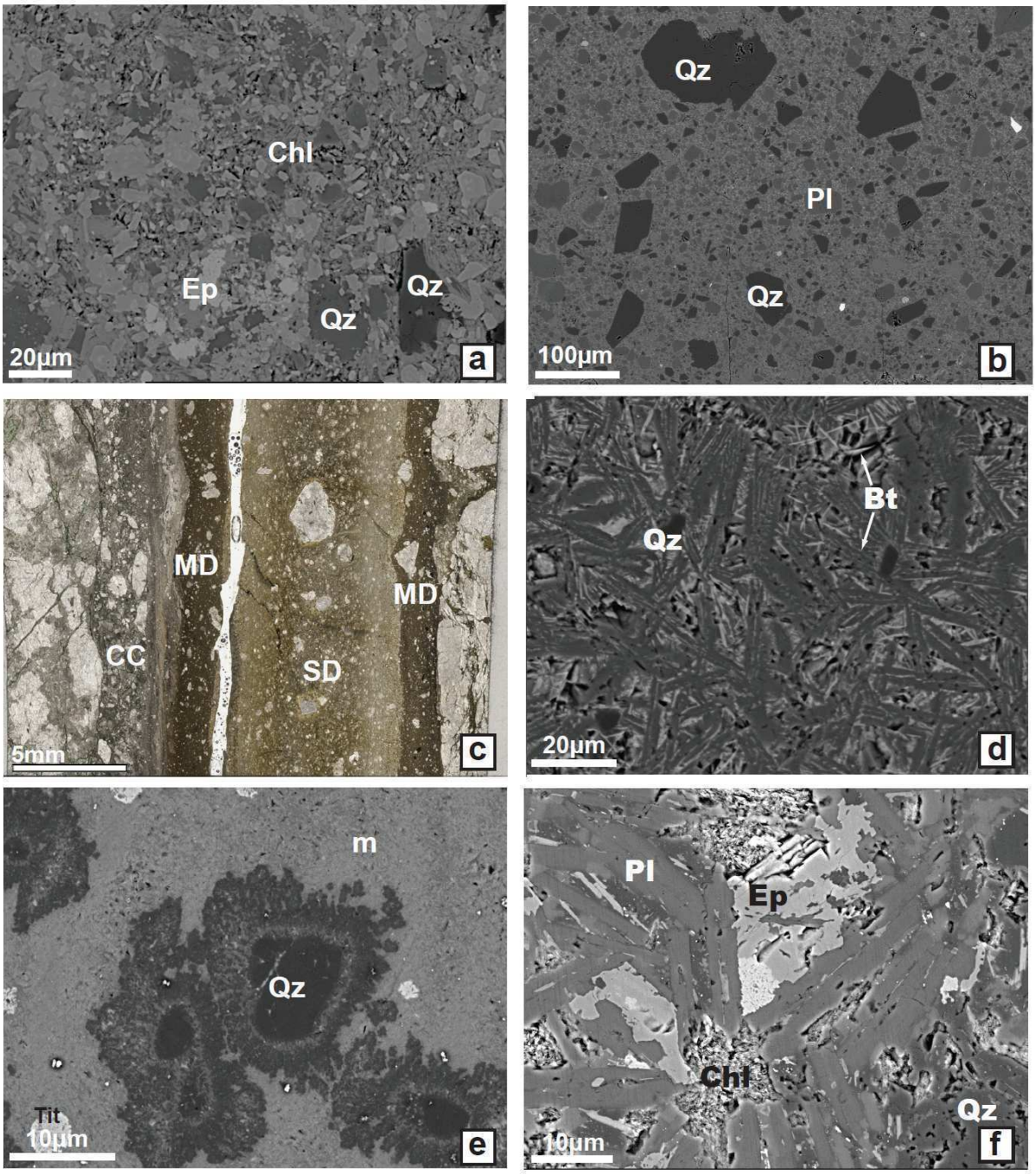

FIGURE 3. Microstructures of fault rocks of the Gole Larghe Fault. (a) SEM-BSE image of the cataclasite matrix. Clasts of quartz (Qz) are embedded in a matrix of randomly oriented epidote (Ep) and chlorite (Chl). (b) SEM-BSE image of a thin (4 mm thick) pseudotachylyte fault vein, composed of angular clasts of quartz (Qz) and plagioclase (Pl) embedded in a microcrystalline to cryptocrystalline matrix. (c) Thin section scan, plane polarized light of a zoned pseudotachylyte fault vein, cutting cataclasite (CC); the microlitic domains (MD) are

brownish in color and have very sharp contacts with the inner, pale green in color, spherulitic domain (SD). (d) SEM-BSE image of a microlitic domain, composed of an intergrowth randomly oriented plagioclase microlites (dark grey) surrounding quartz (Qz) clasts; bright biotite (Bt) lamellae are enclosed in the plagioclase microlites. (e) FE-SEM BSE image of spherulites developed around quartz clasts. The cryptocrystalline matrix is formed of a coalescence of sub-micrometric biotite and other phases. (f) FE-SEM BSE image of a detail of the microstructure of sample 13-01, where the original plagioclase (Pl) and biotite microlites are overprinted by hydrothermal epidote (Ep) and chlorite (Chl).

microcrystalline or cryptocrystalline matrix. The clasts consist of quartz, plagioclase and K-feldspar and, locally, cataclasite and altered pseudotachylyte. In thin (<4mm) pseudotachylyte veins, the matrix is composed of an intergrowth of lath shaped plagioclase and acicular biotite microlites (Fig. 3b, d). Thick veins show a symmetrical zoning with "chilled" microlitic margins, bordering a central domain composed of spherulitic aggregates floating in a cryptocrystalline matrix (Di Toro and Pennacchioni, 2004) (Fig. 3c). The spherulites are formed of plagioclase microlites radially arranged around plagioclase clast cores, or of silica-rich and K-feldspar-rich concentric rims surrounding quartz clasts (Fig. 3e). The cryptocrystalline matrix in the spherulitic domains is formed of an aggregate of sub-micrometric biotite and of analytically unresolvable (under the EDS-equipped SEM) phases (probably plagioclase and K-feldspar) (Fig.3e). Most of the analyzed pseudotachylytes escaped alteration except sample 13-01, where epidote and chlorite overprint the microlitic aggregate (Fig. 3f).

4.4.3 Artificial pseudotachylytes

pseudotachylytes were produced in high velocity friction experiments performed on tonalites and cataclasites sampled within the GLFZ with the HV-1 rotary shear apparatus (for a description of the apparatus, see Shimamoto and Tsutsumi, 1994; Hirose and Shimamoto, 2005). A pair of rock cylinders (22.3-22.5 mm in diameter) was used for each experiment. To impose normal stresses up to 20 MPa, the samples were jacketed in aluminium rings, but without confining the slipping zone (i.e., powders and melt could extrude from the slipping zone). During the experiments, the sliding velocity was 1.75 ms^{-1} at the outer boundary of the specimen, corresponded to a linear slip rate of about 1.2 ms^{-1}), and under an imposed normal stress of 5, 10, 12.5, 15 and 20 MPa. All the experiments were conducted at room temperature and room humidity conditions (for a description of the experimental methods and results, see Di Toro *et al.*, 2006a; 2006b). During the experiments,

after the initial expulsion of powders of crushed material, the slip surfaces melted (see video in Supplementary material of Di Toro et al., 2006a). Since the slipping zone was not confined, most of the melt was extruded and a thin (<0.5mm) melt layer solidified on the artificial fault at the end of the experiment, welding the samples (Fig. 4a, d, g). Polished rock thick sections were cut parallel to the cylinder axis perpendicular to the slipping zone and examined under the SEM.

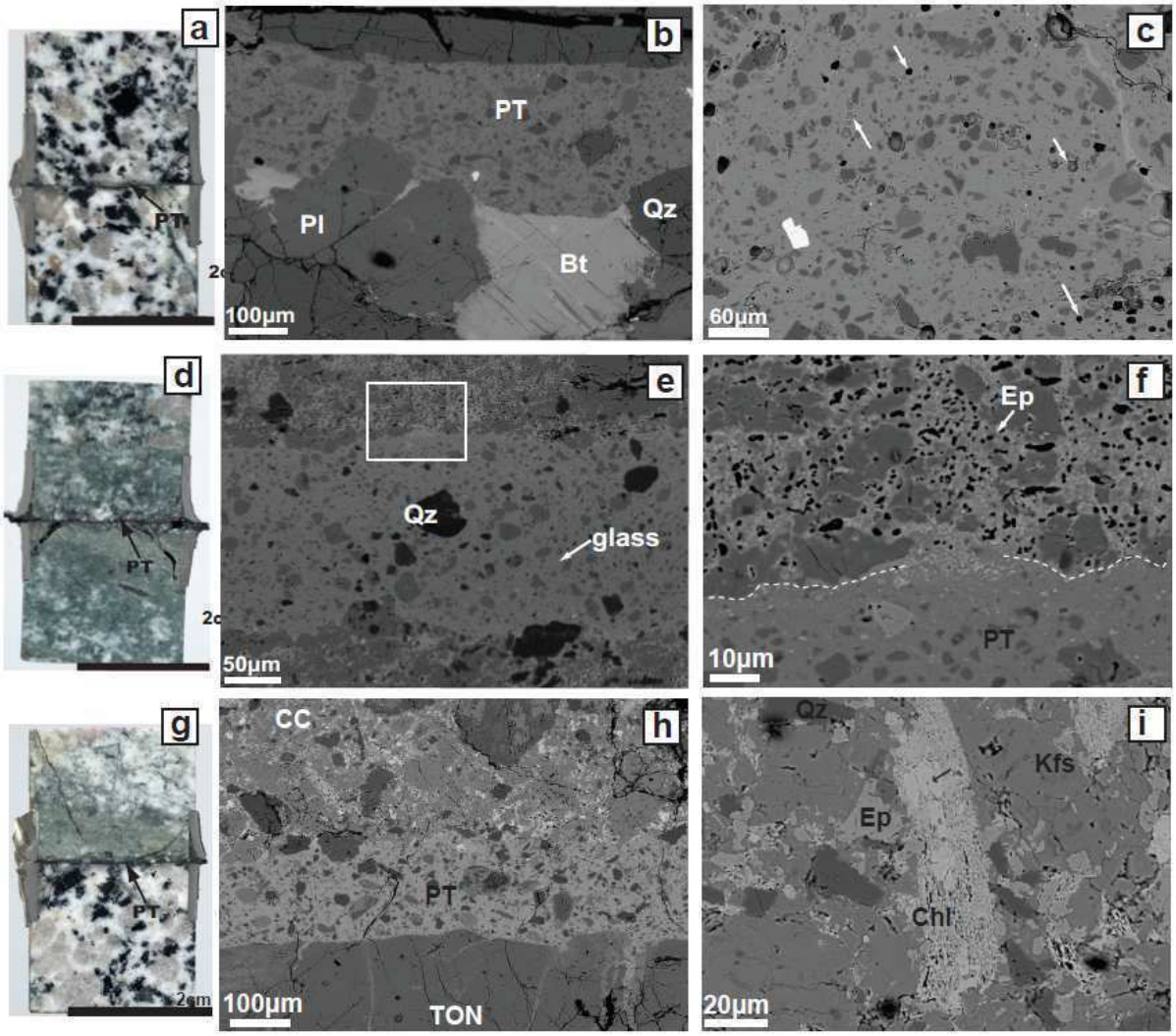

FIGURE 4. Microstructures of the artificial pseudotachylytes and host rocks. (a) Polished sample of two tonalite cylinders welded, after the experiment, by a thin layer of artificial pseudotachylyte (black in color). (b) SEM-BSE image of the artificial pseudotachylyte (PT) in tonalite; the PT-tonalite boundary has deep embyments due to preferential melting of biotite (Bt) grains. (c) SEM-BSE image, a detail of the PT in tonalite. Angular quartz (Qz) and plagioclase (Pl) fragments are floating in glass. The rounded features (white arrows) are visicles in glass. (d) Polished sample of two cataclasite (green in color) cylinders welded, after the experiment, by a thin layer of artificial pseudotachylyte (black). (e) SEM-BSE image of the artificial pseudotachylyte (PT) in cataclasite; the cataclasite adjacent to the pseudotachylyte (PT) shows a pervasive porosity, and the PT-

cataclasite boundaries are rough at the scale of the cataclasite grains. The rectangle shows the area enlarged in Fig. 4f. (f) Detailof the contact between pseudotachylyte and cataclasite; note the evanescent and irregular boundary between melt and cataclasite (dotted lines), due to incipient melting of the low-melting point minerals (chlorite and epidote), while plagioclase grains (Pl) are not affected by melting. (g) Polished section of a cylinder of tonalite and one of cataclasite welded together by a thin layer of artificial pseudotachylyte (black).(h) SEM-BSE image of the artificial pseudotachylyte (PT) between cataclasite and tonalite; the cataclasite shows a pervasive porosity, while, on the opposite side, the boundary with tonalite is stright. (i) Further away from the melt-cataclasite boundary, where heating was less intense, chlorite grains (Chl) shows incipient melting, while epidote (Ep) is unaffected by melting.

The artificial pseudotachylyte had a microstructure very similar to the natural one (compare Fig. 4e with Fig. 3b, c). Artificial pseudotachylytes are formed by clasts of quartz, plagioclase and K-feldspar suspended in a matrix inferred to be glass from its uniform texture (Figure 4b, c, e). In some of the samples, the glass includes round-shaped vesicles (Fig. 4c). Compared with the starting tonalite, the glass composition (average of six microprobe point analyses performed in areas without evidence of the presence of clasts) shows (Table 2): (i) a lower content of SiO_2 (52.2wt % vs. 66.5 wt %), (ii) a higher content of Al_2O_3 (22.1wt% vs. 16.5 wt %), FeO (7.7% vs. 3.4 wt %), MgO (3.9% vs. 1.6 wt %), K_2O (4.18% vs. 2.2 wt %) and TiO_2 (1.1% vs. 0.5 wt %), and (iii) a similar content of CaO (4.8% vs. 4.4 wt %), and Na_2O (2.88% vs. 2.9 wt %).

The boundaries between the pseudotachylyte layers and the wall rocks have different roughness depending on the grainsize and the mineral and modal composition of the host rock. In tonalite, the boundary has embayments (due to preferential wear and melting) in the presence of biotite (Fig. 4b), and it is straight in the presence of quartz and plagioclase. In cataclasite, the boundary profile is rough at the micrometer scale due to preferential wear and melting of micrometric grains of chlorite and epidote(Fig. 4e, f). Inside the rock cylinders, cataclasite is vesiculated over a distance of 150-200µm from the slip surface, due to the breakdown and selective melting of epidote and chlorite grains. At further distance from the pseudotachylyte-cataclasite boundary, vesiculation and break down structures are seen only in chlorite (Fig. 4i), while nearby epidote grains are unaffected.

4.5 Mineralogical and chemical composition

Four samples of natural pseudotachylytes (including the matrix and suspended clasts) were analyzed by means of XRD: three pseudotachylytes samples within cataclasite (46-99-pt, 32-00-pt,

13-01-pt) and one pseudotachylyte sample within tonalite (10-04-pt). The pseudotachylytes are composed of quartz, plagioclase, dmisteinbergite, biotite, indialite (46-99-pt and 32-00-pt) and scapolite (46-99-pt and 32-00-pt). The biotite peak at 10Å is anomalously broad. To test if the broadness of the peak is due to the occurrence of smectite as sub-micrometric interlayers in biotite, the sample was treated with ethylene glycol and heated up to 800°C (Moore and Reynolds, 1997). The treated sample does not show any change in the spectrum profile, which suggests that the broad peak in untreated samples is actually due to the nanometric size of the crystallites of biotite in the spherulitic domains (e.g., Langford and Wilson, 1978). The sample 13-01-pt is mainly composed of quartz, plagioclase, biotite, and significant amounts of epidote (7%) and chlorite (6%); no anomalies in the biotite spectrum are present.

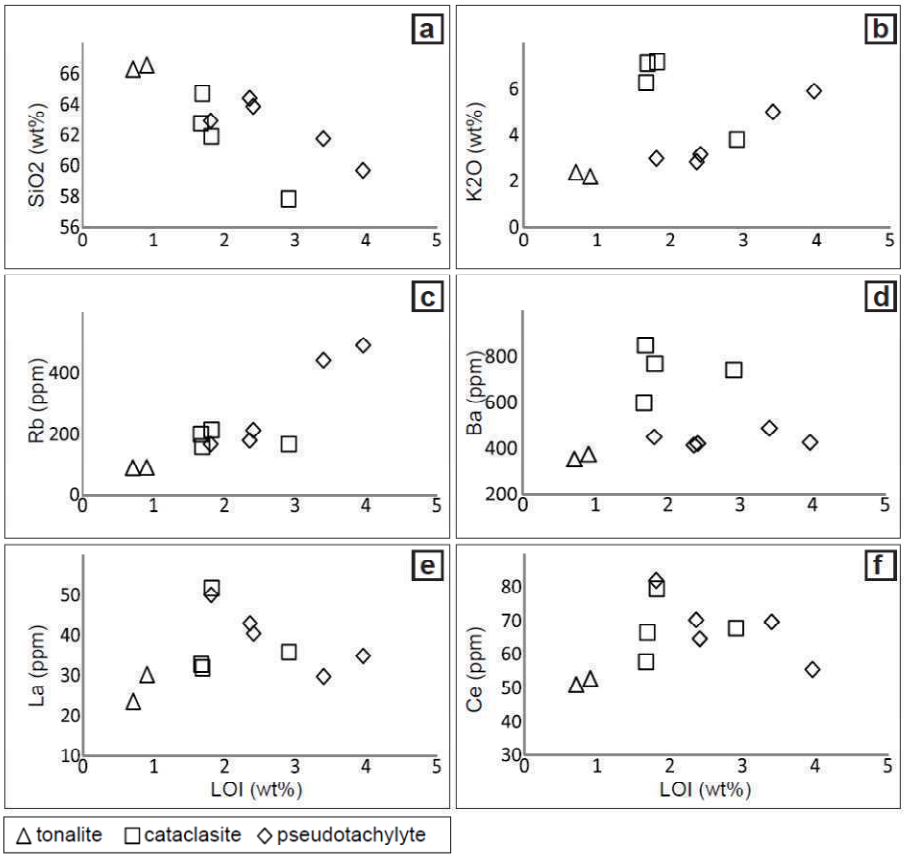

FIGURE 5. Major (in oxides) and trace elements (in ppm) plotted vs. the volatile content (LOI), data from Table 2. See text for discussion.

The bulk elemental composition from XRF analyses of some representative samples of the main rock types of the Gole Larghe Fault Zone was published in previous studies (Di Toro and Pennacchioni, 2005; Pennacchioni et al., 2006); the data are reported in Table 2. The cataclasites are strongly

enriched in Fe_2O_3, K_2O, LOI (Loss On Ignition), Rb, Ba and U; the pseudotachylytes have a similar chemical composition, suggesting that they formed by melting of the already cemented cataclasites (Di Toro and Pennacchioni, 2005; Pennacchioni et al., 2006). Selected elements have been plotted against the bulk content in LOI for the different rocks in Figure 5. Pseudotachylytes are enriched in K_2O, Rb, Ba, La, Ce, similar to cataclasites (Table 2, Fig. 5) and frictional melting likely occurred in cataclasites already cemented by late magmatic in origin, LILE (Large Ion Litophile Elements) – enriched fluids (Di Toro and Pennacchioni, 2004). Field observations of the intrusive relations of pseudotachylytes suggest that frictional melting occurred in cemented cataclasites, since fault and injection veins cut and intrude cataclasite and tonalite in similar way (Figure 2a and 2b). Frictional heating during seismic slip induces non-equilibrium melting of the wall rocks (Spray 1992), with selective melting of the low melting point minerals (such as biotite). As a consequence, the composition of the melt is enriched of the elements from the low melting point minerals (e.g., Fe and Mg from biotite) and depleted in the elements from the high melting point minerals (e.g., Si from quartz), with respect to the wall rocks (Shand, 1916). Figure 5 reports a positive correlation between volatile (i.e., LOI) content and K_2O and Rb, and a negative correlation between volatile content and SiO_2. Most likely volatiles, K_2O and Rb, share a common source (i.e. biotite) and the more biotite was melted, the more the melt is enriched in volatiles, K_2O and Rb. Because quartz has the highest melting temperature among the tonalite-forming minerals, the observed SiO_2-volatile inverse correlation can be the result of (i) selective melting and (ii) increasing degree of melting of SiO_2-poor minerals. Most pseudotachylytes show no correlation among volatiles and Ba, La and Ce contents (Fig. 5d, e, f).

TABLE 2. XRF bulk rocks composition of fault and host rocks of the Gole Larghe Fault and average of point EMPA analysis of the glass produced in experiments. ton: tonalite, av: average. XRF (c) are pseudotachylyte bulk chemical compositions recalculated subtracting the clast content (Di Toro and Pennacchioni, 2004).

	av. ton	st dev	av. cc	st dev	46-99-pt	46-99-pt	24-00-pt	24-00-pt	32-00-pt	20b-00-m-pt	20b-00-m-pt	20b-00-s-pt	20b-00-s-pt	av. glass exp. pt	st dev
	XRF (5 data)		XRF (4 data)		XRF	XRF (c)	XRF	XRF (c)	XRF	XRF	XRF (c)	XRF	XRF (c)	EMPA (6 data)	
SiO_2	66.56	0.94	61.86	2.35	59.69	55.05	63.89	60.08	61.78	62.95	58.99	64.42	61.08	52.21	0.33
TiO_2	0.46	0.05	0.57	0.05	0.55	0.65	0.53	0.66	0.55	0.54	0.63	0.53	0.59	1.16	0.07
Al_2O_3	16.53	0.37	17.71	1.06	17.13	19.03	16.57	17.76	17.06	17.00	18.93	16.68	18.24	22.11	0.28
FeO	3.41	0.29	3.71	0.48	3.09	3.65	3.19	3.99	3.50	3.74	4.34	3.19	3.59	7.71	0.25
Fe_2O_3	0.33	0.08	0.96	0.08	2.00	2.36	1.22	1.51	0.83	0.87	1.00	0.92	1.03		
MnO	0.10	0.01	0.12	0.03	0.11	0.12	0.12	0.13	0.13	0.14	0.16	0.10	0.11	0.26	0.03
MgO	1.57	0.18	1.94	0.21	1.95	2.31	1.77	2.22	1.84	1.91	2.22	1.71	1.92	3.92	0.19
CaO	4.44	0.15	4.16	0.24	3.55	3.77	3.58	3.44	3.62	4.09	4.47	3.89	4.19	4.84	0.18
Na_2O	2.95	0.05	3.25	0.23	1.26	1.21	3.03	3.12	1.59	3.22	3.56	2.99	3.25	2.88	0.16
K_2O	2.20	0.11	3.11	0.26	5.92	6.99	3.15	3.90	5.02	2.98	3.44	2.83	3.18	4.18	0.13
P_2O_5	0.11	0.01	0.15	0.01	0.13	0.16	0.13	0.16	0.14	0.14	0.16	0.14	0.15		
L.O.I.	0.91	0.07	2.23	0.36	3.96	4.69	2.41	3.03	3.40	1.81	2.10	2.36	2.66		
Tot	99.56	0.14	99.78	0.29	99.34	100	99.58	100	99.45	99.39	100	99.74	100	99.27	0.46
V	57.9	6.5	70.80	1.70	67.5		67.5		66.8	69.6		72.0			
Rb	90.4	12.6	173.85	8.70	492.4		213.7		443.0	167.7		180.0			
Sr	225.2	9.7	238.75	12.23	196.7		235.8		221.8	247.4		230.1			
Y	26.4	5.6	31.70	0.42	30.4		32.2		28.9	32.0		31.4			
Zr	117.0	9.7	135.50	0.42	136.4		134.9		139.9	135.2		135.8			
Nb	10.2	1.0	12.05	0.64	12.3		10.8		12.5	12.5		11.6			
Ba	374.8	25.3	433.40	25.46	427.2		422.1		489.7	451.4		415.4			
La	30.3	4.5	46.60	4.95	34.9		40.5		29.8	50.1		43.1			
Ce	52.8	15.2	76.20	8.20	55.5		64.7		69.8	82.0		70.4			
Nd	23.2	7.3	21.85	7.00	29.3		31.8		10.1	26.8		16.9			
U	3.2	0.5	6.25	0.35	17.6		7.7		16.2	6.0		6.5			

4.6 The water content

The water content in bulk tonalite is 0.96% from CHN analyses (Table 3). The LOI value in tonalite ranges between 0.71 and 0.91 wt.% (Table 2), suggesting that the volatiles are mostly composed of water. Considering a modal content of biotite of 17% (Di Toro and Pennacchioni, 2004), the volatiles are most likely derived from OH in biotite.

The water content in mylonites is of 14 – 1.7%, slightly higher than in the bulk tonalite. It is to be noticed that biotite rich ultramylonites were sampled for these measurements.

The water content of biotites from CHN analysis is of 3.49 - 4.24%. The high content in water of some of the samples might be interpreted as due to the occurrence of chlorite interlayers inside the biotite lattice (see the large biotite grain in Fig. 4b).

The bulk natural pseudotachylyte samples have a water content ranging between 2.33 and 4.41%. The water content (2.33 - 4.41%) is higher than expected for a modal content of biotite of 17% as estimated by Rietveld refinement in pseudotachylyte (Nestola et al., 2010): for such biotite abundance we would expect a 0.7% of water.

Although the experiments were performed without confining the slipping zone (i.e., frictional melts could potentially degas) the artificial pseudotachylytes produced from tonalites and cataclasites have a water content of 0.85% – 2.44%, similar to the values of their respective protoliths.

4.7 FTIR spectroscopy in pseudotachylytes

As discussed above, the content of water in pseudotachylytes is higher than expected for a modal content of biotite of 17% (for instance, a rock with bulk water content of 4.24% would be composed only of biotite). The presence of clay minerals has been excluded by XRD analyses at temperature up to 800°C, glass is not seen in XRD analyses, and was not found in TEM investigations on some of the samples analyzed (Di Toro and Pennacchioni, 2004). The structural position of water was thus investigated by infrared (FTIR) spectroscopy.

The absorbance spectra were acquired in the range of wavenumbers 1400 – 4000 cm^{-1}, in order to identify the main peaks of vibration of water: the OH stretch region (2700 cm^{-1} – 3650 cm^{-1}), which is produced in both molecular water and hydroxyl ions in minerals, and the peak of the H-O-H bending (1630 cm^{-1}), indicative of the presence of molecular water.

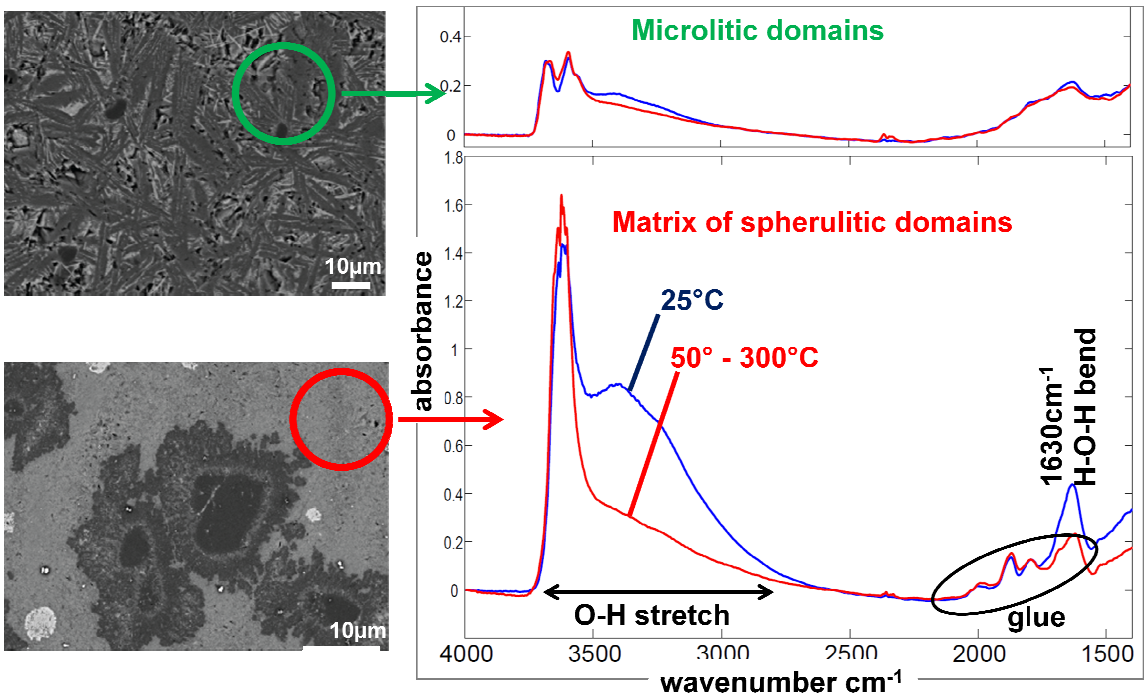

FIGURE 6. Absorbance infrared spectra of microlitic domains and the matrix of spherulitic domains.

In microlitic domains, two peaks in the region of the OH stretching are measured and theshape of the spectrum doesn't change by heating up to 300°C. In the cryptocrystalline matrix of the spherulitic domains, an intense peak is found in the OH stretch region (3600 cm^{-1}), with a broad shoulder towards lower wavenumber. A peak in the HOH bending region is present as well (although in the region 1500 – 2000 cm^{-1} there are some peaks due to the presence of glue). Upon heating over 50°C under vacuum, the shoulder in the OH region and the peak at 1603 cm^{-1} (HOH bending) disappear (Figure 6). This is indicative of loosely bonded molecular water, which might explain the anomalously high water content of the pseudotachylytes.

4.8. Hydrogen isotope composition

The hydrogen isotope compositions of the analyzed samples are listed in Table 3 together with the volatile composition from CHN analyses. The hydrogen isotope composition of the bulk tonalite is most likely represented by the H-isotope composition of biotite, for which a δD value of -74 ± 1 ‰ was measured. The hydrogen isotope composition of bulk mylonites is -77 and -79 ‰, slightly lower than the host tonalite.

Hydrogen isotope compositions of cataclasites are clustered in the interval 65 ± 4 ‰. The large span in H_2O contents and δD depends on the variable modal abundance of epidote and chlorite, the hydrogen bearing minerals in cataclasite.

The hydrogen isotope composition of the bulk natural pseudotachylytes is in the range -92 ± 13.1 ‰. Disregarding subsamples 13-01-pta and 13-01-ptb, where there is evidence of overgrowth of epidote and chlorite (Fig. 3f), the range of hydrogen isotope composition decreases to -93 ± 9.2 ‰, with all but one sample exhibiting a range of -103 to -85‰. The microlitic and spherulitic domains (Fig. 3c) of the pseudotachylyte veins have been analyzed separately and have similar isotope composition in the limits of the instrumental resolution.

The δD value of artificial pseudotachylytes obtained from tonalite is δD= -75±2‰, and that of pseudotachylytes produced using at least one cylinder of cataclasite is δD = -83±1.3‰. Thus, the artificial pseudotachylytes produced from frictional melting of tonalites have δD indistinguishable from that of the source tonalite. In contrast, the artificial pseudotachylytes produced from cataclasites have δD lower by ~20‰ than that of the source cataclasite.

Sample	Outcrop	Lithology	H2O %	δD ‰ mean	st. dev.
06 19 HR Bt	Passo Cercen	biotite (in host tonalite)	4.7	-76.9	3.3
G5 Bt HR	Val d'Avio	biotite (in host tonalite)	4.1	-73.8	2.2
Ad2 99 Bt HR	Vedretta Lobbia	biotite (in host tonalite)	4.2	-75.1	0.4
07 162	Vedretta Lobbia	mylonite	1.4	-77.7	2.4
99 D7 umyl	Vedretta Lobbia	mylonite	1.7	-79.7	3.7
L65 cc	Vedretta Lobbia	cataclasite	2.9	-68.8	0.9
P4407 cc	Vedretta Lobbia	cataclasite	2.3	-67.8	1.3
Ad46 99 cc	Vedretta Lobbia	cataclasite	2.2	-61.6	2.8
24 00 cc	Vedretta Lobbia	cataclasite	2.0	-64.8	0.5
32 00 cc	Vedretta Lobbia	cataclasite	2.3	-66.9	4.7
2d 2001 cc	Vedretta Lobbia	cataclasite	2.3	-61.9	6.9
11d 2001 cc	Vedretta Lobbia	cataclasite	3.2	-65.4	2.8
17 01 cc	Vedretta Lobbia	cataclasite	2.4	-66.3	5.9
19M 01 cc	Vedretta Lobbia	cataclasite	1.0	-64.1	11.2
21 01 cc	Vedretta Lobbia	cataclasite	1.8	-69.1	10.3
371 cc	Vedretta Lobbia	cataclasite	2.0	-60.4	4.5
378 cc	Vedretta Lobbia	cataclasite	1.7	-68.9	0.2
379 cc	Vedretta Lobbia	cataclasite	1.3	-65.3	4.2
380 cc	Vedretta Lobbia	cataclasite	1.8	-65.4	2.7
L65	Val d'Avio	pseudotachylyte	2.6	-87.6	1.9

P 29 07 W	Passo Cercen	pseudotachylyte	3.0	-88.7	4.6
Ad 2	Vedretta Lobbia	pseudotachylyte	3.1	-89.6	2.5
Ad46	Vedretta Lobbia	pseudotachylyte	3.9	-94.4	3.6
24 00	Vedretta Lobbia	pseudotachylyte	4.2	-97.5	4.7
32 00	Vedretta Lobbia	pseudotachylyte	4.4	-103.6	3.3
2up 2001	Vedretta Lobbia	pseudotachylyte	3.1	-95.6	1.3
11u 2001	Vedretta Lobbia	pseudotachylyte	2.8	-92.2	0.1
13Mb	Vedretta Lobbia	pseudotachylyte	2.3	-77.4	0.5
17 01	Vedretta Lobbia	pseudotachylyte	3.8	-93.7	4.9
19M01	Vedretta Lobbia	pseudotachylyte	2.4	-90.8	4.3
21 01	Vedretta Lobbia	pseudotachylyte	3.6	-89.4	4.0
3 02	Vedretta Lobbia	pseudotachylyte	3.0	-96.0	2.7
Ad10 04	Vedretta Lobbia	pseudotachylyte	2.8	-94.9	5.1
370	Artificial ton/ton	pseudotachylyte	1.9	-74.0	2.5
371 II	Artificial cc/cc	pseudotachylyte	1.8	-84.7	2.2
372	Artificial ton/ton	pseudotachylyte	1.4	-73.7	1.0
376 II	Artificial ton/ton	pseudotachylyte	0.8	-75.9	4.7
378	Artificial cc/cc	pseudotachylyte	2.4	-82.0	4.3
379	Artificial cc/ton	pseudotachylyte	1.5	-83.2	6.0

Table 3. Summary of the results of TC/EA analyses (δD‰) and CHN analyses (H_2O contents in wt%).

4.9 Discussion

4.9.1 The artificial pseudotachylytes

In artificial pseudotachylytes, the sources of hydrogen which can potentially be dissolved in the frictional melt are the hydroxyl ions in hydrous minerals of the starting rocks. Ingress of room humudity in the slipping zone during the experiments is impeded by (i) the large applied normal stress (50 to 200 atmospheres), (ii) the extrusion of hot material and (iii) the centrifugal forces due to the high revolution rates of the sample (1500 rpm). The specimen surfaces are ground and the powders are expelled before the onset of melting, so the possible layer of humidity adsorbed on the specimen surfaces probably do not enter the melt. Thus, the main source of hydrogen is probably the hydroxyl ions in hydrous minerals of cataclasite and tonalite. The pseudotachylytes produced in tonalite retain indeed a δD indistinguishable from that of biotite in tonalite (Fig. 6a), while pseudotachylytes produced in cataclasite have δD lower by ~20‰ than the source cataclasite. Based on microstructural observations, process that might have caused isotopic fractionation during melting are: (i) degassing of the melt, as suggested by the occurrence of vesicles and bubbles within

the glass of some artificial pseudotachylytes (Fig. 4c); (ii) selective melting and breakdown of chlorite and epidote within the shear heated cataclasite along the slipping surfaces, as suggested by vesiculation in cataclasite close to artificial pseudotachylytes (Fig. 4e, f, h, i). Hydrogen fractionation due to degassing is accompanied by a loss of water from the melt, as seen in volcanic glasses (Taylor et al., 1983; Rust et al., 2004; De Hoog et al., 2009). Instead, the H-isotope composition of artificial pseudotachylytes has a weak inverse correlation with the water content: the higher the water content, the lower the H-isotope ratio. In our samples, the water content of artificial pseudotachylytes is higher or equal to the water content of the source rock. For causing the -20‰ isotopic shift of artificial pseudotachylytes from the source cataclasites, a loss of water would have been required. Degassing should have affected both melts produced in tonalite and cataclasite, while the negative shift in hydrogen isotope composition is observed only in samples obtained in cataclasite.

Shear heating of the rock adjacent to the melt layer occurs during the experiments. When a continuous layer of melt forms in the slipping zone, after about 1-2 s of slip, steady state conditions are achieved, meaning that the fault is lubricated and the shortening rate of the sample, about, 0.5 mm s^{-1} , is constant (Fig. 2 in Di Toro et al., 2006a). Sample shortening results from a balance between the solid rock entering in the slipping zone and the melt extruded from the slipping zone (Nielsen et al., 2008). Under these experimental conditions, the temperature in the wall rocks increases because the rock migrates towards the slipping zone pushed by the applied normal stress and because of the heat diffusion from the slipping zone towards the wall rocks. The effects of the thermal perturbation in the wall rocks bounding the slipping zone are evident in cataclasite (Fig. 4e, f, h, i): chlorite and epidote grains show evidences of selective melting, break down and vesiculation, which are more intense close to the cataclasite–melt interface. In the experiments with tonalites, biotite grains, which have melting temperature of about 650°C (Spray 1992), are preferentially melted forming embayments along the rock-melt interface, and have vesiculation and selective melting features in the wall rocks bordering the slipping zone (Fig. 4i). Biotite in tonalite occurs as sparse, millimeter-sized crystals, so that few grains intersect the slipping zone and can be heated and degassed (Fig. 4a-c): the proportion of low δD hydrogen could possibly be buffered by the δD of the totally melted biotite. Instead, micrometric chlorite and epidote in cataclasite form a continuous layer bordering the slipping zone (Fig. 4d-f): their degassing and fractionation could potentially affect the bulk isotopic composition of the frictional melt.

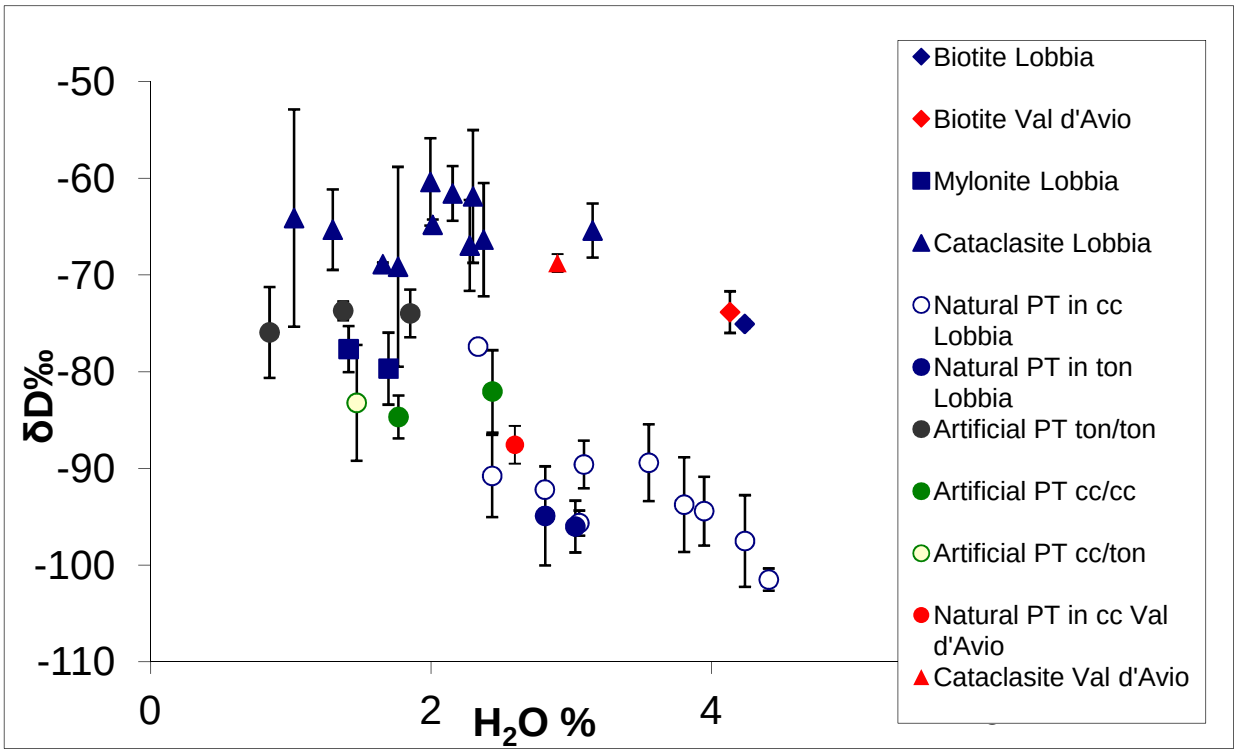

FIGURE 6. Plot of the δD vs. the water content of host rocks and artificial and natural pseudotachylytes from the GLFZ (Table 3). (a) Hydrogen isotope compositions plotted vs. water content for biotite, cataclasite, natural and artificial pseudotachylytes of the GLFZ. The data are well clustered following their lithology.

4.9.2 The Avio tonalite and the GLFZ natural fault rocks

The biotite in the Val d'Avio tonalite has δD of -74 ± 1 ‰, a value consistent with the composition of biotite in plutonic rocks measured worldwide (Taylor, 1978). The two samples of mylonite analyzed have very similar hydrogen isotope composition, (δD = -75 ‰ and -79 ‰), implying no ingression of an external fluid. The -4 ‰ shift of δD measured in one sample can be due to the recrystallization of biotite (Bt_2 in Pennacchioni, 2005) at T=550°C estimated for the mylonitic deformation. A Rayleigh fractionation between water with δD = -74 ± 1 ‰ and biotite at such temperature would produce a -4 ‰ isotopic shift with a loss of water of 1% (using the fractionation coefficient of Suzuoki and Epstein, 1976). Instead, cataclasites have higher δD values (-65 ± 4 ‰). The hydrogen bearing minerals in cataclasites are chlorite and epidote, which have micrometric

grainsize and cement the cataclasite matrix (e.g., Di Toro and Pennacchioni, 2005). The hydrogen isotope composition of bulk cataclasites can be evaluated as

$$\delta D_{ccbulk} = \chi_{ep}\delta D_{ep} + \chi_{chl}\delta D_{chl} = \chi_{ep}(\delta D_w + 1000\ln\alpha_{ep-w}) + \chi_{chl}(\delta D_w + 1000\ln\alpha_{chl-w}), \quad (1)$$

where χ are the molar fraction of water hosted in epidote and chlorite. We calculated the hydrogen isotope composition of water in equilibrium with epidote and chlorite based on the fractionation coefficients for epidote (Graham et al.1987) and chlorite (Graham et al., 1980) at 250°C. Assuming a mean modal content of chlorite and epidote of 6.2% and 11.8% respectively, as obtained averaging eleven semiquantitative modal compositions from XRPD analysis (Di Toro and Pennacchioni, 2005), the composition of water is of -41 ± 4.25‰ (Graham et al., 1980; 1987). These values of δD are in the field of magmatic water (-80 < δD < - 40‰, Taylor 1974). A late magmatic origin of the fluids cementing cataclasites was suggested by Di Toro and Pennacchioni (2005) based on the enrichment in LILE in cataclasite. The seismic activity of the GLFZ was contemporary to the intrusion and cooling of the Presanella pluton (Del Moro et al., 1983), located few km north from the studied outcrops (Fig. 1a), so a late magmatic origin of the fluids involved in the fault zone is likely. The ingression of low D meteoric fluids during the hydrothermal cementation of cataclasites is thus excluded.

The pseudotachylyte sample (13-01) where a detectable amount of epidote and chlorite is present (Fig. 3f) as an overgrowth on the microlitic texture, has the highest δD values among the natural pseudotachylytes (-83 < δD < -77‰). The other natural pseudotachylyte samples have δD values in the range -93.2 ± 9.2 ‰, lower by ~20 - 40‰ than cataclasites, confirming that most psedotachylytes do not bear a significant amount of epidote and chlorite, as observed under the SEM and in XRPD analysis. Likely, the mineral parageneses of pseudotachylytes were not significantly modified by minerals precipitated from fluids associated with cataclasites, neither did they isotopically equilibrate with the (relatively) high-D fluids associated with the cementation of cataclasites. If the source of hydrogen dissolved in the frictional melts is the OH groups in hydrated minerals of the host cataclasite and tonalite, the melt is expected to retain the hydrogen composition of the source minerals.

The negative shift measured in the natural pseudotachylytes is likely related with the occurrence of weakly bounded adsorbed water within the matrix of the spherulitic domains in pseudotachylytes. Here, we try to estimate the hydrogen isotope composition of the spherulite matrix in one of the pseudotachylyte samples. As suggested by infrared spectroscopy, the water in pseudotachylytes is present as: (i) hydroxyl ions in biotite (in both microlitic and spherulitic domains) (ii) adsorbed molecular water. By knowing the hydrogen isotope composition of bulk

pseudotachylyte (in this example, δD_{PTbulk} = -95 ‰), the amount of biotite (17% in weight) and thus the molar fraction of hydrogen hosted in biotite, and assuming that biotite has the same δD value as the biotite in the host (-75‰), we can calculate the isotopic composition of the adsorbed water (δD_x):

$$\delta D_{PTbulk} = \chi_{Bt}\delta D_{Bt} + \chi_x\delta D_x \quad (2)$$

$$\delta D_x \approx -104‰ \quad (3)$$

This value is in agreement with the hydrogen isotope compositions of rainfalls over the region close to the Adamello collected by Longinelli and Selmo (2003). Correcting the data for nearby stations (Campo Carlo Magno) for the altitude of the sampling site (2800m), the δD value of rainfalls at results -97‰. The measured δD values in natural pseudotachylytes are thus lowered by the adsorbtion of low δD value water from local rainfall. This effect should be more intense in pseudotachylytes containing an higher volume of cryprocrystalline matrix . As shown in section 4.7, the microlitic domains do not bear adsorbed molecular water, so they are likely to retain an hydrogen isotope composition closer to the primitive composition of biotite crystallized from the melt (thus shifted to higher δD).

Following this esteem, the hydrogen isotope composition of the bulk pseudotachylytes has probably δD values higher than measured (about -75 to -85‰), thus closer to the δD values of the pseudotachylytes produced in high velocity friction experiments. Since the source rock of most of the pseudotachylytes is in cataclasite, this implies a negative shift of the hydrogen isotope composition from the δD values of cataclasites (-65 ± 4 ‰) to δD of -75 to -85‰. Here we discuss two possible mechanisms to justify this shift: (i) the coseismic dehydration of the wall rocks, as reproduced in experimental dry conditions, and (ii) the growth of biotite in the devitrified pseudotachylyte matrix.

(i) The intrusive relations between pseudotachylytes and cataclasites of the GLFZ, as well as the elemental composition of pseudotachylyte and cataclasites suggest that pseudotachylytes formed when cataclasites were already cemented (Fig. 2b). Artificial pseudotachylytes are thus somewhat reproducing the conditions of formation of natural pseudotachylytes. In artificial pseudotachylytes produced from cataclasites, a negative shift in hydrogen isotope ratio of the frictional melts with respect to the cataclasite protholith, is produced without the ingression of any external fluid, nor devitrification processes. Differently from experiments, in natural pseudotachylytes, the samples hosted in tonalite do not differ significantly from those in cataclasite. This might be due to the complex architecture of the GLFZ, which is formed of a network of faults: the pseudotachylyte veins

apparently hosted in tonalite could have intersect cataclasites in not outcropping sections of the fault. More in general, natural pseudotachylytes often show flow structures, which are independent of the sense of shear of the fault, indicating that melt migration in slipping zones (= fault veins) is driven by the large pressure gradients related to opening of fractures (injection veins) and fault waviness (presence of compressive and extensional domains, Griffith et al., 2010). We propose that selective melting of low melting temperature minerals and dehydration of hydrous minerals in the shear heated cataclasite along the sliding surfaces caused the enrichment in water and lowering in δD measured in the natural pseudotachylytes.

(ii) A negative shift of 20‰ in hydrogen isotope composition of pseudotachylytes of the Homestake Shear Zone if compared with source rock was measured by Moecher and Sharp (2004). The authors suggest that the lowering in δD was due to crystallization of white mica during devitrification processes, accompanied by a loss of water. In the GLFZ pseudotachylytes, the same δD difference from the source rock has been measured (Fig. 6b). However, differently from the Homestake pseudotachylytes, neither white mica, nor clay minerals have been detected, and the only OH-bearing phase is biotite. Hydrogen dissolves in silicatic melts either as OH^- or H_2O (Stolper, 1989) and during cooling and devitrification of the pseudotachylyte veins, hydrogen is incorporated in the hydroxyl ions of hydrated minerals. Crystallization of phyllosilicates causes a negative fractionation of hydrogen, the new minerals resulting enriched in H against D if compared with the residual water (Suzuoki and Epstein, 1976). If the residual water is free to leave the system, the process results in lowering the isotopic composition of the bulk pseudotachylyte. If the water remains in the system, the bulk pseudotachylyte retains the isotopic composition of the melt. Postulating that the initial isotope composition of the melt was the same as biotite with δD≈-75‰, we estimate the loss of water due to crystallization of biotite with a Rayleigh distillation process

$$(\delta D_f - \delta D_i) = 1000[F^{(\alpha-1)} - 1] \qquad (2),$$

where f and i stand for final and initial, F is the fraction of hydrogen remaining in the system and α the isotopic fractionation factor between biotite and water, which varies with temperature. In microlitic domains, biotite has crystallized together with plagioclase, since biotite lamellae are embedded in plagioclase microlites (Fig. 3d). At high cooling rates, a reliable crystallization window for plagioclase is between 1000 and 800°C (Lesher et al., 1999). At T = 800 °C, H-isotope fractionation between biotite and water is low ($1000\ln\alpha_{Bt\text{-}w}$ = -21.29‰; Suzuoki and Epstein, 1976) and F=0.39 is necessary to lower the bulk δD by 20‰. Instead, the matrix of the spherulitic domains crystallized during the late stage of cooling of the vein, and has possibly crossed the glass transition

and undergone devitrification (Di Toro and Pennacchioni, 2004). At low temperature, the hydrogen fractionation between water and biotite is larger (e.g., at 600 °C, 1000 $\ln\alpha_{Bt\text{-}w}$ = -30.74 ‰, at 400°C 1000$\ln\alpha_{Bt\text{-}w}$ = -49.80 ‰) (Suzuoki and Epstein, 1976), and F= 0.52 and F=0.66 are required at 600 and 400°C respectively. In both spherulitic and microlitic domains crystallization of biotite should be accompanied by an important loss of water to be effective in lowering the bulk δD of the pseudotachylytes. The GLFZ pseudotachylytes contain more than 2.5% in weight of water, which is more than the water that can be hosted in the biotite grains of the pseudotachylyte. For example, sample 10-04-pt is composed of 17% in weight of biotite; if all the water were hosted in the crystal lattice of biotite (about 4.2%, Fig. 6), the bulk pseudotachylyte should contain 0.7% of water, which is much less than the 2.8% measured in CHN analyses. Thus, likely pseudotachylytes did not lose a large proportion of water upon biotite crystallization. The water content shows a weak inverse correlation with the hydrogen isotope composition, meaning that the more water in the pseudotachylyte, more negative is the δD. This trend is the opposite than what expected if controlled by a Rayleigh distillation process, where the more reagent (water) is removed, the more intense should be the fractionation effect in the product (biotite) (Fig. 6b). The process of crystallization of biotite during pseudotachylyte cooling and devitrification, even if potentially able to produce a negative isotopic variation, is not likely to be responsible for the whole -20‰ negative shift measured in the GLFZ pseudotachylytes.

4.9.3 Implications for the fluid circulation in seismic fault zones

The hydrogen isotope composition of mylonites suggest that no ingression of an external fluid was associated with the ductile phase of deformation. As suggested by studies in other fault zones (e.g., Kerrich et al., 1984), the ingression of external fluids is associated with the development of a brittle fault system, in this case a network of interconnected cataclasites. The involvement of hydrous fluids in frictional melting is more difficult to assess, because of the complex mineral composition of the pseudotachylyte matrix, which apparently has an hygroscopic behavior. If the contribution of the adsorbed water is subtracted from the measured bulk hydrogen isotope compositions of pseudotachylytes, the δD value of pseudotachylytes can be the result of (i) coseismic shear heating and decomposition of the hydrogen-bearing minerals in the wall rocks, as reproduced in experiments or (ii) the growth of sub-micrometric biotite in the pseudotachylyte matrix. Thus, it is not possible to identify a fluid external to the system in the natural frictional melts.

4.10 Geological implications and conclusions

Microstructural and hydrogen isotope analysis were conducted on artificial friction melts produced in high velocity rock sliding experiments performed on cataclasites of the GLFZ. These analysis suggest that, in presence of a continuous reservoir of hydrous minerals bordering the sliding surface, the process of friction melting itself produces a relative enrichment of H (i.e., more negative δD) in the melt if compared with the source rock. A similar fractionation is found in natural pseudotachylytes, which is not completely explained by precipitation of biotite during cooling and devitrification of pseudotachylytes. We suggest that, since most natural pseudotachylytes of the GLFZ are associated with cataclasites, the D-depletion in friction melts may be primary, due to a mechanism of degassing of OH bearing minerals of the shear heated rocks close to the slipping zone. Thus, no assimilation of external fluids with low δD values is required, and the main source of volatiles in friction melts at the basis of the seismogenic zone is melting and dehydration of the hydrous minerals of the wall rocks.

The hydrothermal cementation by epidote and chlorite associated with the GLFZ had the effect to facilitate friction melting and to furnish a reservoir of water. The lack of evidence of assimilation of an external fluid suggests that the hydrothermal circulation related with faulting was deep-seated and did not reach the surface. Earthquake nucleation and propagation at the base of this seismogenic fault hosted in the continental crust occurred in a (at least isotopically) closed system, where the fluid circulation paths, such as the network of fractures and faults possibly opened during the propagation of seismic ruptures, were quickly sealed by hydrothermal cementation in the interseismic period.

Bibliography

Abercrombie, R., McGarr, A., Kanamori, H., Di Toro, G., 2006. Earthquakes: Radiated Energy and the Physics of Faulting. American Geophysical Union, Washington, D.C. Geophysical Monograph Series, 170 pp.

Allen, A. R., 1979. Mechanism of frictional fusion in fault zones. Journal of Structural Geology 1, 231-243.

Amitrano, D., Schmittbuhl, J., 2002. Fracture roughness and gouge distribution of a granite shear band. Journal of Geophysical Research 107(B12), 2375-2391, doi:10.1029/2002JB001761.

Bakun, W. H., Aagard, B., Dost, B., Ellsworth, W. L., Hardebeck, J. L., Harris, R. A., Ji, C., Johnston, M. J. S., Langbein, J., Lienkaemper, J. J., Michael, A. J., Murray, J. R., Nadeau, R. M., Reasenberg, P. A., Reichle, M. S., Roeloffs, E. A., Shakal, A., Simpson, R. W., Waldhauser, F., 2005. Implications for prediction and hazard assessment from the 2004 Parkfield earthquake. Nature 437, 969-974, doi:10.1038/nature04067.

Beeler, N. M., Tullis, T. E., Blanpied, M. L., Weeks, J. D., 1996. Frictional behavior of large displacement experimental faults. Journal of Geophysical Research 101(B4), 8697-8715.

Bestmann, M., Pennacchioni, G., Nielsen, S., Göken, M., de Wall, H., 2012. Deformation and ultrafine dynamic recrystallization of quartz in pseudotachylyte-bearing brittle faults: A matter of a few seconds. Journal of Structural Geology, in press.

Biørk, T. E., Mair, K., Austrheim, H., 2009. Quantifying granular material and deformation: Advantages of combining grain size, shape, and mineral phase recognition analysis. Journal of Structural Geology 31, 637-653.

Bistacchi, A., Griffith, W. A., Smith, S. A. F., Di Toro, G., Jones, R., Nielsen, S., 2011. Fault Roughness at Seismogenic Depths from LIDAR and Photogrammetric Analysis. Pure and Applied Geophysics 168, 2345-2363, doi: 10.1007/s00024-011-0301-7.

Blanpied, M. L., Lockner, D. A., Byerlee, J. D., 1992. An earthquake mechanism based on rapid sealing of faults. Nature 358, 574-576.

Blanpied, M. L., Lockner, D. A., Byerlee, J. D., 1992. Fault stability inferred from granite sliding experiments at hydrothermal conditions. Geophysical Research Letters 18, 609-612.

Blanpied, M. L., Lockner, D. A., Byerlee, J. D., 1995. Frictional slip of granite at hydrothermal conditions. Journal of Geophysical Research 100(B7), 13045-13064.

Blenkinsop, T. G., 1989. Thickness-displacement relationships for deformation zones: Discussion. Journal of Structural Geology 11, 1051-1054.

Blenkinsop, T. G., 1991. Cataclasis and processes of particle size reduction. Pure and Applied Geophysics 136(1), 59-86.

Blenkinsop, T. G., Sibson, R. H., 1992. Aseismic Fracturing and Cataclasis Involving Reaction Softening Within Core Material From the Cajon Pass Drill Hole. Journal of Geophysical Research 97(B4), 5135-5144, doi:10.1029/90JB02285.

Boness, N., Zoback, M. D., 2006. A multi-scale study of the mechanisms controlling shear velocity anisotropy in the San Andreas Fault Observatory at Depth, Geophysics, 71(5), F131-F146, doi:10.1190/1.2231107.

Boullier, A. M., Fujimoto, K., Ito, H., Ohtani, T., Keulen, N., Fabbri, O., Amitrano, D., Dubois, M., Pezard, P., 2004. Structural evolution of the Nojima fault (Awaji Island, Japan) revisited from the GSJ drill hole at Hirabayashi. Earth Planets Space 56, 1233-1240.

Boullier, A. M., Ohtani, K., Fujimoto, K., Ito, H., Dubois, M., 2001. Fluid inclusions in pseudotachylytes from the Nojima Fault. Journal of Geophysical Research 106(B10), 21965-21977, doi:10.1029/2000JB000043.

Boullier, A. M., 2011. Fault zone geology: lessons from drilling through the Nojima and Chelungpu faults. Geological Society, London, Special Publications 2011 359, 17-37.

Brantut, N., Schubnel, A., Rouzaud, J. N., Brunet, F., Shimamoto, T., 2008. High-velocity frictional properties of a clay-bearing fault gouge and implications for earthquake mechanics. Journal of Geophysical Research 113(B10), B10401.

Brenguier, F., Campillo, M., Hadziioannou, C., Shapiro, N. M., Nadeau, R. M., Larose, E., 2008. Postseismic Relaxation Along the San Andreas Fault at Parkfield from Continuous Seismological Observations. Science 321, 1478-1481.

Brune, J. N., Henyey, T. L., Roy, R. F., 1969. Heat flow, stress, and rate of slip along the San Andreas Fault, California. Journal of Geophysical Research 74, 3821-3827.

Burnham, C. W., 1994. Development of the Burnham model for prediction of H2O solubility in magmas, in: Carroll, M. R., Holloway, J. R., Editors, Volatiles in Magmas, Reviews in Mineralogy and Geochemistry 30, 123-129.

Byerlee, J. D., 1993. Model for episodic flow of high pressure water in fault zones before earthquakes: Geology 21, 303-306.

Carpenter, B. M., Marone, C., Saffer, D. M., 2011. Weakness of the San Andreas Fault revealed by samples from the active fault zone. Nature Geosciences 4, 251-254

Chéry, J., Zoback, M. D., Hickman, S., 2004. A mechanical model of the San Andreas fault and SAFOD Pilot Hole stress measurements. Geophysical Research Letters 31, L15S31, doi:10.1029/2004GL019521.

Chiarabba, C., De Gori, P., Boschi, E., 2009. Pore-pressure migration along a normal-fault system resolved by time-repeated seismic tomography. Geology 38, 1015-1018.

Collettini, C., Niemeijer, A., Viti, C., Marone, C., 2009. Fault zone fabric and fault weakness. Nature 462, 907-910.

Collettini, C., Viti, C., Smith, S. A. F., Holdsworth, R. E., 2009. The development of interconnected talc networks and weakening of continental low-angle normal faults. Geology 37(6), 567-570.

Cowan, D. S., 1999. Do faults preserve a record of seismic slip? A field geologist's opinion. Journal of Structural Geology 21, 995-1001.

De Hoog, J. C. M., Taylor, B. E., Van Bergen, M. J., 2009. Hydrogen-isotope systematics in degassing basaltic magma and application to Indonesian arc basalts. Chemical Geology 266, 256-266.

Del Gaudio, P., Di Toro, G., Han, R., Hirose, T., Nielsen, S., Shimamoto, T., Cavallo, A., 2009. Frictional melting of peridotite and seismic slip. Journal of Geophysical Research 114(B6), B06306, doi:1029/2008JB005990.

Del Moro, A., Pardini, G., Quercioli, C., Villa, I. M., Callegari, E., 1983. Rb/Sr and K/Ar chronology of Adamello granitoids, southern Alps. Memorie della Società Geologica Italiana 26, 285-299.

Dempsey, E. D., Holdsworth, B. E., Di Toro, G., 2011. The role of reactivation and fluid pressure cycling in the development of late zeolite-bearing faults and fractures from the Adamello batholith, Italy. Eos, Transactions American Geophysical Union T31C-2361.

Di Toro, G., Han, R., Hirose, T., De Paola, N., Nielsen, S., Mizoguchi, K., Ferri, F., Cocco, M., Shimamoto, T., 2011. Fault lubrication during earthquakes. Nature 471, 494-498.

Di Toro, G., Hirose, T., Nielsen, S., Pennacchioni, G., Shimamoto, T., 2006. Natural and experimental evidence of melt lubrication of faults during earthquakes. Science 311, 647-649.

Di Toro, G., Hirose, T., Nielsen, S., Shimamoto, T., 2006. Relating high-velocity rock-friction experiments to coseismic slip in the presence of melts, in: Abercrombie R., McGarr, A., Kanamori, H.,

Di Toro, G., Editors, Earthquakes. Radiated Energy and the Physics of Faulting. American Geophysical Union, Washington, D.C., 121-134.

Di Toro, G., Pennacchioni, G., 2004. Superheated friction-induced melts in zoned pseudotachylytes within the Adamello tonalites (Italian Southern Alps). Journal of Structural Geology 26, 1783-1801.

Di Toro, G., Pennacchioni, G., 2005. Fault plane processes and mesoscopic structure of a strong-type seismogenic fault in tonalites (Adamello batholith, Southern Alps). Tectonophysics 402, 55-80.

Di Toro, G., Pennacchioni, G., Nielsen, S., 2009. Pseudotachylytes and earthquake source mechanics, in: Fukuyama, Eiichi, Editors, Fault-Zone Properties and Earthquake Rupture Dynamics. International Geophysics Series, Elsevier.

Dixon, J. E., Dixon, T. H., 1989. Vesicles, amygdales and similar structures in fault-generated pseudotachylytes - Comment. Lithos 23, 225-227.

Dreger, D., Nadeau, R. M., Chung, A., 2007. Repeating earthquake finite source models: Strong asperities revealed on the San Andreas Fault. Geophysical Research Letters 34, L23302, doi:10.1029/2007GL031353.

Etheridge, M. A., Wall, V. J., Cox, S. F., Vernon, R. H., 1984. High fluid pressure during regional metamorphism and deformation: inplications for mass transport and deformation mechanisms. Journal of Geophysical Research 89, 4344-4358.

Evans, J. P., 1988. Deformation mechanisms in granitic rocks at shallow crustal levels. Journal of Structural Geology 10, 437-443.

Fabbri, O., Lin, A. M., Tokushigé, H., 2000. Coeval formation of cataclasite and pseudotachylyte in a Miocene forearc granodiorite, southern Kyushu, Japan. Journal of Structural Geology 22, 1015-1025.

Fagereng, A., Remitti, F., Sibson, R. H., 2010. Shear veins observed within anisotropic fabric at high angles to the maximum compressive stress. Nature Geoscience 3, 482-485.

Faulkner, D. R., Rutter, E. H., 2001. Can the maintenance of overpressured fluids in large strike-slip fault zones explain their apparent weakness? Geology 29, 503-506.

Ferrill, D. A., Morris, A. P., Evans, M. A., Burkhard, M., Groshong, R. H., Onasch, C. M., 2004. Calcite twin morphology: a low temperature deformation geothermometer. Journal of Structural Geology 26, 1521-1529.

Gilbert, G. K., 1909. Earthquake forecast. Science XXIX, 121-138.

Graham, C. M., Sheppard, S. M. F., Heaton, T. H. E., 1980. Experimental hydrogen isotope studies - I. Systematics of hydrogen isotope fractionation in the systems epidote-H2O, zoisite-H2O and AlO(OH)-H2O. Geochimica et Cosmochimica Acta 44, 353-364.

Graham, C. M., Viglino G. A., Harmon, R. S., 1987. Experimental study of hydrogen isotope exchange between aluminous chlorite and water and of diffusion in chlorite. American Mineralogist 72, 566-579.

Grant, J. A., 1986. The isocon diagram-a simple solution to Gresens' equation for metasomatic alteration. Economic Geology 81, 1976-1982.

Grant, J. A., 2005. Isocon analysis: A brief review of the method and applications. Physics and Chemistry of the Earth, Parts A/B/C 30, 997-1004, doi:10.1016/j.pce.2004.11.003.

Gratier, J. P., Favreau, P., Renard, F., Pili, E., 2002. Fluid pressure evolution during the earthquake cycle controlled by fluid flow and pressure solution crack sealing. Earth Planets and Space 54, 1139-1146.

Gratier, J. P., Favreau, P., Renard, F., 2003. Modeling frluid transfer along California Faults when integrating pressure solution crack sealing and compaction processes. Journal of Geophysical Research 108(B2), 2104.

Gratier, J. P., Richard, J., Renard, F., Mittempergher, S., Doan, M. L., Di Toro, G., Hadizadeh, J., Boullier, A. M., 2011. Pressure solution creep as a mechanism of aseismic sliding in active faults: evidence from the San Andreas Fault Observatory at Depth (SAFOD). Geology 39, 1131-1134.

Griffith, A., Nielsen, S., Di Toro, G., Smith, F. A. S., 2010. Rough Faults, Distributed Weakening, and Off-Fault Deformation. Journal of Geophysical Research 115(B08409), 1-22, doi:10.1029/2009JB006925.

Griffith, W. A., Di Toro, G., Pennacchioni, G., Pollard, D. D., 2008. Thin pseudotachylytes in Faults of the Mt. Abbot Quadrangle, Sierra Nevada: physical constraints for small seismic slip events. Journal of Structural Geology 30, 1086-1094, doi:10.1016/jsg.2008.05.003.

Handy, M. R., Hirth, G., Hovious, N., Editors, 2007. Tectonic faults: Agents of change in a dynamic Earth, Report of the 95th Dahlem Workshop on the Dynamics of Fault Zones, Berlin, January 16-21, 2005, MIT Press.

Heilbronner, R., Keulen, N., 2006. Grain size and grain shape analysis of fault rocks. Journal of Structural Geology 427, 199-216.

Hickman, S. H., Zoback M. D., 2004. Stress orientation and magnitudes in the SAFOD Pilot hole, Geophysical Research Letters 31(L15S12), doi:10.1029/2004GL020043.

Hickman, S., Sibson, R., Bruhn, R., 1995. Introduction to special section: meachanical involvement of fluids in faulting. Journal of Geophysical Reseach 100(B7), 12831-12840.

Hirose, T., Shimamoto, T., 2005. Growth of molten zone as a mechanism of slip weakening of simulated faults in gabbro during frictional melting. Joural Geophysical Research 110(B05202), doi:10.1029/2004JB003207.

Holdsworth, R. E., van Diggelen, E. W. E., Spiers, C. J., de Bresser, J. H. P., Walker, R. J., Bowen, L., 2011. Fault rocks from the SAFOD core samples: Implications for weakening at shallow depths along the San Andreas Fault, California. Journal of Structural Geology 33(2), 132-144.

Holloway, J. R., Blank, J. G., 1994. Application of experimental results to C-O-H species in natural melts, in: Carroll, M. R., Holloway, J. R., Editors, Volatiles in Magmas. Reviews in Mineralogy 30, 187-230.

Hubbert, M. K., Rubey, W. W., 1959. Role of fluid pressure in mechanics of overthrusting faulting. Geological Society of America Bulletin 70, 115-205.

Ihringer, P.D., Zhang, Y., Stolper, E.M., 1999. The speciation of dissolved water in rhyolitic melt. Geochimica et Cosmochimica Acta 63, 3567-3578.

Imanishi, K., Ellsworth, W. L., 2006. Source scaling relationships of microearthquakes at Parkfield, CA, determined using the SAFOD pilot hole seismic array, in Eartyhquakes: Radiated energy and the physics of earthquake faulting. Geophysical Monograph Series 170, edited by R. Abercrombie et al., 81-90, AGU, Washington, D.C.

Jefferies, S. P., Holdsworth, R. E., Shimamoto, T., Takagi, H., Lloyd, G. E., Spiers, C. J., 2006. Origin and mechanical significance of foliated cataclastic rocks in the cores of crustal-scale faults: Examples from the Median Tectonic Line, Japan. Journal of Geophysical Research: Solid Earth 111(B12303).

Jeffreys, H., 1942. On the mechanics of faulting. Geological Magazine 79, 291-295.

Johnson, P. A., Mc Evilly, T. V., 1995. Parkfield seismicity: fluid driven?. Journal of Geophysical Research 100(B7), 12937-12950.

Kanamori, H., Brodsky, E. E., 2004. The physics of earthquakes. Reports on Progress in Physics 67(8), 1429-1496.

Kennedy, B. M., Kharaka, Y. K., Evans, W. C., Ellwood, A., DePaolo, D. J., Thordsen, J., Ambats, G., Mariner, R. H., 1997. Mantle fluids in the San Andreas fault system, California. Science 278, 1278-1281.

Kerrich, R., La Tour, T. E., Willmore, L., 1984. Fluid participation in deep fault zones: Evidence from geological, geochemical and 18O/16O relations. Journal of Geophysical Research 89, 4331-4343.

Keulen, N., Heilbronner, R., Stünitz, H., Boullier, A. M., Ito, H., 2007. Grain size distributions of fault rocks: A comparison between experimentally and naturally deformed granitoids. Journal of Structural Geology 29, 1282-1300.

Kirkpatrick, J. D., Shipton, Z. K., 2009. Geologic evidence for multiple slip weakening mechanisms during seismic slip in crystalline rock. Journal of Geophysical Research 114(B12401), doi:10.1029/2008JB006037.

Lachenbruch, A. H., 1980. Frictional heating, fluid pressure, and the resistance to fault motion. Journal of Geophysical Research 85, 6097-6112.

Lachenbruch A. H., Sass, J., 1980. Heat flow and energetics of the San Andreas fault zone. Journal of Geophysical Research 85, 6185-6222.

Langford, J. I., Wilson, A. J. C., 1978. Scherrer after Sixty Years: A Survey and Some New Results in the Determination of Crystallite Size, Journal of Applied Crystallography 11, 102-113.

Lesher, C. E., Cashman, K. V., Mayfield, J. D., 1999. Kinetic controls on crystallization of Tertiary North Atlantic basalt and implications for the emplacement and cooling history of lava at Site 989, Southeast Greenland rifted margin. In: Larsen, H. C., Duncan, R. A., Allan, J. F., Brooks, K., Editors. Proceeding of the ODP. Scientific Results 163, College Station, Texas (Ocean Drilling Program), 3-16.

Lin, A., 1994. Glassy pseudotachylytes from the Fuyun Fault Zone, Northwest China. Journal of Structural Geology 16, 71-83.

Lin, A., 1995. Injection veins of crushing-originated pseudotachylyte and fault gouge formed during seismic faulting. Engineering Geology 43, 213-224.

Lin, A., 2007. Fossil earthquakes: The formation and preservation of pseudotachylytes, Lecture Notes in Earth Sciences 111, Springer.

Lockner, D. S., Morrow, C., Moore, D. E., Hickman, S., 2011. Low strength of deep San Andreas fault gouge from SAFOD core. Nature 472, 82-85.

Logan, J. M., Dengo, C. A., Higgs, N.G., Wang, Z. Z., 1992. Fabrics of experimental fault zones: their development and relationship to mechanical behavior, in: Evans, B., Wong, T. F., Editors. Fault mechanics and transport properties of rocks, Academic Press.

Maddock, R. H., Grocott, J., Van Nes, M., 1987. Vesicles, amygdales and similar structures in fault-generated pseudotachylytes. Lithos 20, 419-432.

Magloughlin, J. F., 1992. Microstructural and chemical changes associated with cataclasis and frictional melting at shallow crustal levels: the cataclasite-pseudotachylyte connection. Tectonophysics 204, 243-260.

Magloughlin, J. F., 1998. Amygdales within pseudotachylyte. In: Snoke, A. W., Tullis, J., Todd, V. R., Editors. Fault Related Rocks-A Photographic Atlas. Princeton, New Jersey, 88-89.

Mair, K., Frye, K., Marone, C., 2002. Influence of grain characteristics on the friction of granular shear zones. Journal of Geophysical Research 107(B10).

Mandl, G., 1988. Mechanics of tectonic faulting. Models and basic concepts. Developments in Structural Geology. Zwart, H.J., Editor, Elsevier.

Marone, C., Scholz, C. H., 1989. Particle size distribution and microstructures within simulated fault gouge. Journal of Structural Geology 11, 799-814.

Marshall, D. J., 1988. Cathodoluminescence in geological materials. Unwin Hyman, Boston.

McKenzie, D., Brune, J. N., 1972. Melting on Fault Planes During Large Earthquakes. Geophysical Journal of the Royal Astronomical Society 29, 65-78.

Meneghini, F., Di Toro, G., Rowe, D. C., Moore, J. C., Tsutsumi, A., Yamaguchi, A., 2010. Record of mega-earthquakes in subduction thrusts: the black fault rocks of Pasagshak Point (Kodiak Island, Alaska). Geological Society of America Bulletin 122, 1280-1297, doi:10.1130/B30049.1.

Miller, S. A., Collettini, C., Chiaraluce, L., Cocco, M., Barchi, M.R., Kaus, B., 2004. Aftershocks driven by a high pressure CO2 source at depth. Nature 427, 724-727.

Miller, S. A., Nur, A., Olgaard, D., 1996. Earthquake as a coupled shear stress-high pore pressure dynamical system. Geophysical Research Letters 23, 197-200.

Mitchell, T. M., Faulkner, D. R., 2009. The nature and origin of off-fault damage surrounding strike-slip fault zones with a wide range of displacements: A field study from the Atacama fault system, northern Chile. Journal of Structural Geology 31, 802-816.

Moecher, D. P., Sharp Z. D., 2004. Stable isotope and chemical systematics of pseudotachylyte and wall rock, Homestake shear zone, Colorado, USA: Meteoric fluid or rock-buffered conditions during coseismic fusion?. Journal of Geophysica Research 109(B12206), doi:10.1029/2004JB003045.

Moore, D. E., Rymer, M. J., 2012. Correlation of clayey gouge in a surface exposure of serpentinite in the San Andreas Fault with gouge from the San Andreas Fault Observatory at Depth (SAFOD). Journal of Structural Geology, in press.

Moore, D., Reynolds, R.C., 1997. X-Ray Diffraction and the Identification and Analysis of Clay Minerals. Oxford University Press, New York, 378 pp.

Moore, D., E., Rymer, M. J., 2007. Talc-bearing serpentinite and the creeping section of the San Andreas fault. Nature 448, 795-797, doi:10.1038/nature06064.

Nadeau, R. M., Michelini, A., Uhrhammer, R. A., Dolenc, D., McEvilly, T. V., 2004. Detailed kinematics, structure and recurrence of micro-seismicity in the SAFOD target region. Geophysical Research Letters 31(L12S08), doi:10.1029/2003GL019409.

Nadeau, R. M., Johnson, L. R., 1998. Seismological studies at Parkfield VI: Moment release rates and estimates of source parameters for small repeating earthquakes. Bulletin of the Seismological Society of America 88, 790-814.

Nestola, F., Mittempergher, S., Di Toro, G., Zorzi, F., Pedron, D., 2010. Evidence of hexagonal anorthite in pseudotachylyte: a tool to constrain the thermal history during a seismic event. American Mineralogist 95, 405-409, doi:10.2138/am.2010.3393.

Nielsen, S., Di Toro, G., Hirose, T., Shimamoto, T., 2008. Frictional melt and seismic slip. Journal of Geophysical Research 113(B01308), doi:10.1029/2007JB005122.

Nollet, S., Urai, J. L., Bons, P. D., Hilgers, C., 2005. Numerical simulations of polycrystal growth in veins. Journal of Structural Geology 27, 217-230, doi:10.1016/j.jsg.2004.10.003.

O'Hara, K. D., Sharp, Z. D., 2001. Chemical and oxygen isotope composition of natural and artificial pseudotachylyte: Role of water during frictional fusion. Earth and Planetart Science Letters 184, 393-406.

Passchier, C. W., Trouw, R. A. J., 2005. Microtectonics, Springer, Berlin, 366 pp.

Pennacchioni, G., 2005. Control of the geometry of precursor brittle structures on the type of ++ductile shear zone in the Adamello tonalites, Southern Alps (Italy). Journal of Structural Geology 27, 627-644.

Pennacchioni, G., Di Toro, G., Brack, P., Menegon, L., Villa, I. M., 2006. Brittle-ductile-brittle deformation during cooling of tonalite (Adamello, Southern Italian Alps). Tectonophysics 427, 171-197.

Pili, E., Poitrasson, F., Gratier, J. P., 2002. Carbon-oxygen isotope and trace element constraints on how fluids percolate faulted limestones from the San Andreas Fault system: partitioning of fluid sources and pathways. Chemical Geology 190(1-4), 231-250.

Pili, E., Kennedy, B. M., Conrad, M. E., Gratier, J. P., 2011. Isotopic evidence for the infiltration of mantle and metamorphic fluids from below in faulted rocks from the San Andreas Fault System. Chemical Geology 281(3-4), 242-252.

Pittarello, L., Di Toro, G., Bizzarri, A., Pennacchioni, G., Hadizadeh, J., Cocco, M., 2008. Energy partitioning during seismic slip in pseudotachylyte-bearing faults (Gole Larghe Fault, Adamello, Italy). Earth and Planetary Science Letters 269, 131-139, doi:10.1016/j.epsl.2008.01.052.

Prior, D. J., Trimby, P.W., Weber, U. D., Dingley, D. J., 1996. Orientation contrast imaging of microstructures in rocks using forescatter detectors in the scanning electron microscope. Mineralogical Magazine 60, 859-869.

Ramsay, J.G., 1980. The crack-seal mechanism of rock deformation. Nature 284, 135-139.

Ramsey, J. M., Chester, F. M., 2004. Hybrid fracture and the transition from extension fracture to shear fracture. Nature 428, 63-66, doi://10.1038/nature02333.

Reches, Z., Dewers, T. A., 2005. Gouge formation by dynamic pulverization during earthquake rupture. Earth and Planetary Science Letters 235, 361-374.

Reid, H. F., 1910. The Mechanics of the Earthquake, The California Earthquake of April 18, 1906. Report of the State Investigation Commission Vol. 2. Carnegie Institution of Washington, Washington, D.C.

Rice, J. R., 1992. Fault stress states, pore pressure distribution, and the weakness of the San Andreas Fault, in: Fault mechanics and transport properties of rocks, edited by Evans, B., Wong, T. F., 475-503, Academic Press, San Diego, California, USA.

Rice, J. R., 2006. Heating and weakening of faults during earthquake slip. Journal of Geophysical Research 111(B05311), doi:10.1029/2005JB004006.

Rietveld, H. M., 1967. Line profiles of neutron powder-diffraction peaks for structure refinement. Acta Crystallographica 22, 151-152.

Robert, F., Boullier, A. M., Firdaos, K., 1995. Gold-quartz veins in metamorphic terranes and the role of fluids in faulting. Journal of Geophysical Research 100, 12861-12879.

Rowe, C. D., Moore, J. C., Meneghini, F., McKeirnan, A. W., 2005. Large-scale pseudotachylytes and fluidized cataclasites from an ancient subduction thrust fault. Geology 33, 937-940.

Rust, A. C., Cashman, K. V., Wallace, P. J., 2004. Magma degassing buffered by vapour flow through brecciated conduit margins. Geology 32, 349-352.

SAFOD (2010). The core Atlas (version 4), http://www.earthscope.org/es_doc/data/safod/Core%20Photo%20Atlas%20v4.pdf .

Sammis, C. G., King, G. C. P., Biegel, R., 1987. The kinematics of gouge deformation. Pure and Applied Geophysics 125, 777-812.

Schleicher, A. M., Tourscher, S. N., Van der Pluijm, B. A., Warr, L. N., 2009. Constraints on mineralization, fluid-rock interaction, and mass transfer during faulting at 2-3 km depth from the SAFOD drill hole, Journal of Geophysical Research 114(B04202), doi:10.1029/2008JB006092.

Scholz, C. H., 2002. The mechanics of earthquakes and faulting. Cambridge Univerity Press, 471 pp.

Shand, S. J., 1916. The pseudotachylyte of Parijs (Orange Free State) and its relation to “trap-shotten gneiss” and “flinty crush rock”. Quarterly Journal of the Geological Society, London 72, 198-221.

Sharp, Z. D., Atudorei, V., Durakiewicz, T., 2001. A rapid method for determination of hydrogen and oxygen isotope ratios from water and hydrous minerals. Chemical Geology 178, 197-210, doi:10.1016/S009-2541(01)00262-5.

Shimamoto, T., Tsutsumi, A., 1994. A new rotary-shear high-speed frictional testing machine: its basic design and scope of research (in Japanese with English abstract). Journal of Tectonic Research Group of Japan 39, 65-78.

Sibson, R. H., 1973. Interactions between temperature and pore fluid pressure during earthquake faulting - a mechanism for partial or total stress relief. Nature 243, 66-68.

Sibson, R. H., 1975. Generation of pseudotachylyte by ancient seismic faulting. Geophysical Journal of the Royal Astronomical Society 43, 775-794.

Sibson, R. H., 1977. Fault rocks and fault mechanisms. Journal of the Geological Society of London 133, 191-213.

Sibson, R. H., 1990. Rupture nucleation on unfavorably oriented faults, Bulletin of the Seismological Society of America 80, 1580-1604.

Sibson, R. H., Roberts, F., Poulsen, K. H., 1988. High angle reverse faults, fluid pressure cycling, and mesothermal gold-quartz deposits. Geology 16, 551-556.

Sibson, R. H., Toy, V. G., 2006. The habitat of fault generated pseudotachylyte: presence vs. absence of frictional melt, in: Abercrombie, R., McGarr, A., Kanamori, H., Di Toro, G., Editors, Earthquakes: Radiated Energy and the Physics of Faulting. Geophysical Monograph Series 170, AGU, 153-166.

Simpson, D. W., Leith, W. S., Scholz, C. H., 1988. Two types of reservoir induced seismicity. Bulletin of the seismological Society of America 78, 2025-2040.

Sleep, N. H., Blanpied, M. L., 1992. Creep, compaction and the weak rheology of major faults. Nature 359, 687-692.

Smith, S. A. F., Collettini, C., Holdsworth, R. E., 2008. Recognising the seismic cycle along ancient faults: CO2-induced fluidization of breccias in the footwall of sealing low-angle normal fault. Journal of Structural Geology 30, 1034-1046.

Solum, J. G., Hickman, S. H., Lockner., D. A., Moore, D. E., Van der Pluijm, B. A., Schleicher, A., Evans, J. P., 2006. Mineralogical characterization of protolith and fault rocks from the SAFOD main hole. Geophysical Research Letters 33(L21314), doi:10.1029/2006GL027285.

Sone, H., Shimamoto, T., Diane, E. Moore Frictional properties of saponite-rich gouge from a serpentinite-bearing fault along the Gokasho-Arashima Tectonic Line, central Japan. Journal of Structural Geology, in press.

Sone, H., Shimamoto, T., 2009. Frictional resistance of faults during accelerating and decelerating earthquake slip. Nature Geoscience, doi:10.1038/NGEO637

Spray, J. G., 1992. A physical basis for the frictional melting of some rock-forming minerals. Tectonophysics 204, 205-21.

Stolper, E. M., 1989. Temperature dependence of the speciation of water in rhyolitic melt and glasses. American Mineralogist 74, 1247-1257.

Storti, F., Balsamo, F., Salvini, F., 2007. Particle shape evolution in natural carbonate granular wear material. Terra Nova 19, 344-352.

Storti, F., Billi, A., Salvini, F., 2003. Particle size distribution in natural carbonate fault rocks: Insighets for non-self-similar cataclasis. Earth and Planetary Science Letters 206, 173-186.

Suzuoki, T., Epstein, S, 1976. Hydrogen isotope fractionation between OH-bearing minerals and Water. Geochimica et Cosmochimica Acta 40, 1229-1240.

Taylor, B. E., Eichelberger, J. C., Westrich, H. R., 1983. Hydrogen isotopic evidence of rhyolitic magma degassing during shallow intrusion and eruption. Nature 306, 541-545.

Taylor, H. P. Jr., 1974. The application of oxygen and hydrogen studies to problems of hydrothermal alteration and ore deposition. Economic Geology 69, 843-883.

Taylor, H. P. Jr., 1977. Water/rock interactions and the origin of fluids in granitic batholiths. Journal of the Geological Society, London 133, 509-558.

Taylor, H. P. Jr., 1978. Oxygen and hydrogen isotope studies of plutonic granitic rocks. Earth and Planetary Science Letters 38, 177-210.

Terzaghi, K., 1943. Theoretical Soil Mechanics. John Wiley and Sons, New York.

Titus, S. J., DeMets, C., Tikoff, B., 2006. Thirty-five-year creep rates for the creeping segment of the San Andreas Fault and the effects of the 2004 Parkfield earthquake: constraints from alignment arrays, continuous global positioning system, and creepmeters, Bulletin of the Seismological Society of America 96(4B), S250-S268, doi:10.1075/0120050811.

Turcotte, D. L., 1997. Fractals and chaos in geology and geophysics. Cambridge University Press, 398 pp.

Ujiie, K., Yamaguchi, H., Sakaguchi, A., Shoichi, T., 2007. Pseudotachylytes in an ancient accretionary complex and implications for melt lubrication during subduction zone earthquakes. Journal of Structural Geology 29, 599-613.

Vannucchi, P., 2001. Monitoring paleo-fluid pressure through vein microstructures. Journal of Geodynamics 32, 567-581.

Vermilye, J. M., Scholz, C. H., 1998. The process zone: A microstructural view of fault growth. Journal of Geophysical Research - Solid Earth 103, 12223-12227.

Vermilye, J. M., Scholz, C. H., 1999. Fault propagation and segmentation: insight from the microstructural examination of a small fault. Journal of Structural Geology 21, 1623-1636.

Villa, I. M., Hermann, J., Müntener, O., Trommsdorff, V., 2000. 39Ar-40Ar dating of multiply zoned amphibole generations (Malenco, Italian Alps). Contributions to Mineralogy and Petrology 140, 363-381.

Werling, E., 1992. Tonale-, Pejo- und Judicarien-Linie: Kinematic, Mikrostrukturen und Metamorphose von Tektoniken aus raumlich interferierenden aber verschiedenaltrigen Verwerfungszonen. PhD. thesis, ETH Zurich.

Wiersberg, T., Erzinger, J., 2008. Origin and spatial distribution of gas at seismogenic depths of the San Andreas Fault from drill-mud gas analysis. Applied Geochemistry 23, 1675-1690, doi:10.1016/j.apgeochem.2008.01.012.

Zoback, M. D., Hickman, S., Ellsworth, W., 2010. Scientific Drilling Into the San Andreas Fault Zone. Eos, Transactions American Geophysical Union 91(22), doi:10.1029/2010EO220001.

Zoback, M. D., Harjes H. P., 1997. Injection-induced earthquakes and crustal stress at 9 km depth at the KTB deep drilling site, Germany. Journal of Geophysical Research 02(B8), 18477-18491.

Appendix. Published papers

In this section, the papers published in peer reviewed journals during the PhD course are reproduced. Here, the contribution of SM to each publication is explained.

1. **Mittempergher, S.**, Pennacchioni G., Di Toro, G., 2009. The effects of fault orientation and fluid infiltration on fault rock assemblages at seismogenic depths. Journal of Structural Geology 31, 1511 – 1524. This paper is based on the data collected during the master thesis in Geology (2006) by SM. SM did the field and analytical work, participated to the conceptual development of the paper and wrote the text.

2. Nestola, F., **Mittempergher, S.**, Di Toro, G., Zorzi, F., Pedron, D., 2010. Evidence of hexagonal anorthite in pseudotachylyte: a tool to constrain the thermal history during a seismic event. American Mineralogist 95, 405-409, doi:10.2138/am.2010.3393. SM contributed to the analytical work (XRD, Raman), to the writing and the general idea development.

3. **Mittempergher, S.**, Di Toro, G., Gratier, J.P., Hadizadeh, J., Smith, S.A.F., Spiess, R., 2011. Evidence of transient increases of fluid pressure in SAFOD phase III cores. Geophysical Research Letters 38, L03301. This work was part of this PhD thesis. SM performed the analytical work, wrote the text and participated to the development of the idea.

4. Gratier, J. P., Richard, J., Renard, F., **Mittempergher, S.**, Doan, M. L., Di Toro, G., Hadizadeh, J., Boullier, A. M., 2011. Pressure solution creep as a mechanism of aseismic sliding in active faults: evidence from the San Andreas Fault Observatory at Depth (SAFOD). Geology 39, 1131-1134. SM participated to the microstructural analysis of the samples and contributed to write the text.